A MEASUREMENT OF NEUTRAL MESON AND DIRECT PHOTON PRODUCTION AT LARGE TRANSVERSE MOMENTUM

A THESIS
SUBMITTED TO THE FACULTY OF THE GRADUATE SCHOOL
OF THE UNIVERSITY OF MINNESOTA

BY

JIM DAVID POVLIS

IN PARTIAL FULLFILLMENT OF THE REQUIREMENTS
FOR THE DEGREE OF
DOCTOR OF PHILOSOPHY

(May, 1984)

ACKNOWLEDGEMENTS

I would like to express my thanks to all members of the experiment described in this thesis: Joe Biel, Alan Jonckheere, and Charlie Nelson from Fermilab; Carl Bromberg, Steve Cooper, Ray Lewis, and Gerry Smith from Michigan State University; Ken Heller, Marvin Marshak, Earl Peterson, Keith Ruddick, and Mike Shupe from the University of Minnesota; Barry Brown, Dave Garelick, George Glass, Mike Glaubman, Shu-Rong Han, Sahadat Hossain, and Ed Pothier from Northeastern University; Clark Chandlee, Selcuk Cihangir, Tom Ferbel, Joey Huston, Joe LeBritton, Fred Lobkowicz, Mike McLaughlin, and Paul Slattery from the University of Rochester. Support for this research was provided by the Department of Energy and the National Science Foundation.

I offer special thanks to my adviser, Ken Heller. I am grateful for the advice and support he has given to me in the course of this work.

It is a pleasure to acknowledge the invaluable assistance and advice I have received from Carl Bromberg, Tom Ferbel, Joey Huston, and Charlie Nelson during the experimental run and during the data analysis.

I have enjoyed working with my fellow graduate students: David Berg, Barry Brown, Clark Chandlee, Selcuk Cihangir, Bruce Collick, Steve Cooper, Steve Heppelmann, and Mike McLaughlin. I have also enjoyed many interesting conversations with Terry Jensen and Marek Zielinski.

I thank Dave Ritchie and Ron Schailey of Fermilab, and Dave Underwood of Argonne National Laboratory for aid in the setup of the experiment.

I am grateful to Bobbi Eich, Mary Dick, and Sandy Smith for their attention to innumerable administrative matters.

Above all, I wish to thank my parents, John and Akiko, to whom this thesis is dedicated, for their love, encouragement, and support.

ABSTRACT

Inclusive cross sections for π^0 and η production near 90° in the center of mass at transverse momenta (p_T) between 2.1 and 5 GeV/c have been measured in 200 GeV/c π^+ and proton collisions with beryllium, carbon, and aluminum targets. These cross sections rise with increasing nucleon number (A) of the target nucleus as A^α, with $\alpha>1$. The ratio of the π^0 yields in pA and π^+ collisions decreases with increasing p_T. The inclusive production of direct photons has been measured for the same kinematic region in 200 GeV/c π^+ and proton collisions on a carbon target. A significant direct photon yield is observed for $p_T>2.5$ GeV/c. The invariant cross section for direct photon production, when compared with measurements from the CERN intersecting storage rings, can be expressed in terms of the variables p_T and x_T ($=2p_T/\sqrt{s}$) as

$$(73\pm27)\ (1-x_T)^{7.9\pm0.8}\ p_T^{-6.9\pm0.2}\ \mu b/GeV^2/c^3$$

(statistical errors only) for the center of mass energy range $\sqrt{s}$=19.4-63 GeV, and the x_T range 0.2-0.5.

TABLE OF CONTENTS

LIST OF TABLES

FIGURE CAPTIONS

CHAPTER 1

Theoretical Background

A. Introduction

Large transverse momentum (p_T) phenomena provide an important way to test current ideas about the fundamental hadronic constituents and their interactions. Observations suggest that the constituents of colliding hadrons (quarks and gluons) undergo hard scattering. The outgoing particles form final state hadrons through a complicated fragmentation process. This tends to obscure the underlying dynamics.

Since quarks carry an electric charge, it is possible to produce a high p_T photon in a hard collision. These are called "direct" or "prompt" photons. The fundamental importance of the study of direct photon production arises from the elementary nature of the photon and its well-understood electromagnetic coupling. In any hard

scattering process that has a gluon emitted from a quark vertex, the gluon may be replaced by a photon. The corresponding cross section is reduced by the ratio of the electromagnetic and strong coupling constants. These photons can emerge as free particles with all of the p_T from the primary collision imparted to them, unlike the gluons which must fragment. A consequence of this fundamentally different behavior is that the γ/π^0 production ratio should rise with p_T, since the π^0 must arise from a p_T dependent fragmentation process and carry off only a fraction of the momentum of its parent.

At present, there is a lack of detailed information concerning the gluon content of hadrons, and the gluon fragmentation process. A major reason for the interest in prompt photon production is that measurements of differences in direct photon cross sections for different incident beams provides the possibility of isolating specific production mechanisms and extracting this information (section C).

Several experiments [1.38-1.47] conducted at the CERN ISR and at Fermilab have measured γ/π^0 over the p_T range 2-12 GeV/c at various energies in pp and pBe collisions. The data indicate that the γ/π^0 ratio is consistent with zero for $p_T<3$ GeV/c, but is >10% at 4 GeV/c, and steadily rises with increasing p_T. The experiment described in this thesis measured direct photon production over the 2-5 GeV/c p_T region with proton and π^+ beam incident on carbon, beryllium, and aluminum targets. Neutral meson decays are the main source of background in a prompt photon experiment. Any measurement of direct

photon production must include a study to ascertain π^0, η, ω, ... yields. Data on the nuclear target dependence of the π^0 and η inclusive cross sections is presented.

In this chapter, the theoretical framework for direct photon production is outlined and previous experiments are briefly reviewed. In Chapter 2, the apparatus is described. Chapters 3-5 discuss event reconstruction, analysis, and the Monte Carlo. The results are presented in Chapter 6.

B. High p_T Inclusive Reactions

During the past several years, a theory describing strong interaction physics has emerged: quantum chromodynamics (QCD). The theory is closely related to quantum electrodynamics. The difference lies in the gauge group involved. The SU(3) color gauge group of QCD is non-Abelian. As a result, the mathematical complexities of QCD are still too great to allow precise tests of the theory. One can calculate in QCD using perturbation theory, just as in quantum electrodynamics. Unfortunately, virtually every process of interest has a non-perturbative component as well. Until the non-perturbative domain of the theory can be quantitatively understood, the best that can be done is to study a broad range of phenomena, looking for consistency with QCD and to seek observations that may constitute clear-cut refutations of the theory. By combining data from a wide range of experiments, it may be possible to arrive at an understanding

of strong interaction dynamics.

The interest in high p_T phenomena has been largely motivated by the possibility that events involving large momentum transfer result from fundamental interactions among the hadronic constituents. In this section, high p_T particle production is discussed. The theoretical framework for hadronic reactions is the parton model, using QCD to describe interactions between the partons. Several excellent reviews of QCD and articles on the application of the parton model to inclusive particle production have been written in the past decade [1.1]. The aim in this section is to give a brief description of how the theoretical calculations are done, and outline their limitations.

The successful application of perturbative quantum chromodynamics (QCD) to the analysis of high momentum transfer hadronic scattering depends on being able to separate the process into parts characterized by well defined momentum scales. The approach is based on a macroscopic picture developed for the "naive" parton model [1.2]. In QCD, the partons are quarks and gluons. Hadrons are viewed as color singlet combinations of these particles. Hadrons interact through individual interactions of their constituents. The model assumes that parton interactions can be treated as interactions among fundamental bare fields in a renormalizable field theory; though quarks and gluons are confined in bound states, free-field boundary conditions are applied. This "factorization", illustrated in Figure 1.1, isolates the scattering mechanism from the hadronic bound state.

Figure 1.1

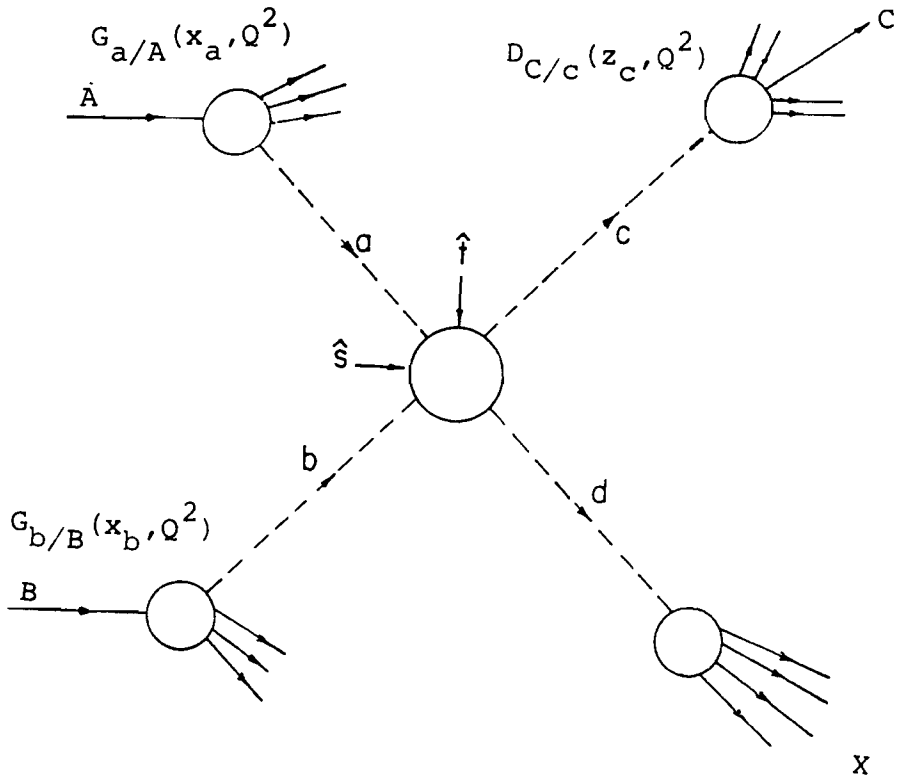

Large momentum transfers between the colliding particles occur in "hard" subprocesses involving the constituents. The internal propagators in the Born diagrams for these subprocesses are typically off-shell by $O(Q^2)$, where Q^2 is the invariant square of an appropriate momentum transfer that characterizes the collision [1.3]. For large Q^2, the amplitude for the subprocesses may be evaluated through a perturbative expansion in the running strong coupling constant [1.4]:

$$\alpha_s(Q^2) = \frac{12\pi}{(33-2n_f)\ \log\ Q^2/\Lambda^2} \quad , \tag{1.1}$$

where n_f is the number of quark flavors that can contribute to the scattering and Λ is the strong interaction renormalization parameter, which sets the scale for Q^2 [1.5]. Eq. 1.1 is only valid for $Q^2 >> \Lambda^2$ and $\ln Q^2 >> \ln(\ln Q^2)$, i.e. when $\alpha_s << 1$. If the number of flavors is less than 16 (for the experiments described in this chapter, $n_f=4$), then $\alpha_s \to 0$ as $Q^2 \to \infty$. This property of "asymptotic freedom" provides the justification for factorization and permits QCD calculations to be performed using perturbation theory [1.6].

Information about the bound state wave functions is taken into account through "structure functions" characterized by momenta with magnitudes typically on the order of the renormalization scale of the theory. These parton distributions cannot be obtained by perturbative methods; they must be determined experimentally. Structure functions are assumed to be process independent. Distributions measured in one reaction are used to predict results in other experiments.

In an inclusive process such as $pp \to \pi^0 + X$ ($X \equiv$ anything) or $pp \to \gamma + X$, the identity of the parent particle is not preserved. The constituents are therefore assumed to interact incoherently. The probability distribution function of the struck constituent in a hadron must be convoluted with the cross section for the hard subprocess. This distribution is the square of the hadronic wave function after integration over the spectator constituents. If the process involves the "hadronization" of the outgoing parton as it emerges from the hard-interaction region, the fragmentation function for this hadron must be folded in. These functions are the overlap of the hadronic wave function with the parton shower produced by the soft radiation of quarks and gluons by the outgoing constituent.

The invariant cross section for the inclusive reaction $A+B \to C+X$ can be expressed in terms of these factors as [1.7]

$$E\frac{d\sigma}{d^3p} = (AB \to CX;\ W, p_T, \theta_{cm}) =$$

$$\sum_{abc} \int dx_a \int dx_b \int dz_c\ G_{a/A}(x_a, Q^2) G_{b/B}(x_b, Q^2) \tag{1.2}$$

$$\times \frac{1}{\pi z_c} D_{C/c}(z_c, Q^2)\ \frac{d\hat{\sigma}}{d\hat{t}}\ (ab \to cd;\ \hat{s}, \hat{t}),$$

where G is a number distribution function [1.8] and D a fragmentation function. The variables $\hat{s}$, $\hat{t}$, and $\hat{u}$ are Mandelstam invariants defined for the constituents. The hard scattering parton cross section for the underlying subprocess $a+b \to c+d$ is $d\hat{\sigma}/d\hat{t}$. W is the incoming hadron-hadron center of mass (c.m.) energy and θ_{cm} is the center of

mass angle of the large p_T trigger hadron, C. The fractional longitudinal momenta carried by partons a and b are x_a and x_b. The trigger hadron C carries off a fraction z_c of parton c's momentum.

A theory with parton distributions that are not functions of Q^2 is said to "scale". In such a model, the invariant cross section for producing a large p_T meson takes the form [1.9]

$$E\frac{d\sigma}{d^3p} = f(x_T,\theta)\ p_T^{-4} \tag{1.3}$$

where θ is the production angle in the center of mass frame. This behavior is not observed experimentally. For p_T below 8 GeV/c, Fermilab and ISR data appear to have a p_T^{-8} dependence at θ=90° [1.10]. One reason for the softening of the p_T distribution is the running of the strong coupling constant, $\alpha_s(Q^2)$.

Another reason is that the strong "radiative" corrections of QCD [1.11] are responsible for scaling violations in the structure and fragmentation functions; in addition to an x dependence, they also evolve with Q^2. In QCD, $d\hat{\sigma}/d\hat{t}$ is calculated by summing Feynman diagrams. Although the coupling constant $\alpha_s(Q^2)$ can be made small by choosing an appropriate renormalization point, terms like $(\alpha_s(Q^2) \log Q^2/\Lambda^2)^n$ ("leading logarithm" terms) arise in the nth order of perturbation theory from configurations in which either collinear or soft gluons are emitted. Since $\alpha_s(Q^2) \sim 1/\log Q^2/\Lambda^2$, such terms are of order one. Thus each successive order in the perturbative expansion makes a comparable contribution to the cross section.

A complete summation of the full perturbation series to all orders is beyond the scope of theoretical techniques available at the present time. It is possible to perform an approximate summation of a particular subset of perturbative graphs to all orders. In the leading logarithm approximation, this subset consists of the terms which make the dominant contributions to the scattering process in each order of the series expansion.

For a calculation performed using the leading logarithm approximation, $\hat{ds}/\hat{dt}$ is calculated to lowest order in $\alpha_s(Q^2)$. Logarithmically divergent contributions from collinear and soft gluon emission are summed and absorbed into the distribution and fragmentation functions using the operator product expansion and the renormalization group equation [1.12]. These divergences are responsible for scaling violations in the structure and fragmentation functions.

There are many problems and ambiguities associated with the use of the leading order formula (Eq. 1.2) at finite energies. It is unclear at the present time to what extent non-leading order corrections affect the leading order results. The corrections to $qq \rightarrow qq$ scattering have been calculated [1.13] and found to be large. It is difficult to make a definitive statement since this subprocess is only one of several which may be involved in a large p_T reaction. The relative sizes of the leading and next to leading order terms also depends on the specific renormalization prescription [1.14]. If the perturbation series is evaluated to all orders, different

renormalization schemes give the same answer. However, when the series is truncated, estimates of higher order corrections depend upon the particular prescription used. It is very likely that these corrections are significant when estimating magnitudes of cross sections.

A related problem is the choice for the variable Q^2. In hadron-hadron reactions, there is no unique large momentum variable which characterizes the momentum transfer in the hard scattering subprocess. The Q^2 variable is constructed from some combination of $\hat{s}$, $\hat{t}$, and $\hat{u}$ which characterizes the subprocess and has the correct dimensions. Predictions at energies currently accessible are sensitive to the precise form of this choice. If next to leading order corrections are taken into account there is no ambiguity, but to leading order all choices that increase linearly with the parton-parton C.M. energy are equivalent. If different choices lead to widely different predictions, the kinematic region under consideration is such that the leading logarithm approximation is invalid.

At low and intermediate p_T values, there may be corrections that fall off by powers of p_T faster than leading order. There is no systematic method for incorporating all of these terms. One power-damped correction of this type is due to the transverse momentum of partons within hadrons, $(k_T)_{q/h}$, and hadrons within the outgoing jets, $(k_T)_{h/q}$. This is particularly important for calculations of single particle production at large p_T because of a "trigger bias"

effect. Configurations in which the initial partons were already moving in the direction of the hadron triggered on are preferentially selected [1.15].

Parton transverse momentum can arise in two ways. In a hadron beam, partons are confined in the transverse direction to within the hadron radius. Because of the uncertainty principle, they must have some "intrinsic" transverse momentum. This momentum involves small Q^2 values and cannot be calculated perturbatively. It is typically parameterized as an exponential or Gaussian in k_T. In QCD, one also expects the hard bremsstrahlung of gluons to impart k_T to partons. This contribution can be calculated perturbatively if the momentum transfers are large. This k_T arises from the non-divergent terms in the bremsstrahlung diagrams; the divergent parts, as discussed above, are incorporated into $G(x,Q^2)$ and $D(z,Q^2)$. Precisely how much these k_T smearing corrections affect single particle rates is still a much debated issue.

Subprocesses involving the large angle scattering of hadrons (e.g. $\pi q \to \pi q$) constitute another set of corrections down by powers of p_T from the leading order parton-parton terms. It has been postulated that these so-called "higher-twist" subprocesses might be important at intermediate p_T values. For example, one might produce a high p_T pion directly rather than demand the higher parton-parton C.M. energy needed to produce a hadron jet containing the trigger pion [1.16]. Some higher-twist terms can be estimated, but it is not possible at present to systematically correct for all such effects.

Quark distribution functions for the proton can be measured in deep inelastic scattering experiments [1.17]. No model independent measurement of the gluon distribution exists. Deep inelastic scattering data and data on J/Ψ production with photon and hadron beams are compatible with a gluon distribution that behaves as $(1 - x)^5$ at Q^2~10 GeV^2, but the error on the exponent is large [1.18]. One cannot conclusively rule out $(1 - x)^4$ behavior. The uncertainties in these distributions are the major source of uncertainty in making theoretical predictions.

Quark decay distribution can be measured by observing the recoilling hadrons in lepton-hadron collisions, or by observing hadrons produced in e^+e^- reactions. The fragmentation function for a gluon is not well constrained experimentally. Gluons do not carry a weak or electromagnetic charge and are not produced directly in e^+e^- annihilation or deep-inelastic scattering. Observations of the away-side jet in two-arm experiments with single particle triggers indicate that $D_{h/g}(z,Q^2)$ is softer than $D_{h/q}(z,Q^2)$, but the parameterizations are quite arbitrary.

Despite these difficulties, if one wanted to make a prediction at large p_T, the first step would be to try Eq. 1.2. The uncertainties primarily affect absolute cross sections; particle and beam ratios should be less sensitive to these various corrections. Ratios are not as dependent on the choice of Q^2 and the assumption of collinear kinematics. Higher order QCD corrections are more likely to affect predictions of the magnitude of a cross section than the ratio

of cross sections. Experimentally, many sources of systematic bias cancel when measuring ratios.

The production of high p_T single photons is of interest because it can provide information difficult to obtain by the study of purely hadronic processes [1.19]. A photon does not fragment into a shower of hadrons; it reflects more closely the kinematics of the underlying subprocess. The situation is similar to that of a jet trigger. The advantage is that there is less ambiguity in the definition of the jet. In addition, use of a direct photon trigger in conjunction with particle identification in the away-side jet may provide a means of determining gluon fragmentation and distribution functions (section C).

In the following section, the QCD subprocesses relevant to direct photon production are discussed. Nuclear target effects are discussed in section D. In section E, theoretical predictions for the γ/π^0 ratio and absolute cross sections are given and compared to previous experiments.

C. Direct Photons

Photons at large transverse momentum can be produced in several ways. The two lowest order subprocesses predicted in QCD produce a photon at the hard scattering vertex with a cross section of order $\alpha\alpha_s(Q^2)$. The subprocess $gq \rightarrow \gamma q$ (Figure 1.2a) is the QCD analogue of Compton scattering. The annihilation diagram $q\bar{q} \rightarrow \gamma g$ is shown in Figure

Figure 1.2

a)
Compton

b)
Annihilation

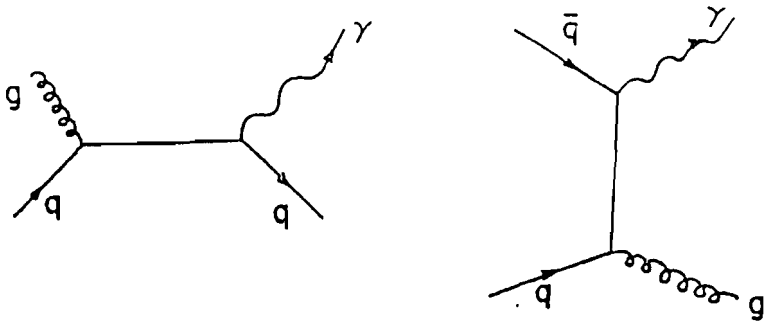

c)
Bremsstrahlung

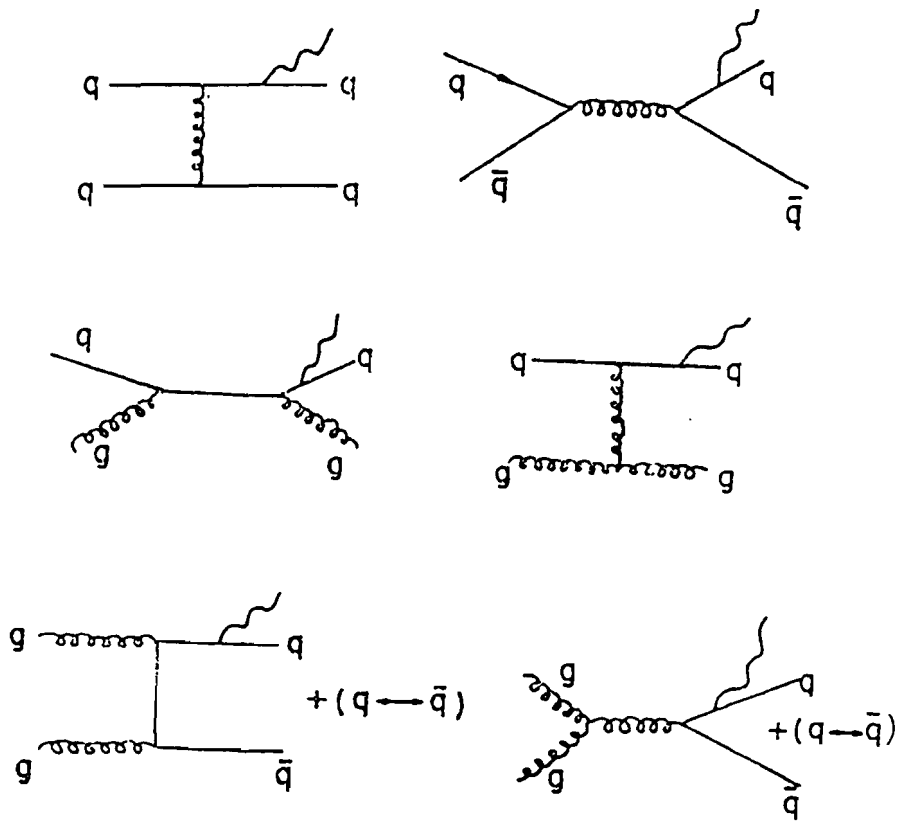

1.2b. The cross sections for these subprocesses after performing color and spin sum averages are [1.23,1.25,1.26]

$$\frac{d\hat{\sigma}}{d\hat{t}}(gq\to\gamma q) = -\frac{\pi\alpha\alpha_s}{3\hat{s}^2} e_q^2 \left(\frac{\hat{u}}{\hat{s}} + \frac{\hat{s}}{\hat{t}}\right) \tag{1.4a}$$

$$\frac{d\hat{\sigma}}{d\hat{t}}(q\bar{q}\to\gamma g) = \frac{8\pi\alpha\alpha_s}{9\hat{s}^2} e_q^2 \left(\frac{\hat{u}}{\hat{t}} + \frac{\hat{t}}{\hat{u}}\right) , \tag{1.4b}$$

where e_q is the fractional electric charge of the quark and $\hat{s}$, $\hat{t}$, and $\hat{u}$ are the Mandelstam invariants for the parton-parton scattering subprocess.

Another way to produce a large p_T photon is quark bremsstrahlung. This is a QCD perturbation theory correction of order $\alpha\alpha_s^2$. Some of the bremsstrahlung diagrams are shown in Figure 1.2c. In order to calculate the contributions from these processes, it is necessary to know the fragmentation function for a quark into a photon, $D_{\gamma/q}$. In leading log QCD, $D_{\gamma/q} \propto \log Q^2/\Lambda^2$ or equivalently, $\propto a/\alpha_s$ [1.20]. When convoluted with order α_s^2 subprocesses ($qq\to qq$, $gq\to gq$, etc.) the result is an overall $\alpha\alpha_s$ dependence. Because of the large number of $O(\alpha_s^2)$ subprocesses, the bremsstrahlung contribution is a potentially large correction to the lowest order subprocesses. The magnitude of the bremsstrahlung component is difficult to assess. The exact fraction of the total cross section depends on the relative hardness of the gluon distribution function, which is not well determined.

Photons produced by the Born processes of Fig. 1.2a and Fig. 1.2b have a different event structure than those emitted in a bremsstrahlung process. They are not produced by parton fragmentation, and therefore are not accompanied by high p_T hadrons. The bremsstrahlung photons may be accompanied by hadrons in nearby regions of phase space. These hadrons are produced by the fragmentation of a quark or gluon participating in the bremsstrahlung subprocess. This provides a means of distinguishing between the different mechanisms experimentally.

There are several parameterizations for distribution and fragmentation functions in common use [1.21]. The general behavior of G for protons and pions at Q=2 GeV is shown in Figure 1.3 [1.22]. In an asymptotically free theory, scaling violations typically cause the number of high-x constituents to decrease as Q^2 increases; this is accompanied by a corresponding increase in the number of low-x constituents.

Consideration of these distributions in conjunction with the expressions in Eq. 1.4 reveals some important features of direct photon production. The proton valence quark content is uud; the antiquark component results from virtual $q\bar{q}$ pairs (the "sea" quarks) produced at low-x. It is difficult to produce a high p_T photon in the annihilation process $q\bar{q}\rightarrow\gamma g$, since antiquarks typically carry a very small fraction of the proton's momentum. Gluon-Compton scattering ($gq\rightarrow\gamma q$) is therefore the dominant lowest order subprocess in a $pp\rightarrow\gamma X$ reaction.

Figure 1.3

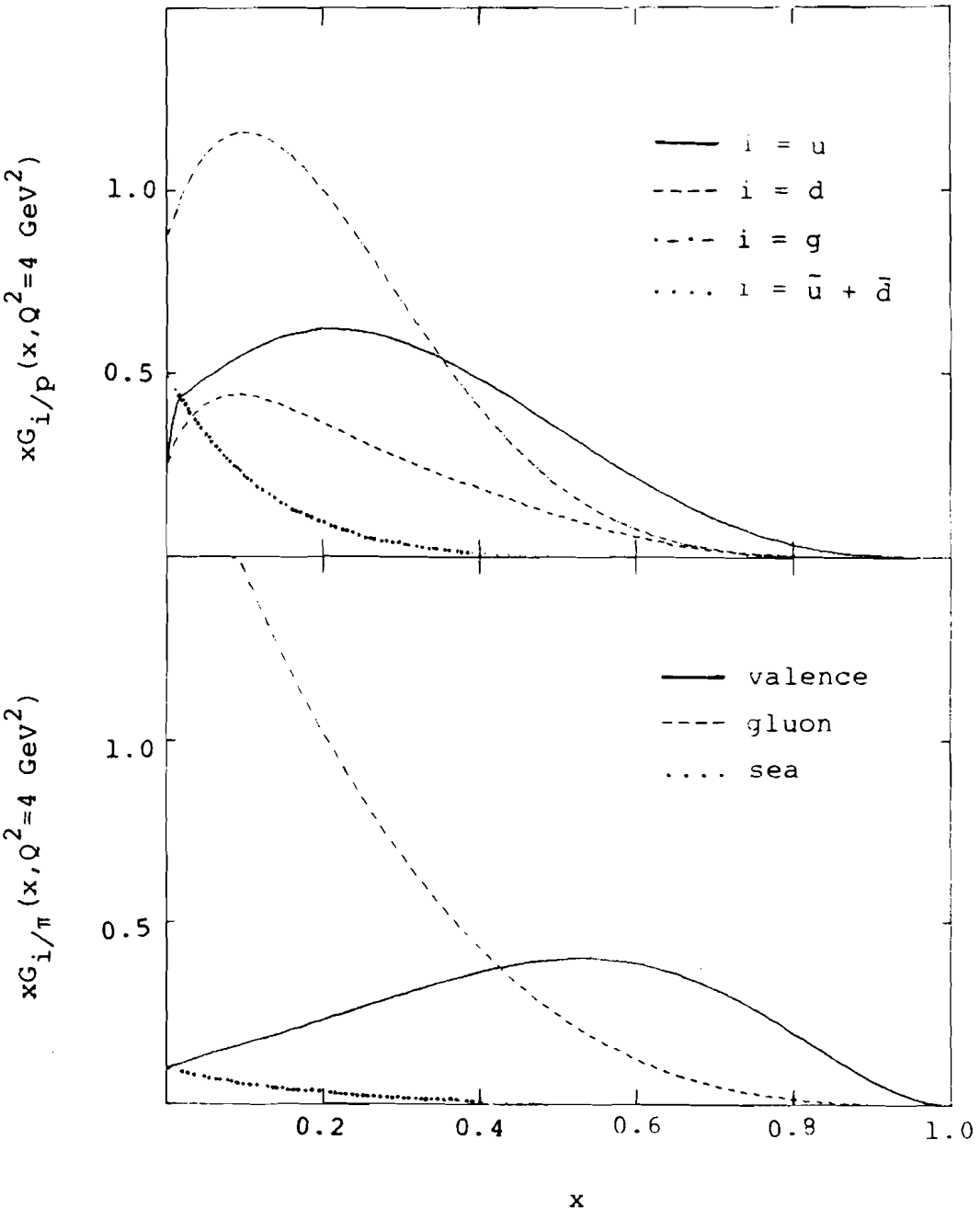
i = u
i = d
i = g
i = ū + d̄
valence
gluon
sea
1.0
0.5
1.0
0.5
0.2
0.4
0.6
0.8
1.0
x
xG_{i/p}(x,Q²=4 GeV²)
xG_{i/π}(x,Q²=4 GeV²)

Photon production in pp collisions occurs primarily through subprocesses involving u-quarks. One reason is the difference in electric charge carried by u and d quarks. The constituent scattering cross sections (Eq. 1.4) are proportional to e_q^2. Since $e_u = +2/3$ and $e_d = -1/3$, the contribution of u-quark subprocesses to the photon yield is a factor of four larger than the contribution from subprocesses involving d-quarks. Another reason is that there are twice as many valence u-quarks as valence d-quarks in the proton.

The valence quark content of the π^+ and π^- are $u\bar{d}$ and $\bar{u}d$ respectively. The valence distributions are related via isospin (I) and charge conjugation (CC) invariance:

$$\begin{aligned} G_{u/\pi^+} &= G_{d/\pi^-} \quad (I) \\ &= G_{\bar{u}/\pi^-} \quad (CC) \\ &= G_{\bar{d}/\pi^+} \quad (\text{apply both}). \end{aligned} \tag{1.5}$$

The momentum distribution of gluons in the pion is presumed to be softer than that of the valence quarks. For $x<0.5$, the gluon distribution is larger than either valence quark distribution. At low x_T ($\simeq 2p_T/\sqrt{s}$), gluon-Compton scattering still dominates $\pi^+p\rightarrow\gamma X$ and $\pi^-p\rightarrow\gamma X$ processes. For $x_T>0.5$, $\bar{u}u\rightarrow\gamma g$ should be an important component of the $\pi^-p\rightarrow\gamma X$ cross section. The annihilation term for $\pi^+p\rightarrow\gamma X$ is $\bar{d}d\rightarrow\gamma g$, which is a factor of four smaller than $\bar{u}u\rightarrow\gamma g$ due to the difference in fractional electric charge. The relative abundance of valence u and d quarks in the proton leads to another factor of two suppression for direct photon production via the leading order

annihilation term in the π^+p reaction, relative to π^-p. As a consequence, gluon-Compton scattering is predicted to dominate the $\pi^+p \rightarrow \gamma X$ cross section for kinematic regions currently accessible experimentally.

The antiproton contains valence antiquarks. The $gq \rightarrow \gamma q$ subprocess in the $p\bar{p} \rightarrow \gamma X$ case is the same as in the pp reaction. The photon yield should be larger for $p\bar{p} \rightarrow \gamma X$ since both Born processes contribute substantially. The annihilation term is expected to dominate π^0 and γ production at large x_T in $p\bar{p}$ interactions.

The relative contributions of the two subprocesses, $gq \rightarrow \gamma q$ and $q\bar{q} \rightarrow \gamma g$, are different for reactions involving π^+, π^-, p, and $\bar{p}$. It is possible to use cross section measurements with different beams to isolate contributions from specific subprocesses. Whenever a photon occurs in the final state via one of these mechanisms, it is either accompanied by a gluon on the away-side or scattering was initiated by a gluon. This leads to the possibility of measuring, or at least constraining, gluon fragmentation functions (if the away-side hadrons are identified), gluon distribution functions for the proton and pion, and pion quark distribution functions [1.23].

The ratio of electromagnetic and strong interaction coupling constants, α/α_s, is of order 0.03 at p_T values present direct photon experiments cover. In addition, there are more subprocesses which contribute to hadron jet production than is the case for direct photons. However, a photon can carry off all of the momentum imparted to it in the primary interaction. In Eq. 1.2,

$$\frac{1}{z_c} D_{C/c}(z_c,Q^2) \rightarrow \delta(1 - z_c). \qquad (1.6)$$

A pion must share the momentum of its parent parton with other particles produced in the jet fragmentation. Events in which a single pion carries off a large fraction of the total jet momentum are relatively rare; measurements indicate that the jet/pion ratio is on the order of a hundred at large p_T [1.24]. This leads to a large enhancement of the ratio of γ and π^0 inclusive cross sections at large p_T. The γ/π^0 production ratio is expected to increase with p_T. A number of effects contribute to this rise: 1) Scaling violations soften the momentum distribution for the hadronic fragments. 2) The gluon distribution is softer than the quark distribution within a hadron. Processes such as $gg \rightarrow gg$ that contribute to hadroproduction, but not to direct photon production, are less important at higher p_T. 3) The Q^2 dependence of α_s leads to an increase in the ratio α/α_s with increasing p_T.

Several predictions for direct photon production can be found in the literature [1.23,1.25,1.26]. They differ in the parameterization of the structure functions, the choice of Q^2, the renormalization prescription, the implementation of k_T smearing, and the manner in which higher twist terms are handled. Several representative calculations are compared with experimental data in section E.

D. Nuclear Target Effects

The densities of heavy nuclear targets are greater than that of hydrogen. They have the virtues of being compact and easy to handle, and are often utilized to study low cross section processes. Aside from their convenience, nuclear targets may yield new physics of intrinsic value. High energy hadron-nucleus scattering experiments probe the space-time development of the hadronic production process.

The atomic weight (A) dependence of cross sections can be parameterized by a power-law of the form $A^{\alpha(p_T,x_F)}$ [1.27], where $x_F \equiv 2p_{longitudinal}/\sqrt{s}$. The total absorption cross section exhibits an $A^{2/3}$ dependence, as would be expected from geometric shadowing considerations [1.28]. The multiplicity of produced particles has been studied using counter techniques [1.29] and nuclear emulsions [1.30]. These data indicate that there is very little intra-nuclear cascading by the fast hadrons produced in the collision. The A-dependence observed in large transverse momentum inclusive particle distributions increases monotonically from $A^{0.9}$ at $p_T \sim 1$ GeV/c to values exceeding unity at larger p_T [1.31]. The trend $\alpha \to 1$ can be understood by supposing that in these rare processes, the screening of one nucleon by another becomes negligible. For α to exceed unity in this picture, nucleons must behave in a cooperative manner (i.e. a rescattering of the outgoing state may occur).

A number of models have been proposed to explain the features of hadron-nucleus collisions at high energies [1.32]. These models

make very different assumptions about the elementary interaction. However, there is as yet no generally accepted quantitative description for the different aspects of these processes. From an experimental viewpoint, it is important to study the limitations of these models and seek further differences that may exist between hadron-hadron and hadron-nucleus collisions.

In the experiment described in this thesis, inclusive γ, π^0, and η production on nuclear targets over the p_T range 2.3-4.0 GeV/c is measured. The Chicago-Princeton collaboration measured the nuclear target dependence of $Ed\sigma/d^3p$ for $\pi^{\pm}$, $K^{\pm}$, p, and $\bar{p}$ with incident protons and π^-. The proton data are on hydrogen, deuterium, beryllium, tungsten, and titanium targets with 400 GeV incident energy at a lab angle corresponding to ~90° in the center of mass. Their results for incident protons are shown in Figure 1.4 [1.33]. For a restricted region of x_F, $\alpha(p_T,x_F) \approx \alpha(p_T)$. The value of $\alpha(p_T)$ rises from ~0.85 at a p_T of 1 GeV/c to a value of 1.10±0.02 around 6 GeV/c for π^+, π^-, and K^+. For K^-, p, and $\bar{p}$, α rose to 1.3 at high p_T. Similar results were obtained with 200 and 300 GeV π^- incident on beryllium, copper, and tungsten at ~90° in the center of mass [1.34].

Outside of resonance regions, the Drell-Yan mechanism [1.35] dominates muon pair production by hadrons. Quark-antiquark pairs annihilate to form a virtual photon, which decays into $\mu^+\mu^-$. Since a photon couples to matter through an electromagnetic rather than a strong interaction, it should be less affected by a passage through surrounding nuclear matter. After an initial rise in α at low

Figure 1.4

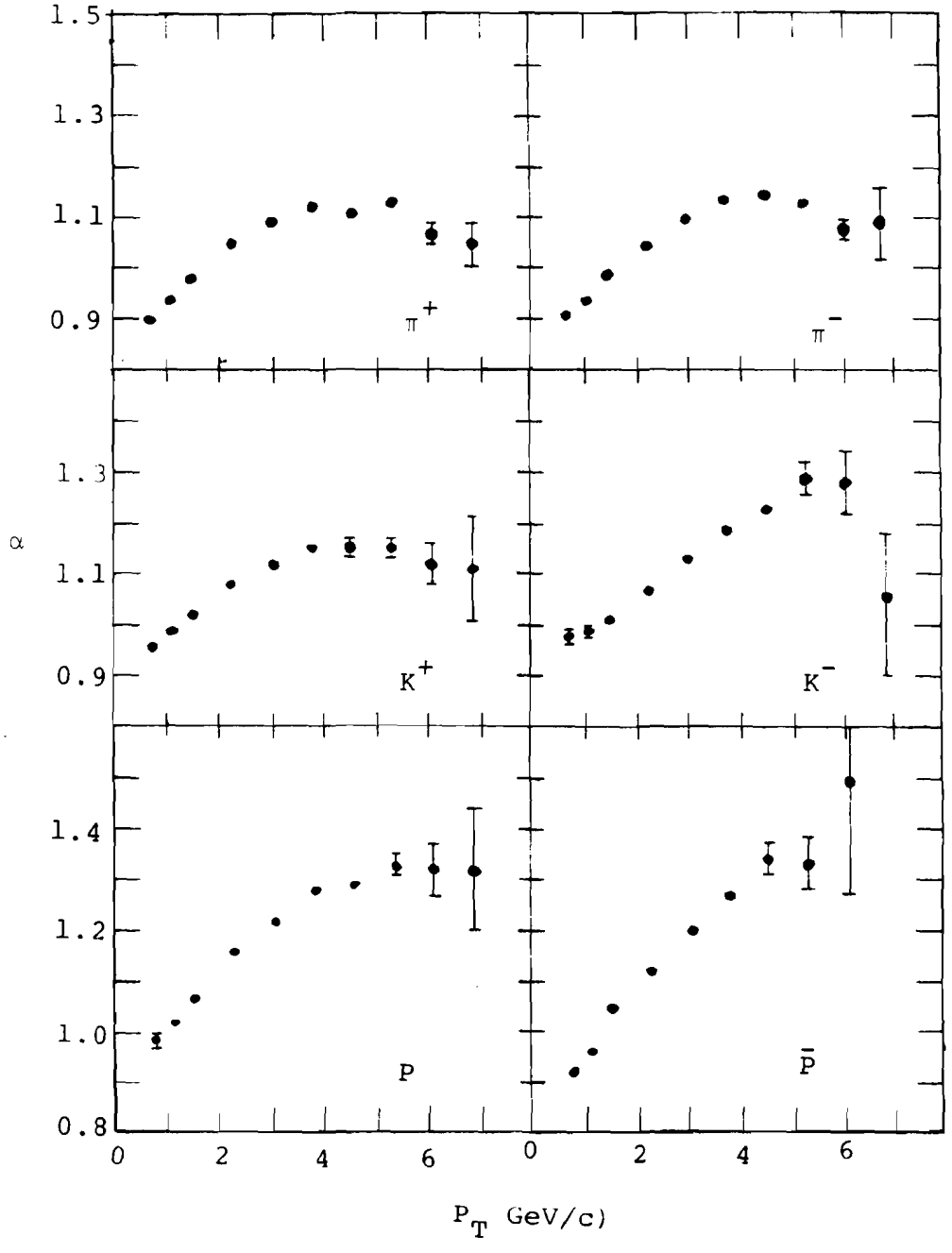

invariant mass, dimuon experiments are consistent with an atomic weight dependence of A^1 [1.36].

If $\alpha_\gamma(p_T) < \alpha_\pi(p_T)$, γ/π^0 measured on a nuclear target should be smaller than γ/π^0 measured in proton-proton collisions. This introduces an additional complication in comparing predictions to data.

E. Previous Experiments

The major problem in a direct photon experiment is the separation of the signal from the background due to meson decays (mainly $\pi^0 \to \gamma\gamma$). Three techniques [1.37] have been used to search for the direct photon signal: 1) resolved π^0 decays, 2) the "conversion" method, and 3) the study of low mass lepton pair spectra (i.e. virtual photons).

The first method requires a detector with sufficient spatial resolution to distinguish a single shower from the two photons from π^0 decay. At the same time, the detector must cover a large enough solid angle to capture both photons from a π^0 decay and to contain a reasonable fraction of the $\eta \to \gamma\gamma$ decays, which have larger opening angles. The requirements of large angular coverage and fine granularity imply a large number of readout channels. This consideration is the main drawback of this method.

The conversion method uses a photon detector with coarse granularity; the two photons from a π^0 decay are usually observed as

one shower. A thin converter placed in front of the photon detector, followed by a track detector, signals the conversion $\gamma \to e^+e^-$. The conversion probability is roughly twice as great for a π^0, where there are two photons, as for a single photon. The average number of photons in the event sample is determined statistically. From this, the fraction of clusters to ascribe to single photons can be calculated. The coarser readout, compared to the first method, makes it possible to cover a larger solid angle for the same cost. The disadvantage is that the backgrounds tend to be larger. Systematic errors for this approach can be comparable to the signal at moderate p_T values.

A third technique involves extrapolation of the invariant mass distribution of lepton pairs to the zero mass limit (virtual → real photons) [1.38,1.39]:

$$q_o \frac{d\sigma(\gamma^* \to e^+e^-)}{d^3q\, dm^2} = \frac{\alpha}{2\pi m^2} \frac{\gamma}{\pi^0} E \frac{d\sigma(\pi^0)}{d^3p} , \qquad (1.7)$$

where m is the mass of a lepton pair of momentum q and energy q_o. The advantage of this approach is that backgrounds are small provided that the mass regions are chosen properly. The disadvantage is the factor $\alpha/2\pi \sim 10^{-3}$ in the rate.

Two experiments at the CERN Intersecting Storage Rings (ISR) observed low mass lepton pairs and set limits on direct photon production in pp collisions. Cobb et al. [1.38] (BNL-CERN-Syracuse-Yale) set an upper limit of (.55±.92)% on γ/π^0 in the p_T

range 2-3 GeV/c for $\langle\sqrt{s}\rangle$ = 55 GeV (averaged over 52 and 63 GeV data). Chilingarov et al. [1.39] (CERN-Saclay-Zurich) measured γ/π^0 = 1.9% at p_T=1.9 GeV/c for $\sqrt{s}$=53 and 63 GeV.

At somewhat higher p_T values, several experiments have observed a direct photon signal in pp collisions. Darriulat et al. [1.40] (Aachen-Heidelberg-CERN-Dubna) measured the yields of single photons and π^0's at 90° in the center of mass at the ISR for $\sqrt{s}$=45 and 53 GeV, using a lead glass hodoscope as a photon detector. They observed a γ/π^0 ratio of ~(20±6)% between p_T=2.8 and 3.8 GeV/c. However, the authors stress that the lead glass array was primarily intended for use as a triggering counter in a different experiment; no detailed study of its energy response and resolution had been made. The experiment was also limited by systematic uncertainty in the antineutron background level.

Baltrusaitis et al. [1.41] (Fermilab-John Hopkins) measured direct photon production at Fermilab in pBe interactions for incident beam energies of 200 and 300 GeV. This corresponds to $\sqrt{s}$=19.4 and 23.8 GeV. Their γ detector was a five by five array of lead glass blocks covering $90° < \theta_{cm} < 160°$. At p_T<3 GeV/c, their data, averaged over $\sqrt{s}$, yield γ/π^0 = 0.070±0.025, which is substantially higher than the ISR measurements using virtual photons. For the range 3-4 GeV//c, they observe γ/π^0 = 0.08±0.025 at $\sqrt{s}$=19.4 GeV and γ/π^0 = 0.094±0.025 at $\sqrt{s}$=23.8 GeV. Their background-subtracted and acceptance-corrected γ/π^0 ratios are plotted in Figure 1.5 as a function of p_T. The shaded band is an estimate of the overall systematic uncertainty. Also shown are various QCD predictions.

Figure 1.5

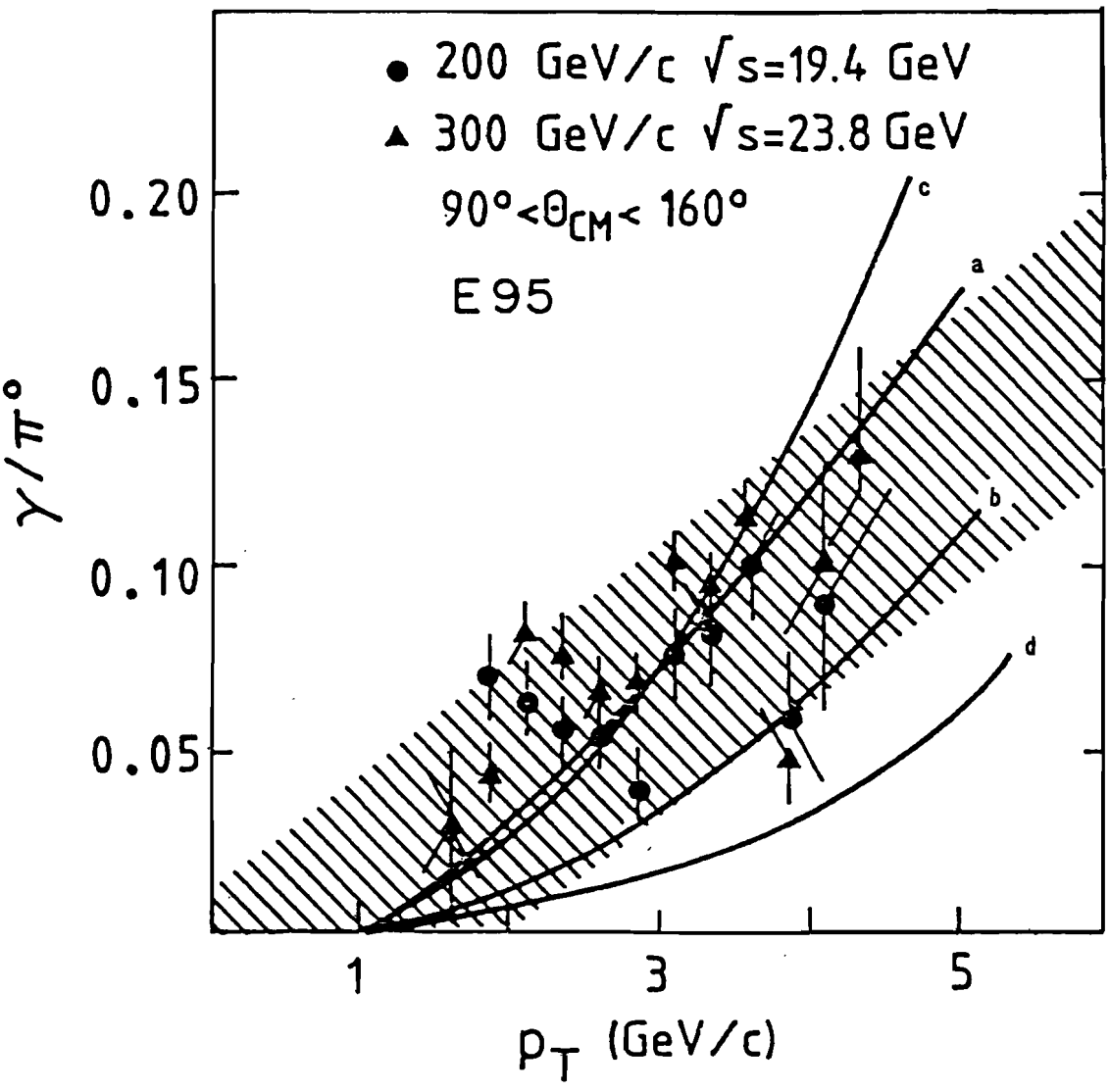
● 200 GeV/c √s=19.4 GeV
▲ 300 GeV/c √s=23.8 GeV
90°<θCM< 160°
E95
a
b
c
d
0.20
0.15
0.10
0.05
γ/π°
1
3
5
pT (GeV/c)

Data from three ISR experiments [1.42,1.43,1.45] are summarized in Figure 1.6 (Contogouris et al., Ref. 1.25). The γ/π^0 ratio of each collaboration was multiplied by their π^0 cross section to obtain the inclusive single photon cross sections. The dashed lines are theoretical predictions using a hard gluon distribution function for the proton. Including $O(\alpha_s^2)$ corrections in the soft gluon limit yields the solid curves.

Amaldi et al. [1.42] (Rome-BNL-CERN) measured γ/π^0 at $\sqrt{s}$=30.6 and 53.2 GeV at the ISR, using a matrix of lead glass counters. Their ratio is consistent with zero for p_T<3 GeV/c, and shows a tendency to increase for larger p_T.

The CERN-Columbia-Oxford-Rockefeller collaboration (CCOR) made a statistical estimate of the single photon component of their data by measuring the average conversion probability for the sample in a one radiation length thick converter. They studied pp collisions at the ISR for $\sqrt{s}$=44 and 62.4 GeV [1.43]. They normalized their data to agree with the measurement of Amaldi et al. for the range $3.5 < p_T < 5.0$ GeV/c. There was an additional 5% systematic uncertainty, of which 3% was $\sqrt{s}$ dependent. For $\sqrt{s}$=62.4 GeV, the average ratio for the range p_T = 6-10 GeV/c is

$$\langle \gamma/\text{all} \rangle \equiv \langle f_\gamma \rangle = 0.074 \pm 0.012 \text{ (statistical)} \pm 0.053 \text{ (systematic)}.$$

For p_T>10 GeV/c,

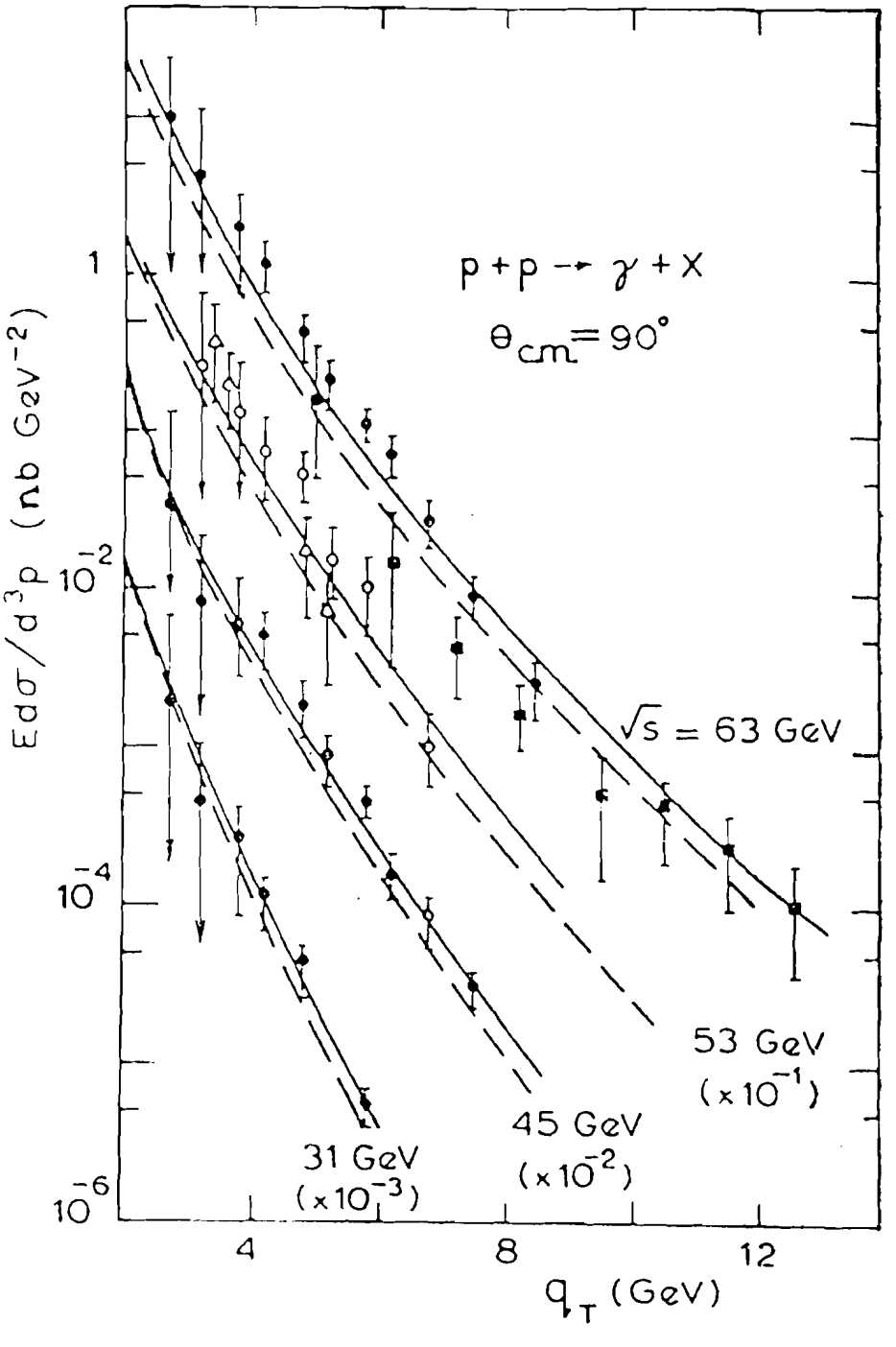
p + p → γ + X
θcm = 90°
√s = 63 GeV
53 GeV
(×10⁻¹)
45 GeV
(×10⁻²)
31 GeV
(×10⁻³)
E dσ/d³p (nb GeV⁻²)
1
10⁻²
10⁻⁴
10⁻⁶
4
8
12
qT (GeV)

Figure 1.6

$$\langle f_\gamma \rangle = 0.26 \pm 0.04 \text{ (statistical)}$$
$$\pm 0.05 \text{ (systematic)}.$$

The group also performed studies of the event structure associated with prompt photons [1.44]. The aim was to differentiate between QCD Compton production and bremsstrahlung production of photons. Events were divided into two classes: (1) those in which the trigger particle was accompanied by at least one other particle of $P_T > 0.3$ GeV/c in the same hemisphere, and (2) those which were not accompanied. Values of f_γ for accompanied triggers were lower than those for unaccompanied triggers, suggesting that direct photons are due mainly to processes such as $gq \rightarrow \gamma g$ or $q\bar{q} \rightarrow \gamma g$, which result in photons unaccompanied by other particles in the trigger hemisphere, rather than quark bremsstrahlung. A measurement of the ratio of positive/negative particles in the hemisphere opposite the trigger particle indicates that the ratio is higher for single photons than for neutral mesons. This favors the subprocess $gu \rightarrow \gamma u$ as the predominant source of direct photons.

The Athens-Athens-Brookhaven-CERN collaboration (A^2BC) conducted a series of experiments at the ISR on direct photons and neutral meson production using the same apparatus in different configurations [1.45]. The experiments measured inclusive or quasi-inclusive pp cross sections near 90° in the center of mass for $\sqrt{s}$ = 31, 45, 53, and 63 GeV. The p_T range covered extends up to ~12 GeV/c. Two lead-liquid argon ionization calorimeters were used as

photon detectors. Their spatial resolution was sufficient to resolve π^0 decays up to the highest p_T values encountered. Three different geometrical configurations were used in order to cover the p_T range more effectively and as an aid in evaluating systematic errors. The γ/π^0 ratio rises from ~5% at p_T=3.5 GeV/c to ~60% at p_T=12 GeV/c. The signal increases with p_T and shows little $\sqrt{s}$ dependence at fixed p_T.

The A^2BC group collaborated with the Axial Field Spectrometer group (AFS) to study correlations of high p_T γ triggers with charged particles for the rapidity range $|y_{cm}|<1$ at $\sqrt{s}$=63 GeV [1.46]. An open axial field magnet and drift chamber were used for charged particle identification. They quote a 2σ upper limit of 30% for the ratio of bremsstrahlung production to total prompt photon production over the p_T range 5.5-8 GeV/c. Their data on the charge asymmetry in the recoil jet agree fairly well with QCD predictions (Benary et al., Ref. 1.25), although the calculations are sensitive to details of the fragmentation model.

The A^2BC collaboration had to apply an "unassigned energy" cut in order to extract the prompt γ signal from the liquid argon calorimeter information. Only events with a single shower and <35 MeV of additional energy deposited in the calorimeter were accepted as prompt γ candidates. This requirement made the measured cross section non-inclusive. After installation of the AFS drift chamber, the effect of this cut could be assessed for the $\sqrt{s}$=63 GeV data by measuring the probability that charged tracks hitting the calorimeter deposited enough energy to fail the cut. From this study, they

deduced a correction factor; the inclusive single photon cross section is 1.4 times the cross section measured with the unassigned energy cut, independent of p_T. This study was not performed at other $\sqrt{s}$ values because the drift chamber had not been installed when these runs were made.

Most direct photon experiments have been performed at scattering angles near 90° in the center of mass. The angular dependence of prompt γ production may provide a sensitive means of testing the predictions of constituent scattering models. The bremsstrahlung contribution is predicted to make up a large fraction of the prompt γ cross section at small angles [1.20]. Akesson et al. [1.47] (AFS collaboration) measured γ/π^0 in the rapidity range $2.00 < y_{cm} < 2.75$ in pp collisions at $\sqrt{s}$=63 GeV at the ISR. The photon detector consisted of a uranium/scintillator sandwich, and was part of the Axial Field Spectrometer. The γ/π^0 ratio was comparable to that measured at $y_{cm} \approx 0$ up to a maximum p_T of 4.5 GeV/c. They found no clear indication of a strong enhancement in single photon production attributable to bremsstrahlung.

F. Goals of This Experiment

There is substantial overlap in the types of problems that can be addressed in colliding beam and fixed target experiments. However, in other respects the two sets of data are complementary. Fixed target machines offer higher luminosities and the possibility of using

meson beams. It is also important to probe different kinematic regions and to employ different geometric configurations in order to guard against possible experimental biases. Nuclear targets complicate matters if one wants to make a comparison with pp data. On the other hand, use of a variety of nuclear targets may yield insights into the time development of hadronic processes.

The experiment described in this thesis (Fermilab experiment 629) was a prototype for a more ambitious proposal to study direct photon production at Tevatron energies. The principal objectives were: (1) to determine whether a liquid argon ionization calorimeter could cope with the interaction rates expected in a prompt photon experiment at a fixed target machine, (2) develop a satisfactory trigger, (3) study backgrounds, and (4) obtain physics results by measuring the production of γ, π^0, and η on nuclear targets for π^+ and proton beams.

CHAPTER 2

Experimental Apparatus

A. General Considerations

In this chapter, the apparatus used in the experiment is described. The objective of the experiment was to measure the production of photons and neutral mesons over the p_T range of 2.0 to 5.0 GeV/c, corresponding to an energy range of approximately 20 to 50 GeV. The major experimental difficulty in measuring the direct photon signal is the background contribution from neutral mesons (π^0, η, ω ...) decaying into two or more photons. If some of the decay photons are not detected, the remainder may contribute to the single photon background. Another possibility is that two photons may be too close together to be resolved, and appear as a single photon. An accurate estimate of these backgrounds depends on precise information regarding

neutral meson production. In addition, the apparatus must be able to distinguish between hadronic and electromagnetic showers. A linear energy response is necessary in order to minimize systematic shifts in the measurement of π^0 energies relative to single photon energies, which induce large differences in the relative yields.

A liquid argon calorimeter (LAC) used in a previous Fermilab experiment (E272) was used as a photon detector. Figure 2.1 shows the region of phase space covered by the LAC. The LAC spanned ~1.4 units of rapidity and ~0.75 radians in azimuth. It had an energy resolution of ~15%/$\sqrt{E}$ and a position resolution of ~1 mm (Chapter 3.C). Photons with energies as low as one GeV were detected. These properties helped to minimize the photon backgrounds. Although roughly 25 radiation lengths in depth, the LAC was only ~1.2 pion interaction lengths thick. This permitted good photon-hadron discrimination (Chapter 4.B). The LAC had a linear energy response over the p_T range covered in E629. The systematic error in the γ/π^0 ratio attributed to detector nonlinearity was less than ±1.5% (Chapter 6.A).

Figure 2.2 shows the layout of the experiment. The LAC was positioned to one side of the beamline, covering a region around 90° in the center of mass frame. The position of the LAC relative to the beam axis was determined using a tape measure. The center of the detector was 812±1 cm downstream of the target, and offset from the beam axis by 114±1 cm. It was turned to face the target, in order to reduce the deviation of photons from normal incidence.

Figure 2.1

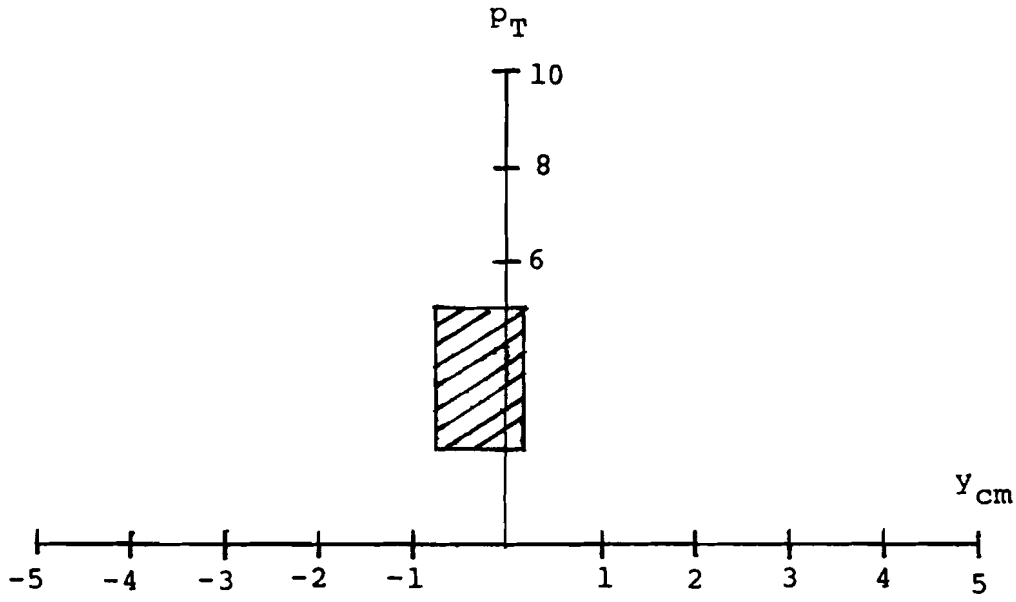

Figure 2.2

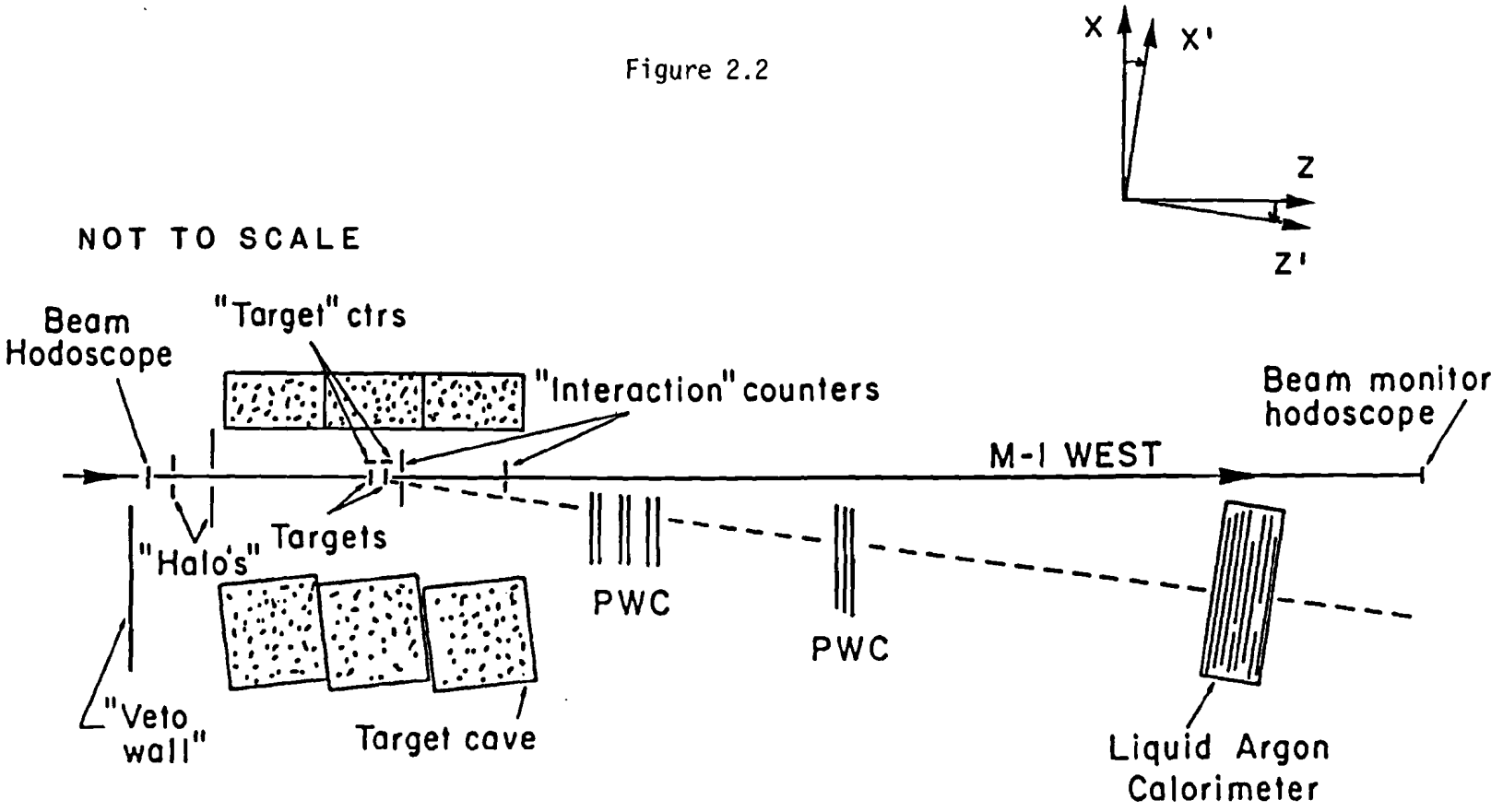
X
X'
Z
Z'
NOT TO SCALE
Beam Hodoscope
"Target" ctrs
"Interaction" counters
Beam monitor hodoscope
M-1 WEST
"Halo's"
Targets
PWC
PWC
"Veto wall"
Target cave
Liquid Argon Calorimeter

Two right-handed coordinate systems will be used in describing the experiment. The unprimed system defines the laboratory frame. The positive Z-axis is directed downstream along the beam axis and the positive Y-axis points vertically upward. The origin is at the midpoint of the two target segments (section C). The X′-Z′ plane of the "primed" system is rotated +110 mrad with respect to the unprimed system, and the origin is translated to the center of the LAC. This system is useful when referring to photon coordinates in the LAC; the Z′ and X′ axes are respectively perpendicular and parallel to the detector planes. In the following sections, the beamline characteristics, targets, chambers, LAC, trigger, and data acquisition system are discussed.

B. Beamline

Fermilab experiment E629 was performed in the M1 West beamline of the Meson Laboratory [2.1]. The 200 GeV/c positive beam consisted of ~87% protons and ~13% π+. Typical intensities for data runs were in the range 10^6-10^7 particles/sec. Figure 2.3 is a schematic of the beam transport system showing ray traces of selected beam particles as determined by the program TRANSPORT [2.2].

The 400 GeV/c primary proton beam from the main ring was focused on a 0.16 cm x 0.16 cm x 20.32 cm long beryllium target. The secondary particles were split among six beamlines. The M1 beamline accepted 200 GeV/c positively charged particles nominally produced at

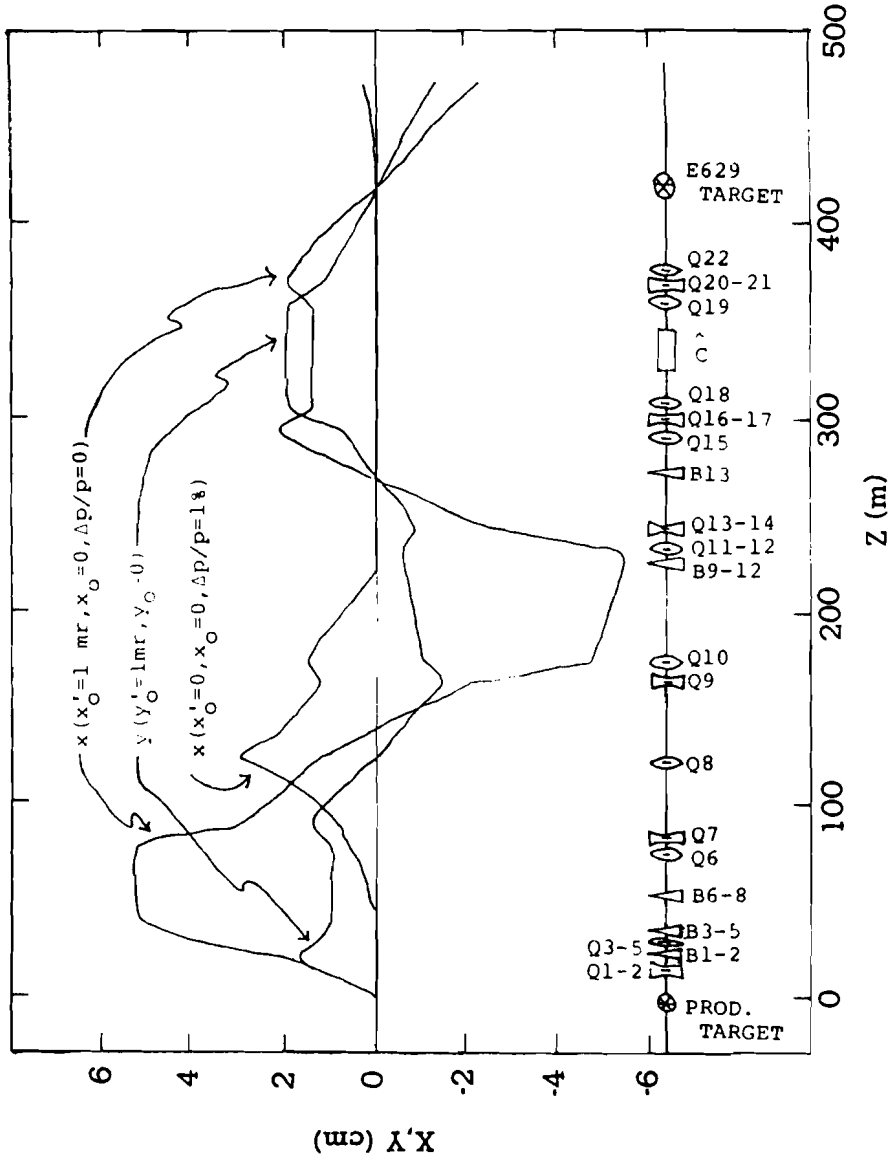
E629
TARGET
Q22
Q20-21
Q19
C
Q18
Q16-17
Q15
B13
Q13-14
Q11-12
B9-12
Q10
Q9
Q8
Q7
Q6
B6-8
B3-5
B1-2
Q3-5
Q1-2
PROD.
TARGET
Z (m)
X,Y (cm)
x (x'o=1 mr, xo=0, Δp/p=0)
x (xo'=0, xo=0, Δp/p=1%)

Figure 2.3

-3.9 mrad relative to the primary beam. The momentum spread of the beam was $|\Delta p/p| < 2\%$, and the maximum acceptance for the tune was ~2 μster.

The M1 beamline was made up of three stages. In the first stage, particles were brought to a focus at a momentum dispersed image ~134 m downstream of the production target. A collimator positioned at this focus defined the range of momenta transmitted to the experimental area. In the second stage, the different momenta were recombined and refocused at ~268 m.

The beam region between 305 and 358 m consisted of a "parallel" section of small angular divergence. A differential Cerenkov counter [2.3] in this section was used to tag π^+ and protons in the beam. The counter was 32.3 m long. Helium gas was used as a radiating medium. Light radiated at an angle of 7.5 mrad was detected by a ring of 6 phototubes. Signals from adjacent phototubes were added together. A two-fold coincidence was required to tag a particle. The helium gas pressure was chosen to maximize the detection efficiency for pions. A plot of the particle fraction versus pressure is shown in Figure 2.4.

Control over the elements in the M1 beamline was available through a laboratory supported beamline computer system located in the electronics trailer. The beam spot size was monitored by several segmented wire ion chambers located at certain positions along the beamline. The beam intensity was controlled using collimators located 268 m downstream of the production target. The main ring accelerator control provided a series of reference times to indicate the beginning

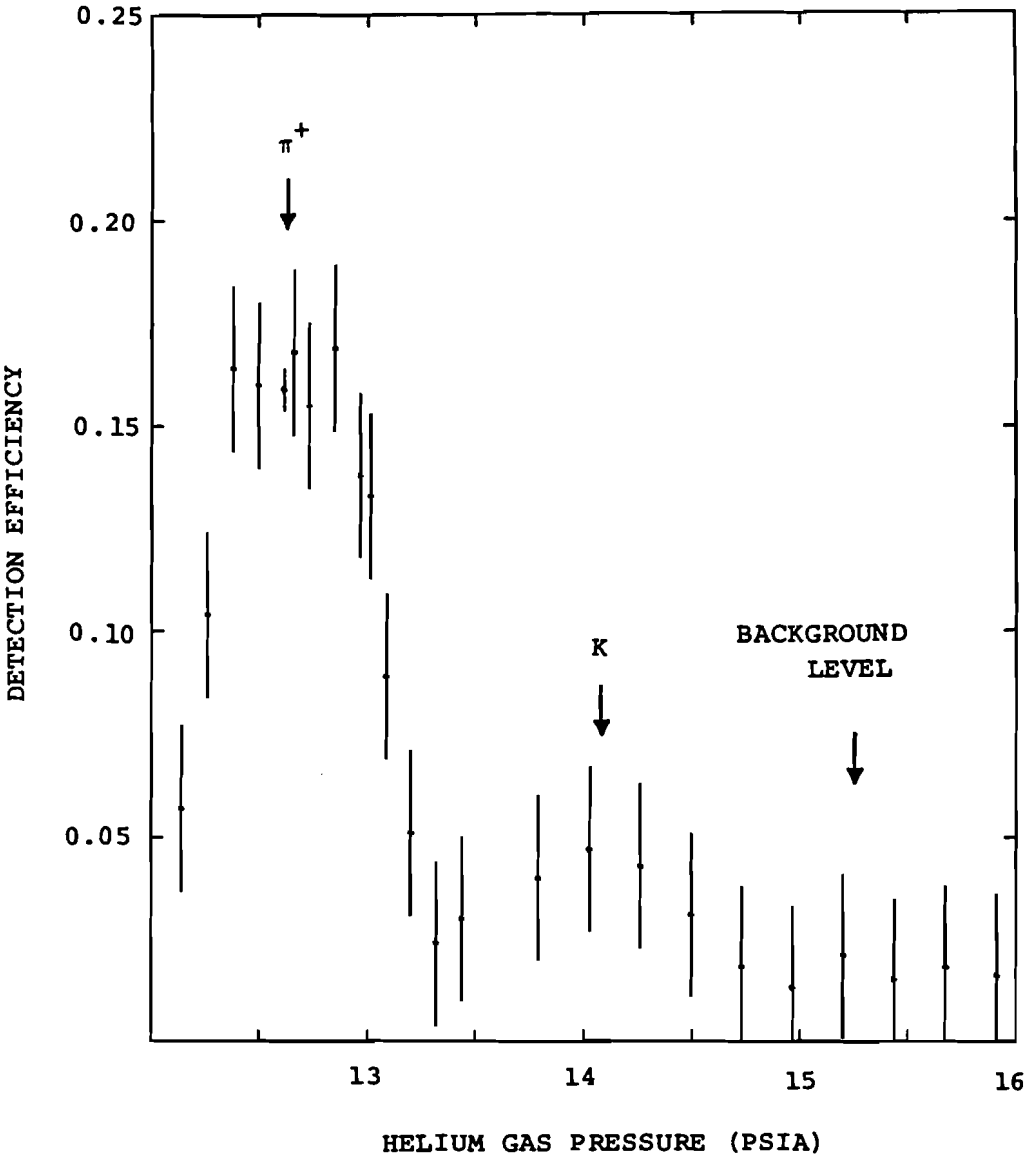
0.25
0.20
0.15
0.10
0.05
DETECTION EFFICIENCY
π+
K
BACKGROUND
LEVEL
13
14
15
16
HELIUM GAS PRESSURE (PSIA)

Figure 2.4

and end of the main ring "flat-top". This defined the time interval during which the beam was extracted from the main ring (≈800 msec). These reference times were used for turning on the electronics during the beam spill.

Just upstream of the experimental target, the beam was defined by a scintillation counter hodoscope [2.4]. It had a row of elements arrayed horizontally for measuring X-position, and a row arrayed vertically for Y-position measurement. Each view consisted of 12 elements. The active area of the hodoscope was 2.2 cm x 2.2 cm. The eight central elements in each projection were 1 mm wide, providing fine-grained resolution for the region of highest beam density. Outside the central region, 2 mm and 5 mm wide elements were used. A beam monitor hodoscope was located downstream of the apparatus. It consisted of a horizontally arrayed plane with the same physical layout as the beam hodoscope.

Two beam halo counters were used to veto events that had particles parallel to, but offset from the beam. A large wall of veto counters and a set of concrete blocks surrounding the target area shielded the liquid argon calorimeter from interactions upstream of the target, and from any beam outside of the halo counters.

C. Targets

Data were taken with three targets in order to study nuclear effects in γ, π^0, and η production. Most of the the data were taken

with a carbon target. About a tenth as much was taken with each of the other two materials, aluminum and beryllium. Some relevant target characteristics are summarized in Table 2.1.

The choice of target materials was based on considerations of radiation length and interaction length. If a photon converts to an e^+e^- pair within a material, the charged particles undergo multiple Coulomb scattering. If their opening angle is appreciable, it may appear as though two photons were produced. To reduce the probability for this to occur, materials with long radiation lengths were desired. To attain high event rates, materials with short interaction lengths were desired. The scaling properties of the radiation length and interaction length as functions of atomic weight (A) and atomic number (Z) led to the choice of relatively low Z materials [2.6].

The targets were split into two segments, each 5% of a radiation length thick. The two blocks were spaced 25 cm apart. At this separation, photons produced with large p_T in the upstream block did not pass through the downstream segment. The segmentation helped to maintain the $\gamma \rightarrow e^+e^-$ conversion rate at a low level, while allowing a reasonable interaction rate. Because no analyzing magnet was used in this experiment, essentially all of the conversion electron pairs merged into one shower (Chapter 5.F). Thus, these photons were not lost from the data sample.

The separation of the target blocks introduced an uncertainty of ~1% in the p_T scale, due to the fact that the distance between the LAC and the point of origin of the photon was not known to better than ±12.5 cm. This point is discussed further in Chapter 6.A.

Table 2.1. Target Properties

Element	Z	A	Thickness x length x Width (cm) (±.002 cm)	Mass (gm) (±.1 gm)	Total Radiation Lengths†	Total Absorption Lengths†	$A/N_o \rho \ell$ (barns)
Be 1	4	9.01	1.91 x 2.55 x 2.55	22.95	.107	.104	2.13
Be 2			1.91 x 2.55 x 2.55	22.6			
C 1	6	12.01	1.27 x 2.55 x 2.56	13.9	.099	.051	4.74
C 2			1.27 x 2.53 x 2.56	13.6			
Al 1	13	26.98	.468 x 2.54 x 2.56	8.3	.106	.025	17.6
Al 2			.473 x 2.53 x 2.55	8.2			

† See Ref. 2.5.

D. Proportional Wire Chambers

The material between the target and the LAC included the proportional wire chamber (PWC) planes (mylar windows, wires, argon-isobutane-freon-methylal gas mixture) and air. The total number of radiation lengths of material is estimated to be ~3%. Chamber information was not used in the analysis of the data (i.e. see Ref. 4.3).

E. Liquid Argon Calorimeter

An electron or photon traversing a material generates an electromagnetic cascade shower [2.7]. The particle typically interacts with an atom after travelling roughly one mean free path. Bremsstrahlung and pair production generate electrons or photons as reaction products. These secondaries again interact in the material. After many interactions, the average energy of the secondaries is too low to support further multiplication. The shower then decays through ionization energy loss and Compton scattering.

The median shower depth as a function of incident energy increases roughly logarithmically. Containment of an electromagnetic cascade inside a detector generally requires at least 10 to 20 radiation lengths of material [2.8].

Hadronic showers are more complex because of the variety of particles produced in a succession of energy-dependent hadronic

interactions and decays. The hadronic mean free path is ~4-30 times as great as the electron-photon mean free path for most materials (aluminum and heavier). The longitudinal extent of a hadronic shower is typically much greater than that of an electromagnetic shower. This provides an effective means of distinguishing between the two types of particle.

The experimental goals dictated the following requirements: (1) the ability to handle rates of ~1 MHz, (2) good position and energy resolution for identification of π^0 and η decay photons, (3) good photon-hadron discrimination, (4) the possibility of using information from the device in defining a trigger for the experiment, (5) stable operation over long periods of time, (6) uniform response over the active area, and (7) coverage of a large area at reasonable cost. These requirements were met by using a sampling calorimeter that consisted of layers of a lead converter sandwiched between liquid argon ionization chambers [2.9]. The calorimeter had been used in a previous Fermilab experiment (E272) in 1978 and 1979. The theory of operation of these detectors is reviewed in the papers of Willis and Radeka (Ref. 2.8), Engler et al. [2.10], Knies and Neuffer [2.11], and Brassard [2.12].

Two cells of the liquid argon calorimeter (LAC) are shown in Figure 2.5. It consisted of alternating layers of 61 lead sheets (2.00 mm thickness) and 62 copper-clad (≈0.03 mm thick copper) G-10 boards (1.60±0.03 mm thickness) separated by 2.0 mm gaps filled with liquid argon. The lead sheets were reasonably uniform in thickness;

Figure 2.5

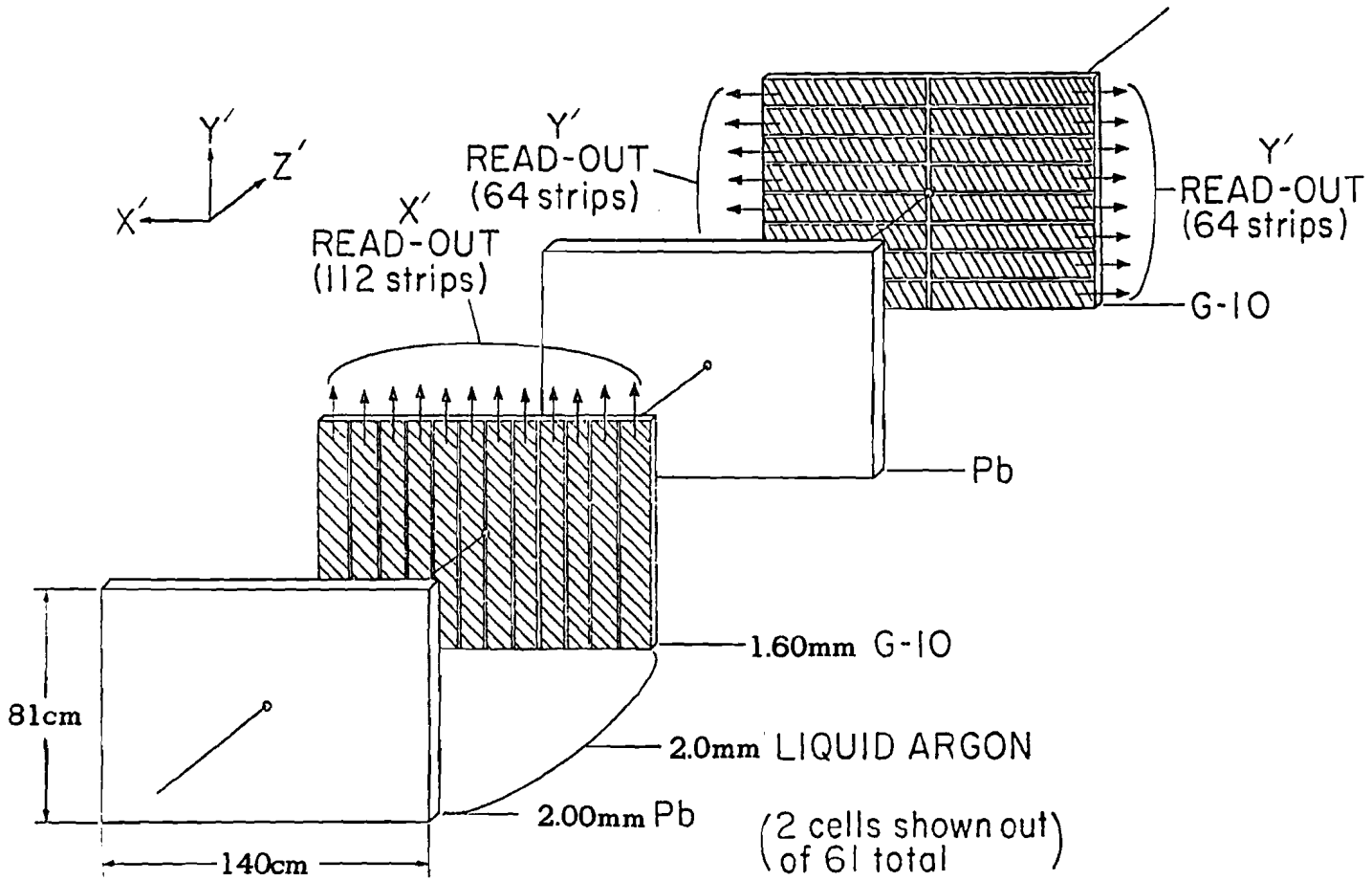
Y′
Z′
X′
Y′
READ-OUT
(64 strips)
X′
READ-OUT
(112 strips)
Y′
READ-OUT
(64 strips)
G-10
Pb
1.60mm G-10
2.0mm LIQUID ARGON
2.00mm Pb
81cm
140cm
(2 cells shown out
of 61 total)

variations were less than ±50 μm. The surfaces of the sheets were flat to better than 0.5 mm, as measured from the highest point on the plane to the lowest. The flattest plates in the set were stacked in the forward portion of the calorimeter, where most of the energy was deposited and where uniformity was most critical. The gaps were defined by spacers along the detector edges. Spacers were scattered randomly over each G-10 board to make the gaps uniform over the detector surface. Mylar shims (~0.08 mm thick) compensated for varying spacer thicknesses. The edge thickness of the finished stack was uniform to ±0.5 mm out of a total thickness of 50 cm.

Electromagnetic showers were induced by the lead sheets. The liquid argon served as the active medium. Charged particles in the shower deposited energy in the argon by producing ion pairs and exciting atoms. The shower energy was measured by collecting the ionization charge. The calorimeter was operated as an ion-chamber without electron multiplication. To maintain a satisfactory signal/amplifier noise ratio, the charge collected had to be a reasonable fraction of the total deposited. Liquid argon has several desireable properties as an active medium. It does not attach free electrons readily and has a high electron mobility (~5 mm/sec at 1kV/mm). Many electronegative impurities are frozen out in liquid argon. It is dense (~1.4 gm/cm^3) and reasonably inexpensive. It is not difficult to purify and is inert (i.e. non-flammable). The chief disadvantage is that the containment vessel must be maintained at liquid argon temperatures (86°K).

A liquid argon ionization chamber is a single-carrier device as far as charge collection is concerned. The electron drift velocity in liquid argon is 3-4 orders of magnitude greater than that of a positive ion (Ref. 2.12). Because of their low mobility, positive ions contribute little to the signal charge in the time required for electrons to drift across the gap. The basic current and charge waveforms for a planar electrode geometry are shown in Figure 2.6. Holding the lead sheets at a negative potential caused the ionization electrons to drift toward the copper-clad boards, which were maintained at ground potential. As electrons drifted across the gaps, they induced charge on the electrodes. The induced signal was measured by a set of charge-sensitive amplifiers.

The collected charge, Q, can be calculated from energy conservation (Ref. 2.12). Consider first the contribution of a single ion pair produced at a distance x from the negative electrode (Fig. 2.6a) at time t=0. The potential in the gap as a function of position, x, is $V(x) = V_o x/d$, where V_o is the voltage difference between the electrodes and d is the gap width. The energy delivered to the chamber from the external circuit equals the change in potential energy of the electron as it drifts across the gap:

$$Q(t)V_o = e[V(t) - V(t=0)]. \qquad (2.1)$$

Define the drift velocity (v_d) and drift time (t_d) as:

$$v_d = dx/dt \ (=\text{constant}),$$

Figure 2.6

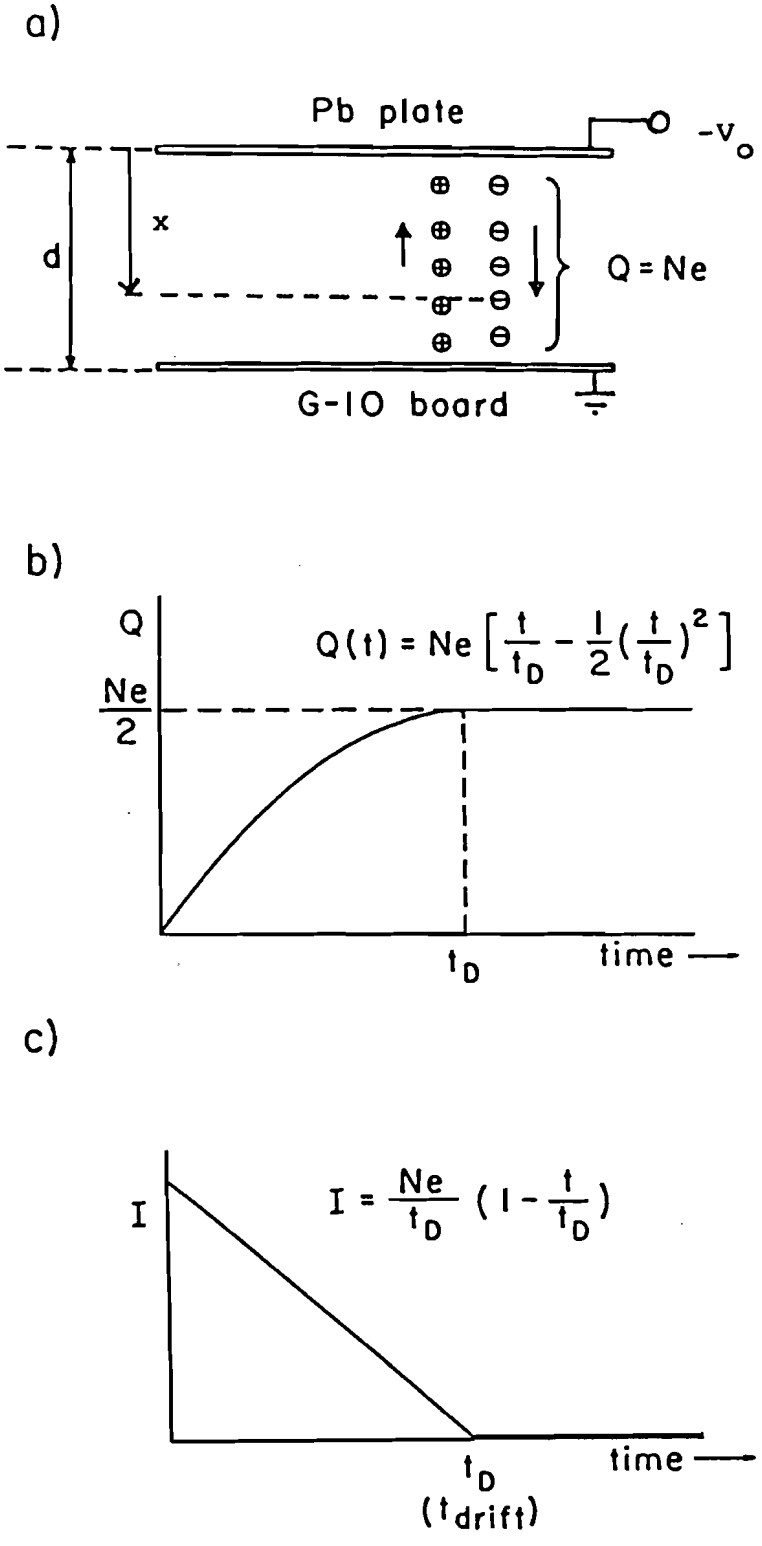
a)
Pb plate
$-V_o$
x
d
Q = Ne
G-10 board
b)
Q
Ne/2
$Q(t) = Ne\left[\frac{t}{t_D} - \frac{1}{2}\left(\frac{t}{t_D}\right)^2\right]$
t_D
time
c)
I
$I = \frac{Ne}{t_D}\left(1 - \frac{t}{t_D}\right)$
time
t_D
(t_{drift})

and

$$t_d = d/v_d.$$

The time derivative of the potential is

$$(dV/dx)(dx/dt) = V_o/t_d.$$

Thus,

$$[V(t) - V(0)] = \begin{cases} V_o \dfrac{t}{t_D} & 0 < t < t_{max} \\ V_o \dfrac{(d - x)}{d} & t \geq t_{max}, \end{cases} \qquad (2.2)$$

$$\text{where } t_{max} \doteq \frac{[(d - x)/d]}{v_D}.$$

At time t_{max}, the electron reaches the positive electrode. The collected charge for a single ion pair is therefore given by

$$Q(t) = \begin{cases} e \dfrac{t}{t_D} & 0 < t < t_{max} \\ e \dfrac{(d - x)}{d} & t \geq t_{max}. \end{cases} \qquad (2.3)$$

Integrating over the uniform distribution of liberated charge (total charge Ne) yields

$$Q(t) = \begin{cases} Ne\left[\frac{t}{t_D} - \frac{1}{2}\left(\frac{t}{t_D}\right)^2\right] & 0 < t < t_D \\ \frac{Ne}{2} & t \geq t_D. \end{cases} \qquad (2.4)$$

The expression for the current is just the time derivative:

$$I(t) = \begin{cases} \frac{Ne}{t_D}\left(1 - \frac{t}{t_D}\right) & 0 < t < t_D \\ 0 & t \geq t_D. \end{cases} \qquad (2.5)$$

There is some loss of signal because drifting electrons recombine with positive ions, and because they are trapped by impurities. Trapped electrons form negative ions which drift slowly and do not contribute to the signal pulse. Impurities other than oxygen and a variety of freon are generally harmless (Ref. 2.8) because of their low electronegativity (nitrogen) or negligible vapor pressure in liquid argon (water). Studies (Ref. 2.10) have shown that the presence of oxygen in argon at a level of ~10 ppm reduces the collected charge by about a factor of two.

An energy of 24 eV is required to produce an ion pair in liquid argon [2.13]. Half of the total charge is collected (Eq. 2.4); the other half remains in the argon in order to image the positive ions, which have low mobility. For the detector configuration used in this experiment, ~16% of the shower energy was deposited in the argon. A one GeV photon therefore deposited ~0.5 picocoulombs of collectible

charge in the argon. The ratio of the collected charge to the total amount deposited, as a function of the applied voltage, is plotted in Figure 2.7. At the 2.2 kV operating voltage, roughly 40% of the available charge was collected.

The G-10 boards were etched to form 1.27 cm wide strips with 0.5 mm interstrip gaps on both sides. This lateral segmentation made it possible to determine shower positions. Alternate boards had strips oriented vertically (for X′-position measurement) and horizontally (for Y′-position measurement). (A simple coordinate transformation yielded the X and Y positions.) The vertical strips extended over the full length of the boards. The horizontal strips were split into right and left halves. A total of 61 lead, liquid argon, G-10 cells were stacked to provide a thickness of 24.5 radiation lengths and 1.2 pion absorption lengths. All strips with the same X or Y position along the axis of the detector were connected to a single amplifier channel. However, Y measuring cells were read out as right/left sections and the entire LAC readout was electrically subdivided into front and back halves, each containing ~12.5 radiation lengths of material. Thus there were six separate sections: X′-front, X′-back, Y′-front right, Y′-front left, Y′-back right, and Y′-back left. A total of 480 amplifier channels (224 X′ and 256 Y′) were required for this arrangement. The sensitive area of the whole detector measured 140 cm horizontally and 81 cm vertically.

The detector assembly was suspended from a steel cover plate for the cylindrical cryostat. The top and side views of the

Figure 2.7

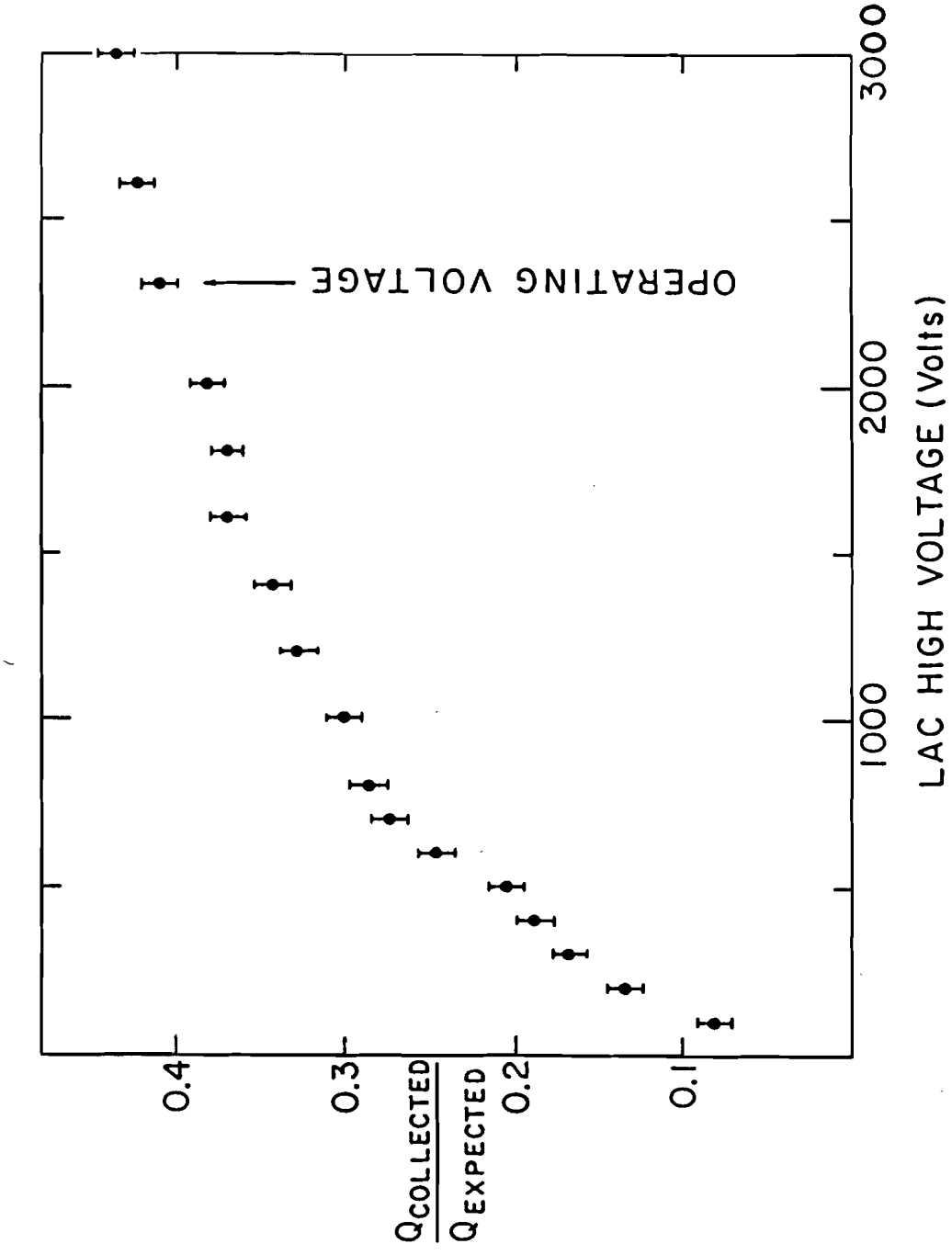
OPERATING VOLTAGE
3000
2000
1000
LAC HIGH VOLTAGE (Volts)
0.4
0.3
0.2
0.1
Q COLLECTED / Q EXPECTED

Figure 2.8

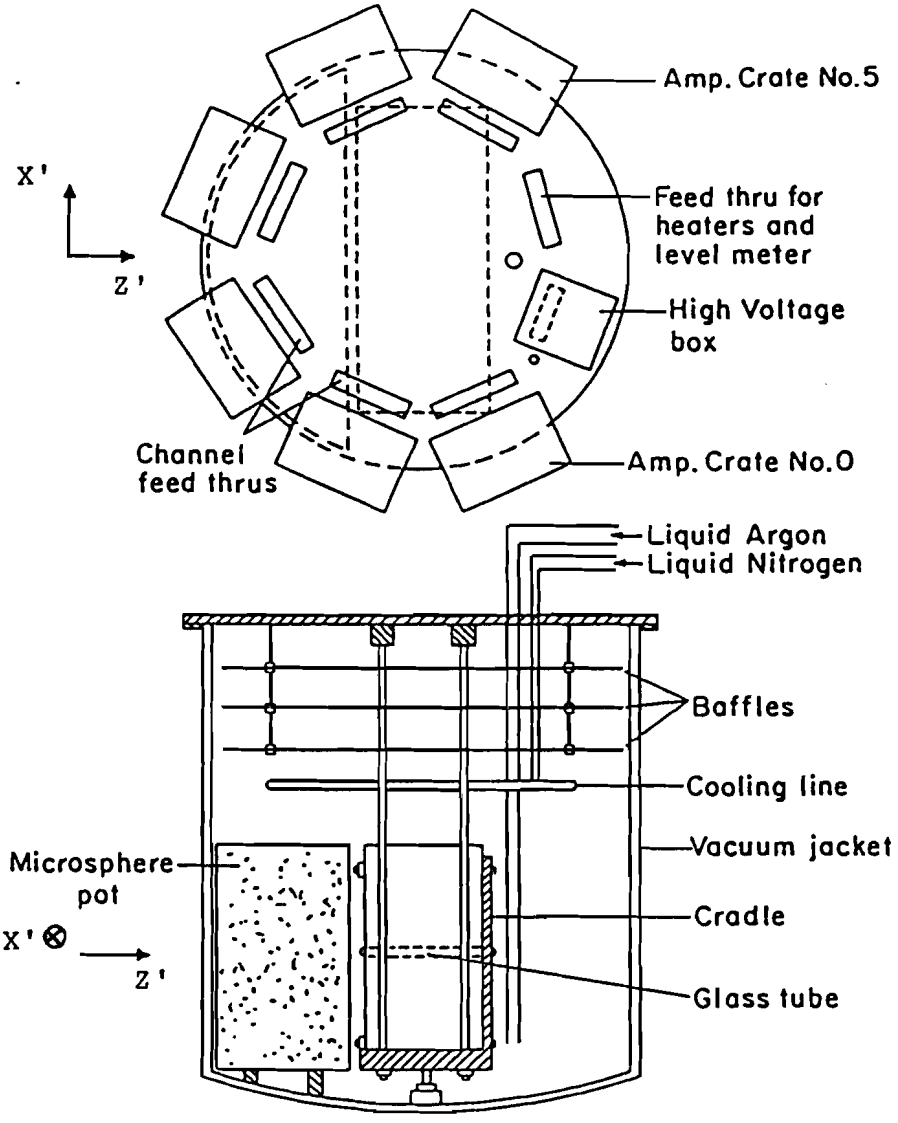
Amp. Crate No.5
Feed thru for heaters and level meter
High Voltage box
Amp. Crate No.0
Channel feed thrus
X'
Z'
Liquid Argon
Liquid Nitrogen
Baffles
Cooling line
Vacuum jacket
Cradle
Glass tube
Microsphere pot
X' ⊗
Z'

cryostat-cover plate assembly are shown in Figure 2.8. This vacuum-insulated vessel was supported in a steel tower which provided the means to raise and lower the cover plate and suspended detector. The tower could be moved on air pads to position the detector horizontally with respect to the beam. A set of jack screws allowed vertical positioning. The cylindrical shape of the cryostat made it necessary to include a thin-walled pot to displace the liquid argon in front of the detector. This container was packed with hollow glass microspheres (ρ~0.08 gm/cm^3) to prevent it from imploding when evacuated. The wall of the cryostat, the microsphere pot, and ~3 cm of liquid argon between the detector and the pot contributed ~0 .9 radiation lengths of material along the Z′ axis.

About 3000 liters of liquid argon were required to submerge the detector. Welding grade argon was cleansed of its oxygen content (usually less than 4 ppm) by passing the gas over a palladium catalyst with a small flow of hydrogen gas which combined with the oxygen to form water vapor. The water vapor was removed by passing the gas through room temperature dessicants that were followed by a molecular sieve operated at dry ice temperature. Oxygen content at the purifier output was typically a few tenths of a ppm. The purification system is depicted in Figure 2.9.

The purified gas was liquified in a storage dewar. It was transferred to the detector cryostat through a vacuum-insulated transfer line. An argon level indicator, made from a 3 cm wide strip of G-10 with 16 temperature sensitive resistors attached, was

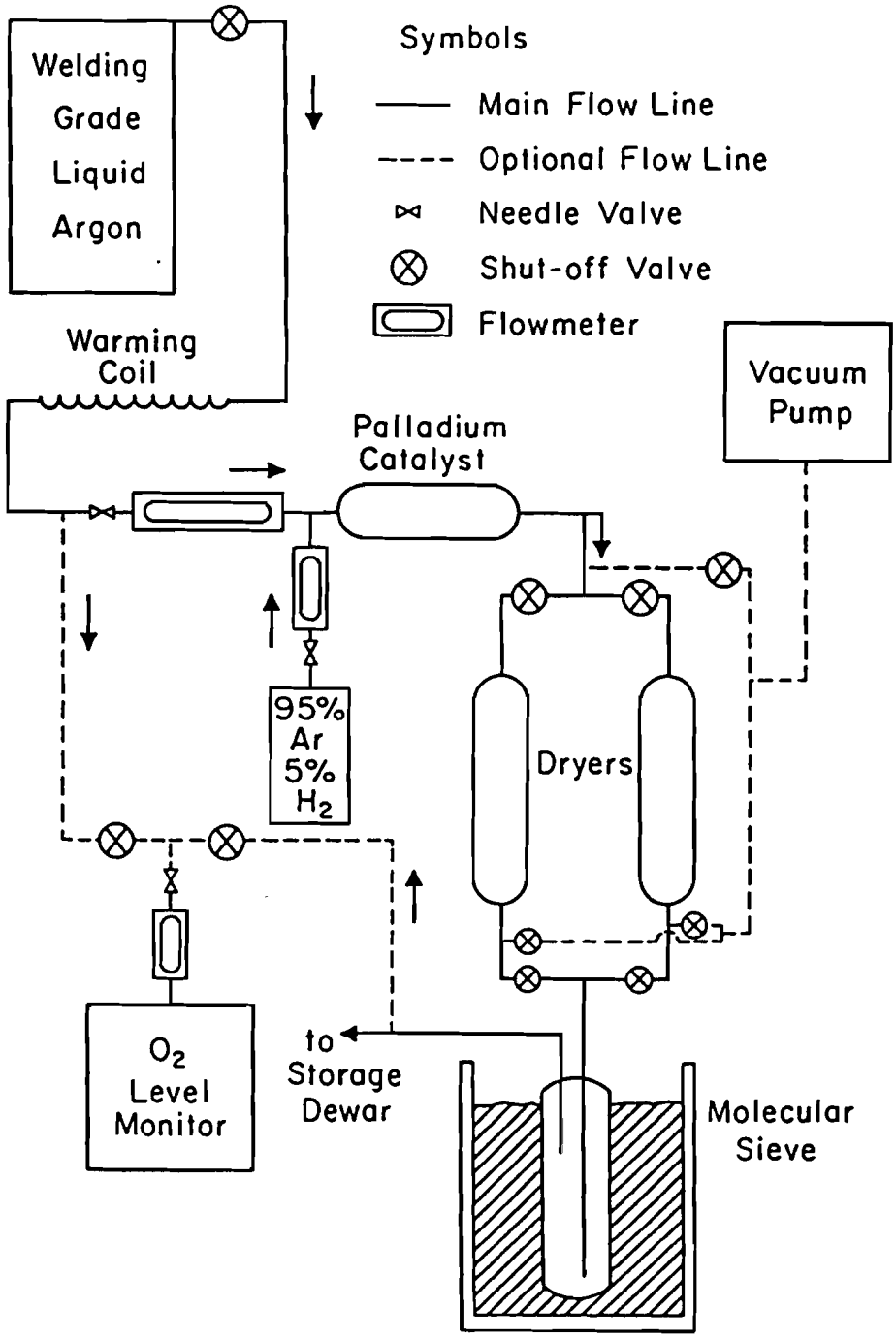
Welding
Grade
Liquid
Argon
Symbols
Main Flow Line
Optional Flow Line
Needle Valve
Shut-off Valve
Flowmeter
Warming
Coil
Vacuum
Pump
Palladium
Catalyst
95%
Ar
5%
H_2
Dryers
O_2
Level
Monitor
to
Storage
Dewar
Molecular
Sieve

Figure 2.9

monitored through cables led to a feed-thru on the cryostat cover plate. Cryogenic temperatures were maintained by sensing the liquid argon vapor pressure and controlling the flow of liquid nitrogen through internal cooling coils. The temperature gradient across the detector was monitored using temperature sensitive resistors placed at six locations on the detector. Six resistor-heaters were used to maintain the gradient at <10°C across the detector.

The ganged strips from the detector, with a total capacitance of 2-2.5 nf/channel, were connected to individual amplifier channels by multiconnector flat cables led to feed-thrus on the cover plate. The cables consisted of two 0.025 mm thick copper layers separated by 0.13 mm thick mylar. The top layer was divided into 0.64 cm wide strips, one per channel. The back layer served as ground. The equivalent impedance of the cables was ~10Ω. Each cable was back terminated at the connection points to the detector strips by 10Ω resistors. The cable impedance was only approximately matched to that of the amplifiers (~40Ω at 0.1 - 30 MHz). Consequently, the cables were properly terminated only at one end. This did not cause difficulty (e.g. ringing) because intrinsic rise time of the input pulses were governed by the drift velocity of electrons in the liquid argon; pulse rise times were typically ~250 nsec.

Figure 2.10a is a block diagram of the front-end electronics for the detector [2.14]. Each channel consisted of a charge-sensitive amplifier, a delay line, a fast trigger pick-off amplifier, two sample and hold circuits, and a difference amplifier. The charge-sensitive

Figure 2.10

a) Electronics for one channel of LAC

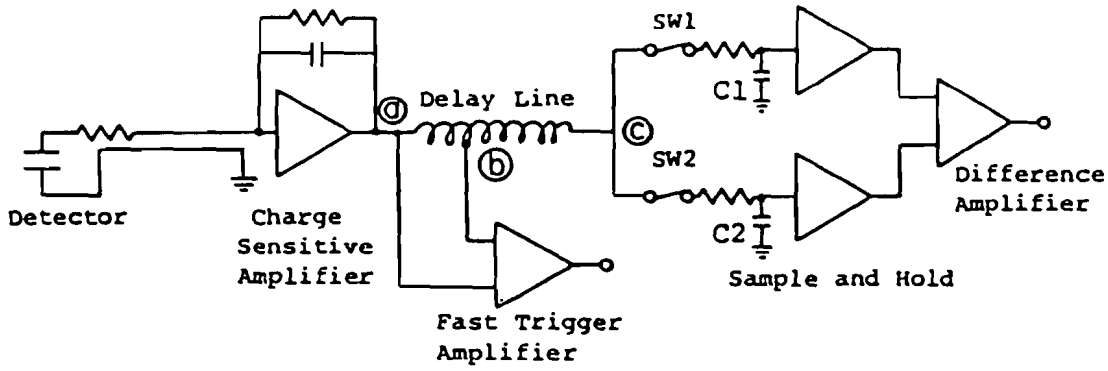

b) Signal at point ©

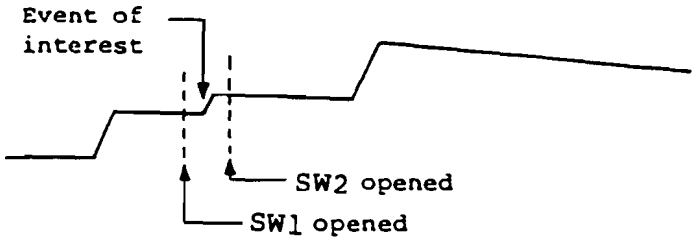

c) Read-out system

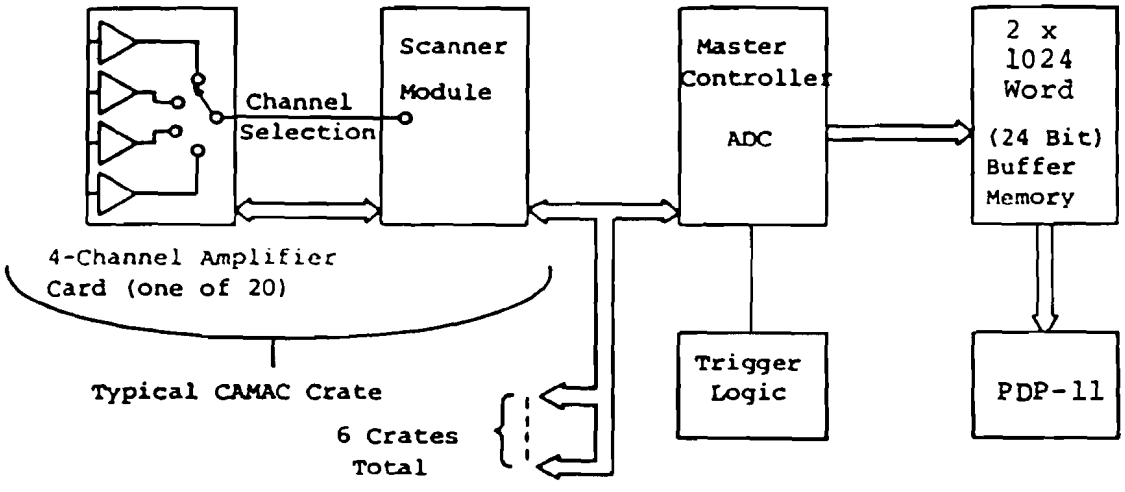

amplifiers had a gain-bandwidth of 100 MHz, a rise time on the order of 120 nsec, and were approximately matched to the detector capacitance. The amplifier response, folded in quadratically with the intrinsic LAC pulse rise time, did not have a large effect. These amplifiers were used to integrate the charge generated by the electromagnetic shower. They were designed to have a large dynamic range (~10/1) compared to the largest expected input pulse. This permitted the RC-decay time to be relatively long with little chance of saturation even at high interaction rates. A time constant of ~20 μsec was used for the front X and Y strips. For the back half, 400 μsec was used.

The output from the amplifiers (point a) appears as the series of steps shown in Fig. 2.10b, each step corresponding to an interaction. The amplifier output is delayed by a 400 nsec lumped delay element to allow time for a trigger decision to be made from a fast output generated by a difference amplifier looking at the input (a) and a 200 nsec tap on the delay line (b). The fast trigger outputs provided signals roughly proportional to the energy deposition and could be appropriately weighted, summed, and discriminated to form an overall calorimeter trigger decision.

If an event was triggered on, CMOS switch SW1 was opened just prior to the pulse arrival and C1 stored the baseline. After a suitable time, SW2 was opened. The difference in charge between C1 and C2 was proportional to the energy deposited in the detector. In principle, the dead time for this scheme is determined only by the

rise time of the incoming pulse. An advantage this method offers over single switch sample-and-hold designs is that small noise charges injected onto the holding capacitors when the switches open tend to cancel out in the difference amplifier, improving pedestal stability and reducing system noise in the analog outputs.

As indicated in Fig. 2.10c, four amplifiers were placed on a single card and twenty cards, along with a scanner module, were mounted in a CAMAC crate. Scanners in each of six crates were connected to a master controller with a 12-bit analog-to-digital converter (ADC). After the trigger was set, the controller activated the crate scanners. Each scanner selected an amplifier card within its crate and one of the four channels on that card. It then multiplexed the sample-and-hold analog output of that channel and passed data to the master controller. The controller module digitized the signal and sent the digitized result, along with 12 bits of channel address information, to one of two 24-bit CAMAC buffer memory modules. After all channels were digitized, the buffer memories were read out by the PDP-11 on-line data acquisition computer.

Each amplifier fast output in the front X view was cabled to a time-over-threshold discriminator. The leading edge of each pulse was timed relative to the final trigger definition using 8-bit/channel time-to-digital-converters (TDC). These digitized times of arrival were very useful in the off-line analysis for dealing with pile-up from out-of-time events, even at high data rates.

A system was implemented to calibrate the LAC electronics. Each difference amplifier had a DC offset to ensure a positive output signal even if no energy had been deposited in that channel. These "pedestal" values had to be determined in order to calculate strip energies. They were measured by reading out the detector between spills when there was no energy in the LAC. The stability of the amplifier gains was monitored by using a pulser to inject a signal into the detector before reading it out.

F. Trigger

The beam-target interaction rate in hadronic experiments (in the MHz range) is normally far higher than what can be recorded for future analysis. Triggers select interesting events, reducing the data-acquisition rate to more manageable levels of the order 10-100 Hz. The goal of this experiment was to measure the production of neutral particles (γ, π^0, η, etc.) at high p_T. During a one second beam spill, there were $\sim 10^6$ interactions in the target, most of which were at low p_T. To discriminate against low p_T events, the energy deposited in the LAC was weighted according to its position in the detector to estimate the transverse momentum of the event. The trigger consisted of a coincidence between a beam-target interaction, which defined a pretrigger signal, and the presence of a large amount of p_T localized in a small region of the LAC. Several veto signals in anticoincidence with the pretrigger were used to reject events under

certain conditions.

Figure 2.11 shows the overall trigger logic. The pretrigger logic used signals from the beam hodoscope, in coincidence with a reference pulse from the main ring (labeled "beam gate" in Fig. 2.11), to define "INCIDENT BEAM". Veto counters just downstream of the beam hodoscope suppressed triggers due to beam halo. Two sets of counters downstream of the targets, situated just outside of and straddling the beam region, detected the charged particles produced in beam-target interactions. Each set covered roughly the same solid angle as the LAC. A logical OR of the pulses from these counters in coincidence with incident beam and veto signals, defined an "INTERACTING BEAM" requirement. When this occurred in coincidence with a "COMPUTER READY" signal, the "PRETRIGGER" latch was set. Each pretrigger generated its own reset pulse, which was sent down a delay line. The pretrigger pulse, in anticoincidence with the vetos discussed later in this section, defined a "STROBE" signal. A coincidence between a strobe and p_T information from the LAC defined a trigger. The delay of the pretrigger reset pulse allowed sufficient time for the LAC to collect charge and form the fast output signals used by the p_T trigger logic. If all trigger requirements were met, the pretrigger reset pulse was inhibited before it could initiate the clearing of various trigger latches.

A set of trigger modules were cabled to the fast outputs of the LAC amplifiers. These modules were used to define two p_T requirements: (1) the total (global) p_T deposited in the LAC (a

Figure 2.11

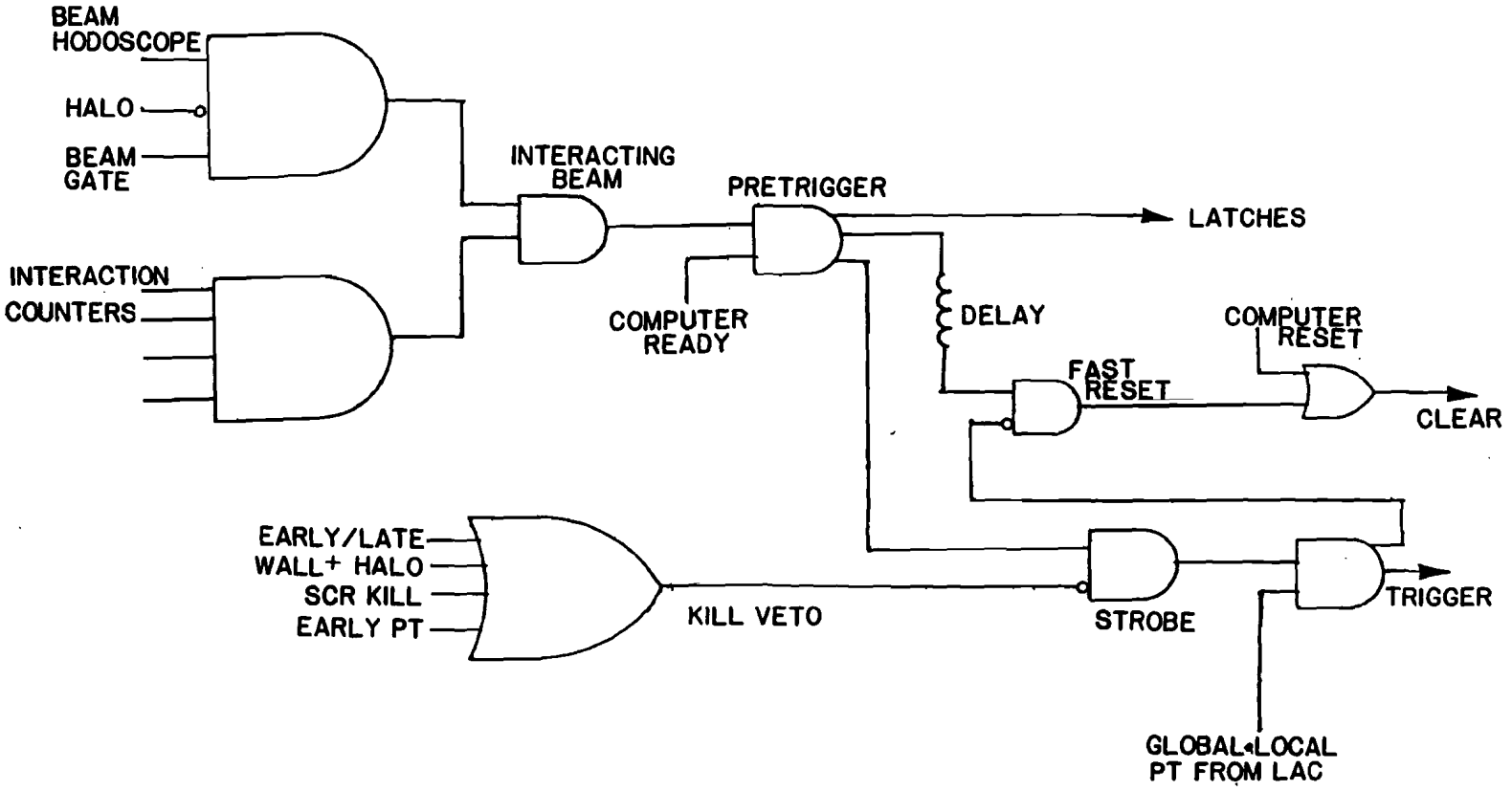
BEAM HODOSCOPE
HALO
BEAM GATE
INTERACTION COUNTERS
INTERACTING BEAM
PRETRIGGER
LATCHES
COMPUTER READY
DELAY
COMPUTER RESET
FAST RESET
CLEAR
EARLY/LATE
WALL+ HALO
SCR KILL
EARLY PT
KILL VETO
STROBE
TRIGGER
GLOBAL◂LOCAL PT FROM LAC

simplified schematic of the circuit is shown in Figure 2.12a), and (2) the "local" p_T (depicted in Fig. 2.12b).

The p_T of a photon in the LAC is given by

$$p_T = p_T \sin\theta = E_\gamma \sin\theta,$$

where θ is the laboratory angle between the beam direction and the direction of the photon. The LAC was displaced from the beam axis in the X-direction and centered in Y. Thus the Y-component of p_T was relatively small. For triggering purposes, the total p_T was approximated by the X-component alone. Most of the energy in an electromagnetic shower was deposited in the front half of the LAC. Therefore, only the front X′-strips were used to define global p_T.

The global p_T trigger was susceptible to coherent noise (noise common to all LAC channels, such as pickup from magnet power supplies). It could also be satisfied by multiphoton events in which each photon carried a low p_T. The fine granularity of the LAC made it possible to suppress these triggers by demanding that events satisfy a "local" p_T condition; a substantial fraction of the global p_T had to be deposited in a region of limited spatial extent, roughly the size of a single shower. The global p_T trigger threshold was set to a nominal value of 2.2 GeV/c, using a 35 GeV electron beam incident on selected regions of the LAC; the local p_T requirement was that at least 600 MeV/c of this p_T be concentrated in one "clump" [2.15]. This condition suppressed events in which there were no π^0 or η mesons produced with p_T above 1.2 GeV/c. Demanding localized energy

Figure 2.12

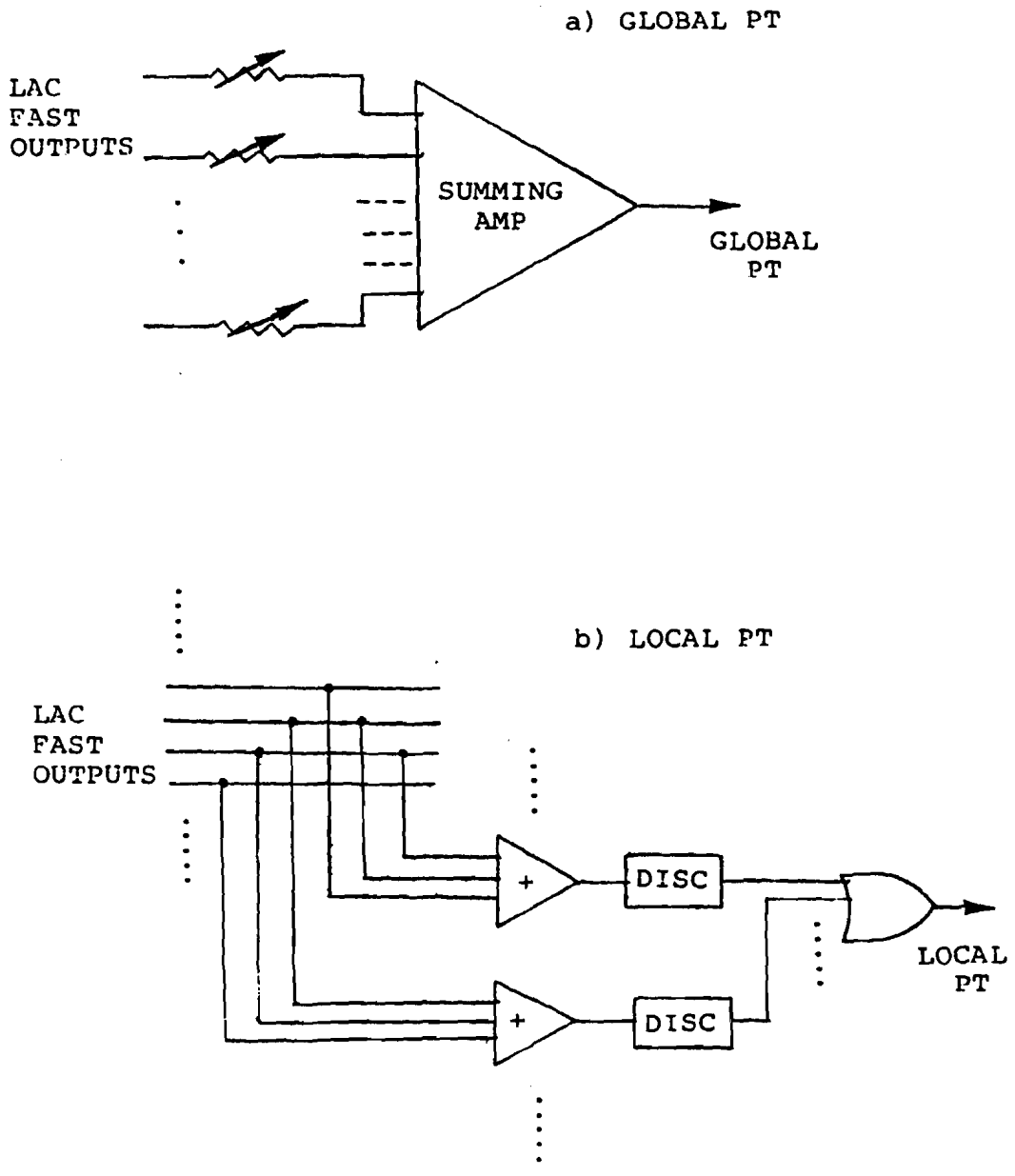
a) GLOBAL PT
LAC
FAST
OUTPUTS
SUMMING
AMP
GLOBAL
PT
b) LOCAL PT
LAC
FAST
OUTPUTS
+
DISC
+
DISC
LOCAL
PT

deposition reduced the trigger rate by roughly a factor of two.

The global p_T trigger circuit was essentially a set of adjustable resistors weighting the inputs of a summing amplifier. The global p_T was estimated by performing an analog sum over appropriately weighted front strip energies in the X′-projection,

$$p_T^{global} = \sum_i \alpha_i E_i^x,$$

where α_i is the weighting factor for strip i and E_i^x the energy. If this weighted sum exceeded the threshold set on a discriminator module, the global p_T requirement was satisfied.

For the i-th X′-strip, with its center located a distance x_i from the beam axis and a distance r_i from the target, $\sin\theta_i = x_i/r_i$. Since r_i ~ constant for all strips, $\sin\theta_i \propto x_i$. Initially, the values of α_i were proportional to x_i. This resulted in a fixed p_T trigger threshold [2.16] across the detector. With a fixed threshold, the vast majority of the events were observed to lie in the region of the LAC closest to the beam (the inside). In order to utilize the entire rapidity range the detector provided, the weights were adjusted to yield a position-dependent trigger threshold. Strips relatively far from the beam were weighted essentially in proportion to x_i; toward the inside of the LAC, the weights decreased faster than x_i. Strips nearer to the beam therefore contributed less to the global p_T sum than for the case of a "sinθ" weighting. A shower incident near the inside edge of the LAC had to carry more p_T to fire the discriminator

than one farther away from the beam. Thus, the trigger threshold was effectively higher on the inside. This tended to equalize the data accumulation rate across the active area.

In order to measure the global p_T threshold and to determine the trigger efficiency curve, a prescaled multiple-trigger threshold scheme was implemented (Figure 2.13). The global p_T analog signal was fanned out to two discriminators. One was set to the nominal 2.2 GeV/c threshold used in the first part of the run, and the other to a lower threshold corresponding to 1.6 GeV/c. A prescaler counted events taken with the normal trigger. The prescaler output was latched on after two events were recorded in this mode. This signal caused the low threshold trigger mode to be selected. The status of both triggers was latched and recorded on tape for each event. The prescaler was reset by the same signal used to clear the other latches (Fig. 2.11). The fraction of events recorded while the low threshold mode was selected, which failed to meet the high threshold trigger conditions, determined the trigger efficiency at a given p_T. The procedure for measuring efficiency curves is discussed further in Chapter 5.C.

Approximately 85% of the energy, and hence the p_T, of an electromagnetic shower was deposited in three strips of the LAC. The local p_T condition was defined in terms of the energy deposited in three contiguous front X′-strips by

$$p_T^{local} = \text{Max} \left[\sum_{i-1}^{i+1} \beta_i E_i^x \right] .$$

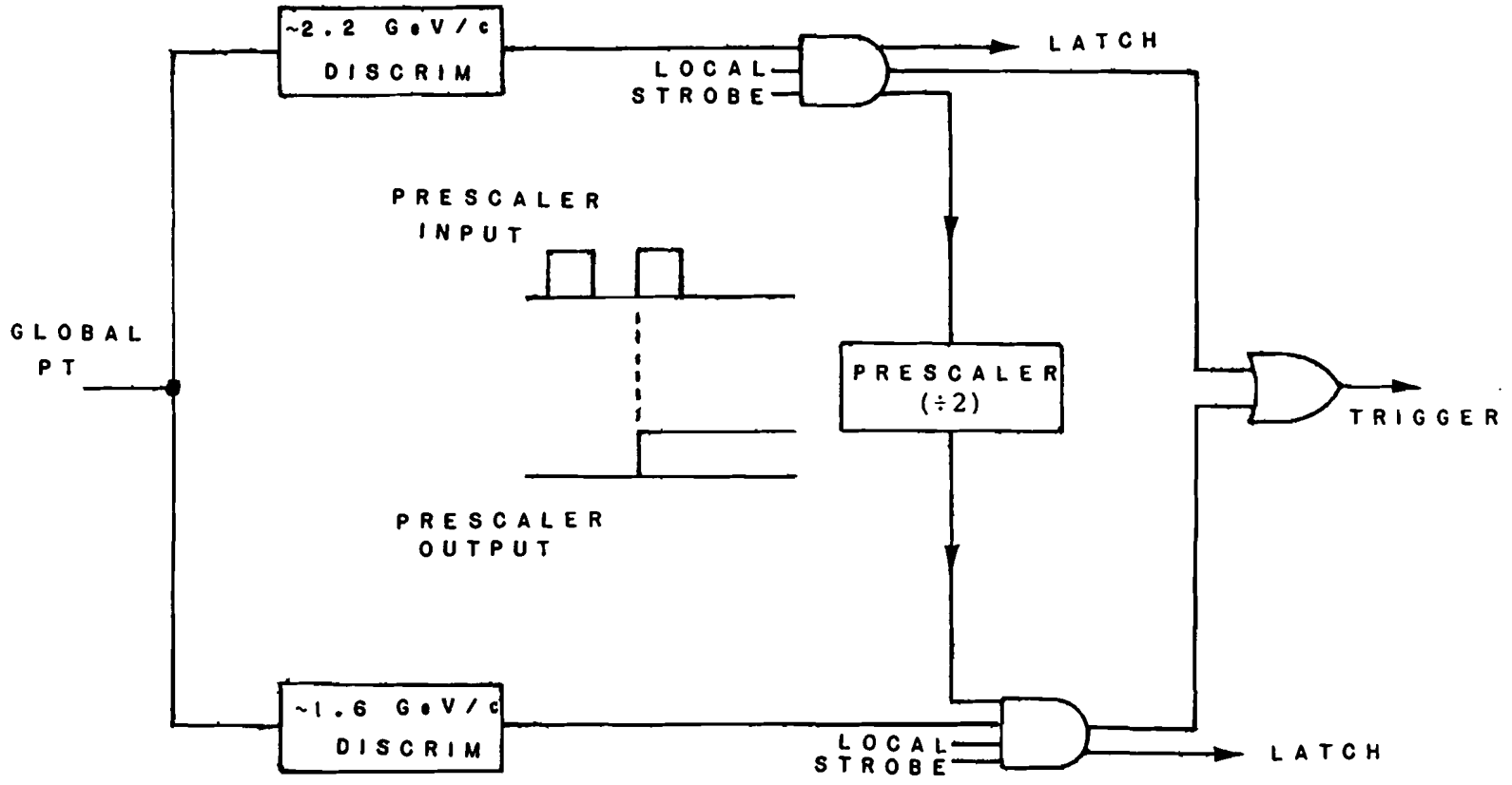
~2.2 GeV/c
DISCRIM
LOCAL
STROBE
LATCH
PRESCALER
INPUT
GLOBAL
PT
PRESCALER
(÷2)
TRIGGER
PRESCALER
OUTPUT
~1.6 GeV/c
DISCRIM
LOCAL
STROBE
LATCH

Figure 2.13

The β_i are weighting factors ($\sin\theta_i$ weighting for local p_T). The local p_T trigger, shown in Fig. 2.11b, consisted of a set of discriminators each cabled to a group of three strips. A logical OR of all the discriminator outputs was formed. Any group summing to a value exceeding the local p_T threshold satisfied the local p_T requirement.

The environment in which this experiment was conducted was electrically noisy. Particularly serious were the huge noise spikes generated by silicon controlled rectifiers (SCRs) used in magnet power supplies. This noise was detected by the LAC amplifier channels, typically producing signals of 100 mV - 1 V in the global p_T sum. Each pulse rang for several microseconds, and the typical SCR noise rate was a few kilohertz. An SCR noise veto was implemented. A photon in the detector produced a global p_T sum of negative polarity with a small positive overshoot. The SCR spikes oscillated between positive and negative polarities. A discriminator set to a low positive threshold sensed the onset of an SCR spike; a 10 μsec wide pulse was generated which caused the experiment to be switched off until the oscillations were damped out.

Because of the high event rate (~1MHz) at which the argon detector was operated, it was necessary to use pile-up vetos to protect against the situation in which an apparent high p_T event was in reality a superposition of two successive lower p_T interactions. An early interaction veto eliminated events in which an interaction occurred up to 200 nsec earlier than the one associated with the pretrigger. An early p_T veto was also used. If the global p_T signal

had been above 800 MeV/c and if the local p_T requirement had been met up to 250 nsec before the prompt time, the event was rejected.

Another problem was caused by particles produced in beam interactions far upstream of the target hitting the LAC in random coincidence with an interaction in the target. A veto signal from a wall of scintillation counters that shadowed the LAC suppressed these triggers for an interval 200 nsec before and 50 nsec after the trigger time [2.17].

To summarize, the basic trigger was defined as

$$\text{TRIGGER} = \text{PRETRIGGER} \cdot \text{GLOBAL PT} \cdot \text{LOCAL PT} \cdot \overline{\text{VETO}}$$

where

$$\text{PRETRIGGER} = \text{BEAM HODOSCOPE} \cdot \overline{\text{HALO}} \cdot \text{COMPUTER READY} \cdot \text{INTERACTION}$$

and

$$\text{VETO} = \text{SCR} + \text{EARLY INTERACTION} + \text{EARLY PT} + \text{VETO WALL.}$$

G. On-line Monitoring and Data Acquisition

Whenever the trigger was satisfied, the experiment was turned off and various readout systems digitized data for that event. The on-line PDP-11/45 computer read out information via a CAMAC interface and wrote data onto magnetic tape. A schematic diagram of the data

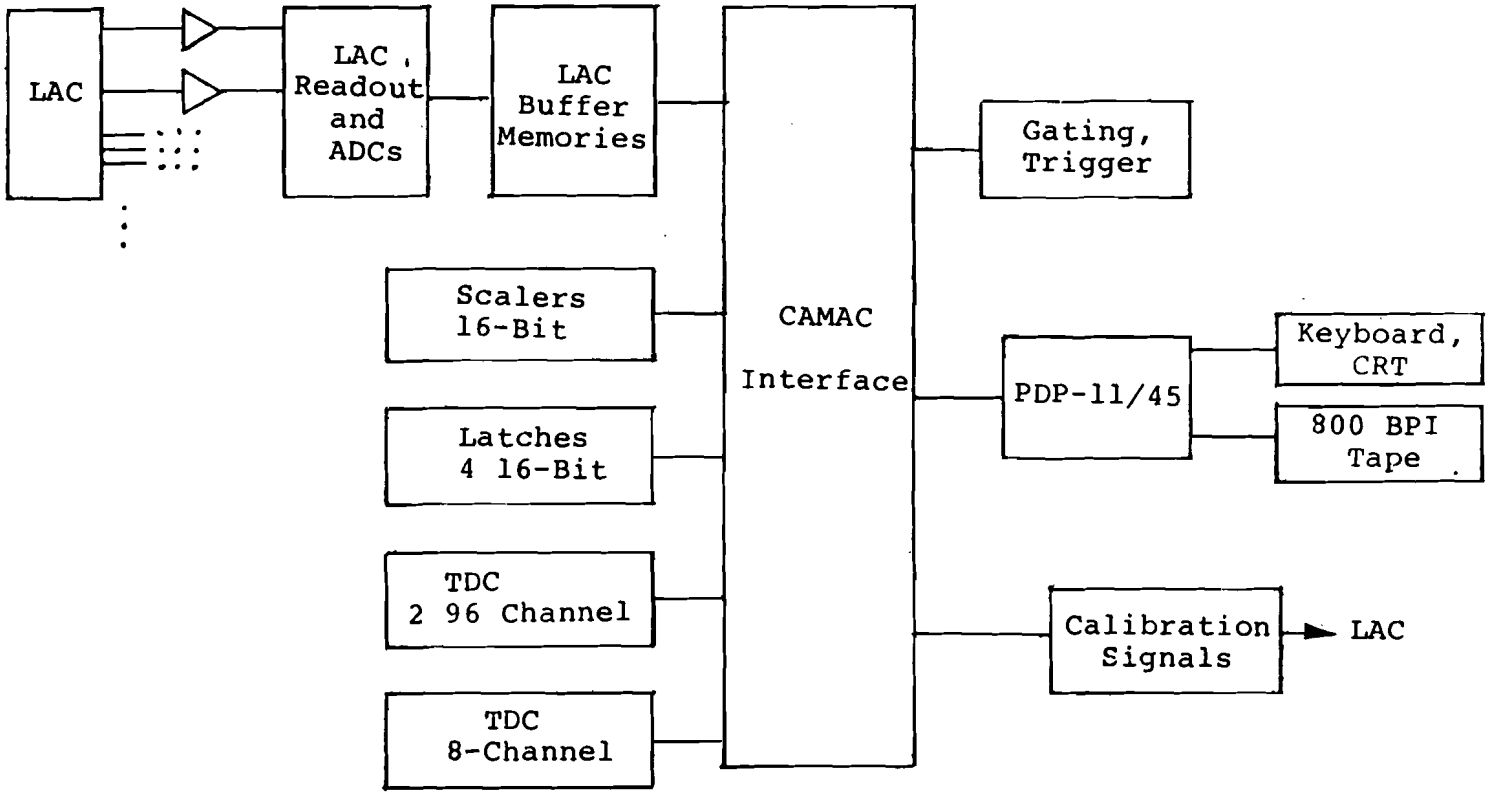
LAC
LAC Readout and ADCs
LAC Buffer Memories
Gating, Trigger
Scalers 16-Bit
CAMAC Interface
Keyboard, CRT
PDP-11/45
800 BPI Tape
Latches 4 16-Bit
TDC 2 96 Channel
Calibration Signals
LAC
TDC 8-Channel

Figure 2.14

acquisition system is shown in Figure 2.14.

The pretrigger signal set four 16-bit registers (LeCroy 2341) and an 8-channel TDC (LeCroy 2228). The 16-bit registers were used to latch the beam hodoscope elements, Cerenkov counter, and signals from the scintillation counters. Owing to a shortage of latch registers, the TDC was used to record the status of the multiple-threshold trigger. If a final trigger was generated, these modules were read out to CAMAC. Otherwise, they were cleared.

The final trigger generated a common stop pulse for two LeCroy 2770A 96-channel TDCs used to time energy deposition in the LAC. Low threshold discriminators (5 mV, or ~500 MeV) provided individual start signals for each TDC channel. The time intervals between start and stop pulses were digitized and read out. The final trigger also initiated the LAC readout.

Two classes of scalers were written to tape. One class (LeCroy 2551) was read out and cleared after each event. The other class (Jorway Model 84) was read out after each spill. Some were cleared after each spill, while others were reset only at the start of a run. This provided an independent means of measuring various rates. The scalers recorded the beam count, the coincidence rate between the beam hodoscope and Cerenkov counter, the strobe rate, and the pretrigger rate. This information was used to determine the proton and pion beam flux for cross section normalization. Also recorded were counting rates for the trigger veto signals, the interaction counters, and the global p_T trigger. This data was useful during the run for debugging

and monitoring the apparatus. Rates for a typical run are listed in Table 2.2.

Monitoring and calibration of the LAC was controlled by the on-line program [2.18]. The LAC amplifier channels were pulsed between spills and read out for tests and off-line calibration. The experiment was monitored during data acquisition through dumps, histograms, plots, and event displays provided by the on-line software.

Data were written to tape at 800 BPI. A typical run, consisting of ~400 spills and ~8000 triggers per tape could be completed in roughly 75 minutes. The event rate was determined by the P_T trigger threshold. It was limited by the time required for the on-line computer to collect the data (~10 msec). The computer dead time scaled in proportion to the rate. At 20 events per spill, the dead time incurred was held to a reasonable level (~20%).

The data analyzed in this thesis consisted of ~55 tapes, obtained in February and March of 1981. Data were taken with three nuclear targets (discussed in section C) and also with no target present (for background subtraction).

COUNTING RATE/SPILL	
INCIDENT BEAM	7.2×10^6
EFFECTIVE BEAM*	4.4×10^6
INTERACTING BEAM	800,000
PRETRIGGERS	430,000
STROBES	280,000
GLOBAL P_T SINGLES RATE	20,000

VETOS/SPILL (SINGLES RATES)	
EARLY P_T	20,000
EARLY/LATE INTERACTION	140,000
VETO WALL+HALO	100,000
SCR	10,000

TRIGGERS/SPILL	20

* See Chapter 4.G.

TABLE 2.2. TYPICAL RATES

CHAPTER 3

Event Reconstruction

A. Introduction

The first stage of the off-line data analysis involved the reconstruction of photons from raw pulse height information recorded on the 800 BPI data tapes. The pulse heights for the 480 LAC channels were converted into units of energy prior to reconstruction. To accomplish this, it was necessary to measure the amplifier zero-offsets ("pedestals") and relative gains for each channel, and to determine an overall normalization factor which established the absolute energy scale. This calibration procedure is described in section B.

The photon reconstruction procedure (1) searched the X and Y views of the detector for clusters of energy (the "primed" system of

Chapter 2 is used exclusively in this Chapter -- primes will be dropped), and (2) correlated clusters in different views on the basis of energy matching, allowing for the energy resolution of the detector. The energy, position, and mass resolution of the LAC is discussed in section C. The method used to determine the E629 lateral shower profile is described in section D. The reconstruction algorithms are described in sections E and F.

B. Liquid Argon Calorimeter Calibration

The digitized signal from each strip was converted into units of energy as follows:

$$E_i = AG_i\ (N_i - N_{0i})$$

where

E_i = energy in ith strip,

A = overall normalization factor,

G_i = relative gain for channel i,

N_i = raw ADC counts for channel i,

and

N_{0i} = pedestal for channel i.

"Pedestals" are effective zero-levels for LAC channels. Pedestal levels had to be subtracted from the recorded LAC pulse heights. Their values were determined mainly by the DC offsets of the

difference amplifiers. Another effect also contributed. The time required to collect electrons drifting through liquid argon was on the order of a few hundred nanoseconds. The mobility of positive ions was much lower; their drift velocities were typically 3-4 orders of magnitude less than those of electrons. These ions induced DC currents in the amplifier outputs which resulted in pedestal fluctuations.

Each channel had a slightly different amplifier gain, G_i. These differences in the relative gains had to be measured and corrected for. In order to convert LAC ADC information into units of energy, an overall conversion factor, A, had to be determined. Calibration of the liquid argon calorimeter involved measuring these parameters.

As described in Chapter 2.E, pedestals were measured between beam spills by reading out the LAC when no energy was present. Electronic noise caused the pedestal values to fluctuate. Figure 3.1 is a plot of the pedestal values for front X and Y strips in a typical run. The error bars show the magnitude of the fluctuations over the course of this run.

Pedestal shifts over the course of a single run, which lasted roughly an hour, were not appreciable. To account for possible drifts over longer time intervals, an average pedestal value for each strip was determined and used for individual runs [3.1]. These average values, identified by run number, were stored in a calibration file read by the reconstruction program.

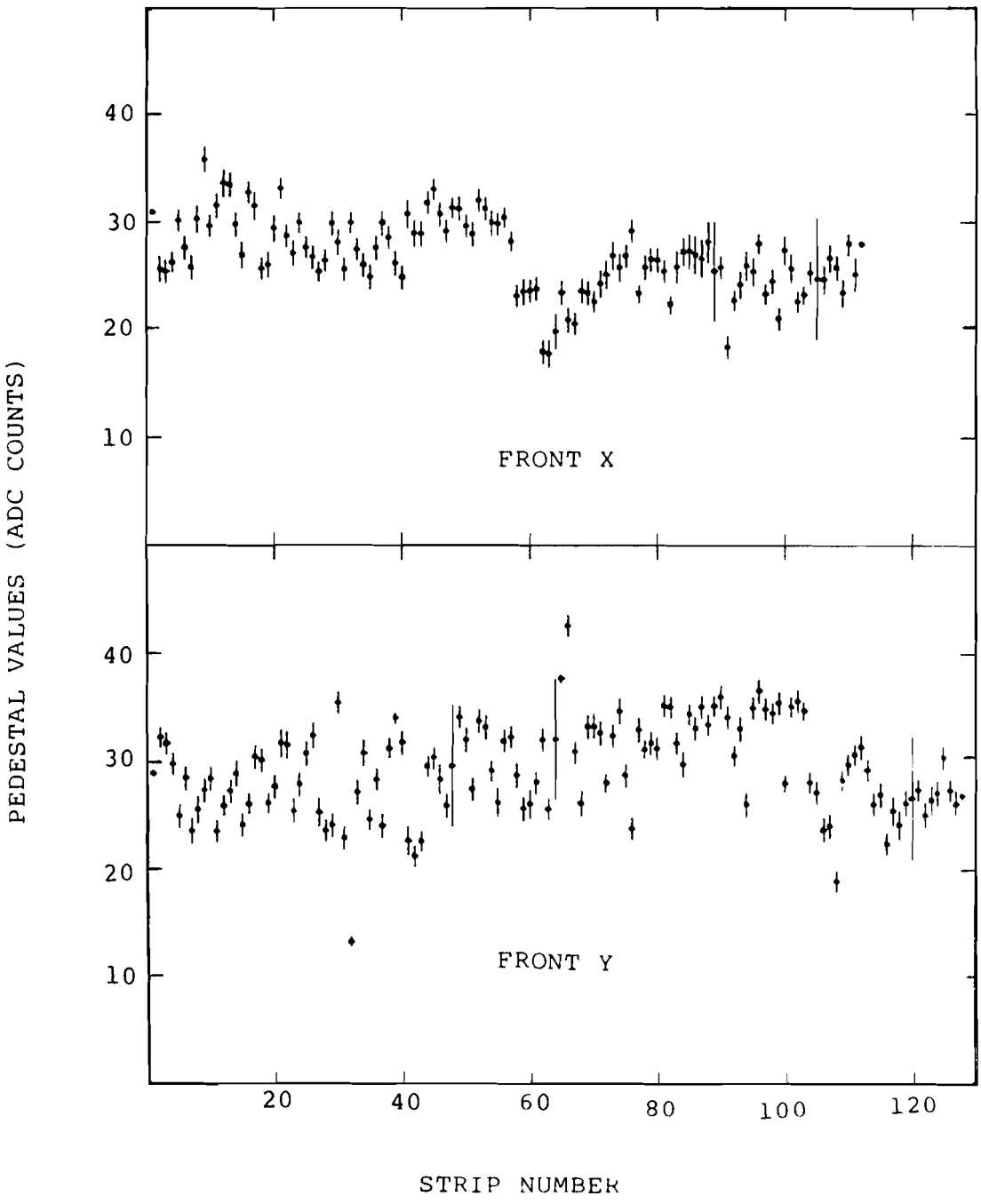
PEDESTAL VALUES (ADC COUNTS)
40
30
20
10
FRONT X
40
30
20
10
FRONT Y
20
40
60
80
100
120
STRIP NUMBER

Figure 3.1

Two separate systems were used to measure and monitor the stability of the LAC amplifier gains. Relative electronic gains were measured after the data run by disconnecting amplifiers from the detector, injecting standard test pulses directly into the inputs, and reading out the signals. Relative gains were determined to an accuracy of ~3%. Gain stability over the course of the experiment was monitored on a run by run basis by capacitively coupling pulses to strips in the LAC between spills and reading the detector out (Chapter 2.E). It was established that the gains shifted by less than 3% over the course of the experiment [3.2].

The overall normalization factor, A, was determined by normalizing the observed mass of the π^0 to the accepted value (135 MeV/c^2). The factor was initially assigned an approximate value based on analysis of events on-line. This value was adjusted after the first reconstruction pass [3.3]. The conversion factors (AG_i) for the front X and Y strips are plotted in Figure 3.2 [3.4].

C. LAC Resolution

Bremsstrahlung and pair production govern the longitudinal development of an electromagnetic cascade shower. The lateral spread is mainly due to multiple Coulomb scattering of electrons [3.5]. These processes are responsible for statistical fluctuations in the longitudinal and lateral shower profiles which limit the position and energy resolution that can be achieved in a detector. Effects such as

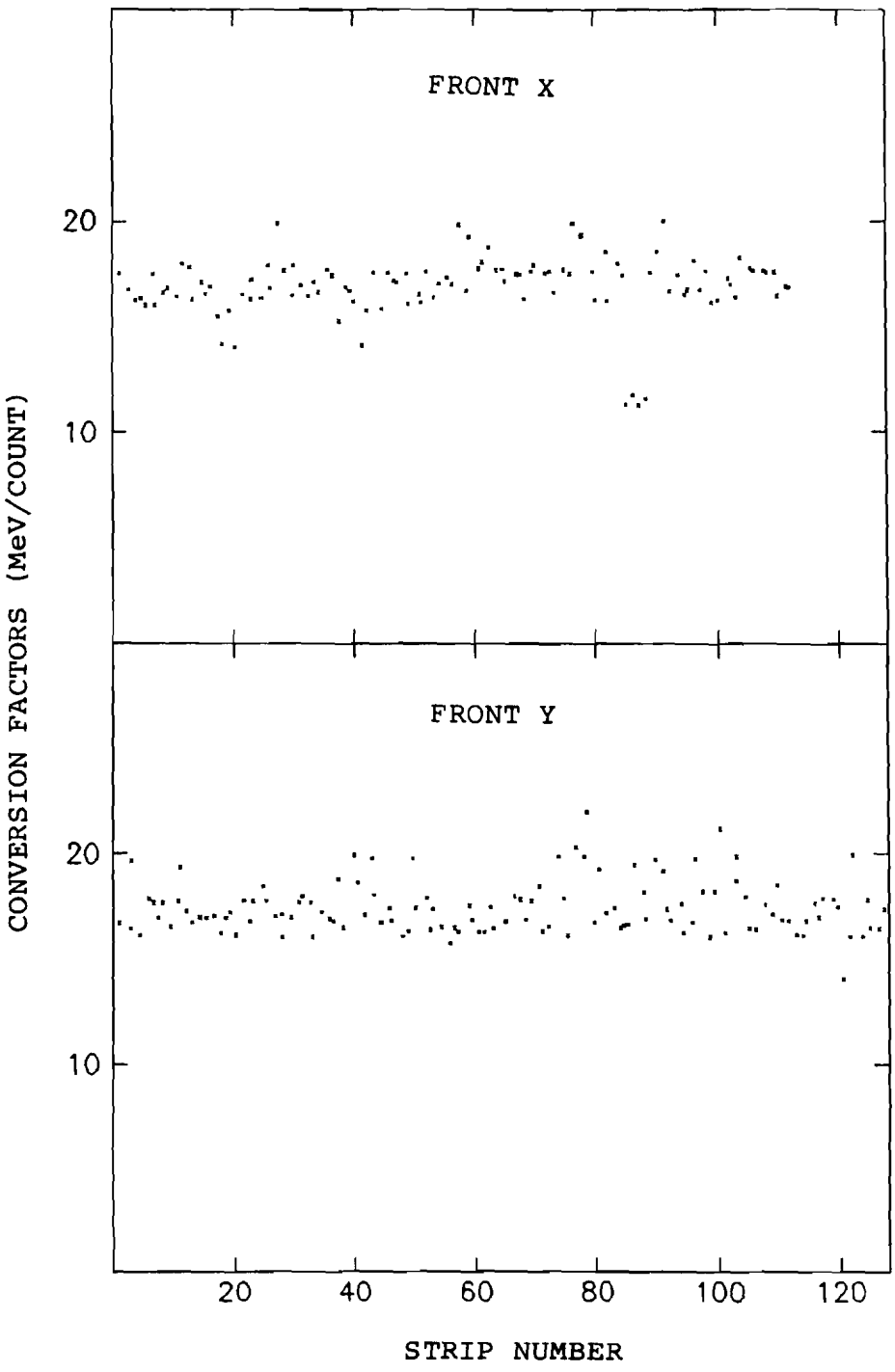
FRONT X
20
10
FRONT Y
20
10
CONVERSION FACTORS (MeV/COUNT)
20
40
60
80
100
120
STRIP NUMBER

Figure 3.2

pedestal fluctuations and amplifier noise also affect the resolution.

The reconstruction procedure correlated showers in different projections of the LAC by comparing their energies. The X and Y readout planes provided two independent energy determinations, each having an uncertainty approximately a factor $\sqrt{2}$ worse than the overall error. Good energy resolution was essential in order to reliably correlate the projections.

Another important aspect of the detector is the linearity of its energy scale. (The linearity of the algorithm used to calculate photon energies from the pulse height data is also important. In general, throughout this section, references to aspects of the "detector" performance also encompass reconstruction effects, unless the context indicates otherwise.) A single photon is more energetic than either of the decay photons from a π^0 of the same p_T. A nonlinear response to photons of different energies would lead to a systematic shift in the p_T scale for single photons relative to π^0's. Because cross sections vary rapidly with p_T, a small shift would lead to large uncertainties in the γ/π^0 ratio.

Good position resolution was necessary in order to resolve photons from energetic π^0 decays. A failure to observe these photons would have led to a background in the direct photon signal at large p_T. Although an energy-weighted average over strip positions (center of gravity) is the simplest way to calculate shower coordinates, it does not yield the true position [3.6]. The energy distribution in an electromagnetic shower falls approximately exponentially with distance

from the shower axis, a general feature shared with hadronic showers. The center of gravity of the energy within a single strip does not coincide with the strip center; this is basically the source of the systematic bias. An empirical formula was derived from the measured shower profile (section D) for calculating positions. Fluctuations in the lateral development of a shower limit the position resolution that can be achieved. They are generally worse for hadronic showers.

The invariant mass of a neutral meson decaying into two photons of energy E_1 and E_2 with opening angle θ (Figure 4.9) is given by

$$m^2 = 2E_1E_2(1 - \cos\theta). \tag{3.1}$$

The accuracy of the mass measurement is

$$\frac{\Delta m}{m} = \frac{1}{2}\left[\left(\frac{\Delta E_1}{E_1}\right)^2 + \left(\frac{\Delta E_2}{E_2}\right)^2 + \left(\frac{4E_1E_2}{m^2} - 1\right)\Delta\theta^2\right]^{1/2}. \tag{3.2}$$

It depends both on the energy and position resolution of the detector. In events with high photon multiplicity, poor mass resolution leads to an enhanced probability for pairing a photon with the wrong partner. In order to get a sharp mass peak and to cleanly separate signal from background, it is important to have good mass resolution.

The LAC was calibrated in E272 (1978-79) using a 50 GeV electron beam [3.7]. The response of the detector to positrons as a function of their momenta (in the range 20-100 GeV/c) was studied using $K^+ \to \pi^0 e^+ \nu$ decays. (These E272 data and the E629 π^0 mass studies

described below test both the detector response and the performance of the reconstruction algorithm.) The E272 spectrometer used four stations of drift chambers and an analyzing magnet for charged particle momentum analysis. It was not possible to repeat these calibration studies in E629. Since no physical modifications were made to the LAC prior to the running of E629, the position and energy resolution were assumed to be essentially the same. As discussed below, studies of the π^0 mass as a function of energy, and of the width of the mass peak, supported this assumption.

The energy resolution of the LAC, expressed in a customary form, was $\sigma(E)/E = 10.3\%/\sqrt{E}$ (GeV) for the 50 GeV E272 electron calibration. This is comparable to the resolution other groups have obtained with liquid argon calorimetry. For example, Cobb et al. [3.8] reported an energy resolution of $\sigma(E)/E = 10\%/\sqrt{E}$ (GeV) for their detector in an electron beam at various energies in the range 0.75-40 GeV.

In the 50 GeV calibration runs, the beam intensity was low, only one particle was incident on the LAC per event, data were taken over short periods of time, and reconstruction parameters were tuned to achieve the best results. Under normal experimental conditions, resolutions are somewhat worse. The $K^+ \to \pi^0 e^+ \nu$ data provides an indication of how the LAC performed under actual running conditions.

The energy resolution for photon showers is presented in Figure 3.3a. The dashed line is a fit to the data:

$$\sigma^2(\text{GeV}) = [\ (0.14\sqrt{E}\ (\text{GeV})\ ]^2 + (0.55)^2, \qquad (3.3)$$

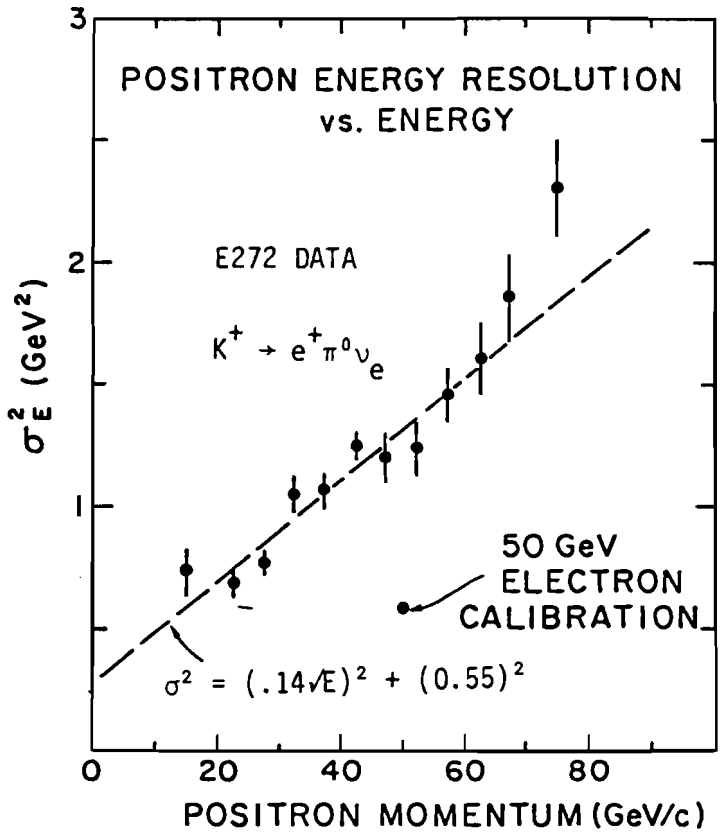
a)
POSITRON ENERGY RESOLUTION
vs. ENERGY
E272 DATA
$K^+ \rightarrow e^+\pi^0\nu_e$
50 GeV
ELECTRON
CALIBRATION
$\sigma^2 = (.14\sqrt{E})^2 + (0.55)^2$
σ_E^2 (GeV^2)
POSITRON MOMENTUM (GeV/c)
b)
DETECTOR LINEARITY
E272 DATA
$K^+ \rightarrow e^+\pi^0\nu_e$
LAC ENERGY (GeV)
POSITRON MOMENTUM (GeV/c)

Figure 3.3

with χ^2 of 1.8 for 5 degrees of freedom. The first term on the right represents the contribution from sampling fluctuations, while the second term is due to such effects as pedestal fluctuations, electronic amplifier noise, shifts in amplifier gain, reconstruction difficulties, and small non-uniformities in response along the length of the strips. This resolution is consistent with that obtained in a study performed using E629 data (Chapter 5.F). The noise term was estimated to be ≈30 MeV per strip, based on an examination of single strip showers. The resolution was then adjusted to get the best agreement with the measured width of the π^0 mass peak. The resolution for a shower (assuming 10 strips on the average) was found to be

$$\sigma^2(\text{GeV}) = [\ (0.15\sqrt{E\ (\text{GeV})}\ ]^2 + (0.1)^2. \qquad (3.4)$$

The difference in the second term is probably due to the fact that in E272, the beam passed through a hole in the center of the LAC. Noise levels in strips near the beam were high compared to E629.

Figure 3.3b shows the energy registered by the LAC for positrons of various momenta. The linearity of the response was better than 5% over the momentum range 20-80 GeV/c. As a check, the E629 π^0 mass was determined for different ranges of π^0 energy. The invariant π^0 mass spectra (see Chapter 4.E) were fit with a Gaussian, using a linear term to represent background underneath the mass peak. The results are summarized in Table 3.1. The data indicate a linearity of better than 1% over the energy range 10-30 GeV. There were insufficient data outside this range to get reliable mass fits.

TABLE 3.1

π^0 Mass versus π^0 Energy

Energy Range (GeV)	π^0 Mass (MeV/c^2)
<15	135.0±0.1
15-18	134.7±0.1
18-22	134.9±0.1
22-30	135.2±0.1

The E272 kaon data were also used to determine the position resolution of the detector. Figure 3.4a is a plot of the distribution of the difference between the centroid of the energy shower in the LAC and the electron position determined by extrapolation of the track from the drift chambers. The resolution of the drift chamber system was assumed to be ±0.2 mm; the data in Fig. 3.4a indicate a position resolution in the LAC of better than 1 mm.

Figure 3.4b is a plot of the E272 π^0 mass distribution, using data from the decay $K^+ \to \pi^+ \pi^0$. The width of the mass peak is a measure of the mass resolution of the LAC. In E272, the π^0 peak had a width of 5.5 MeV/c^2 (Ref. 3.7). The E629 π^0 peak is shown in Figure 4.8a. The width measured in E629 (6.5 MeV/c^2) was quite close to the E272 value. It appears as though the LAC performed essentially as well in E629 as it had previously.

D. Lateral Shower Profile

The separation of overlapping clusters required a knowledge of the energy distribution function for an electromagnetic shower. Photons were not normally incident on the detector in general. A typical photon energy distribution was therefore asymmetric about the shower centroid. To parameterize the shower profile, the reconstruction program was run using the E272 distribution [3.7]. In E272, the LAC was much farther away from the target (~24 m) than in E629 (~8 m). Thus, photons were incident essentially normal to the

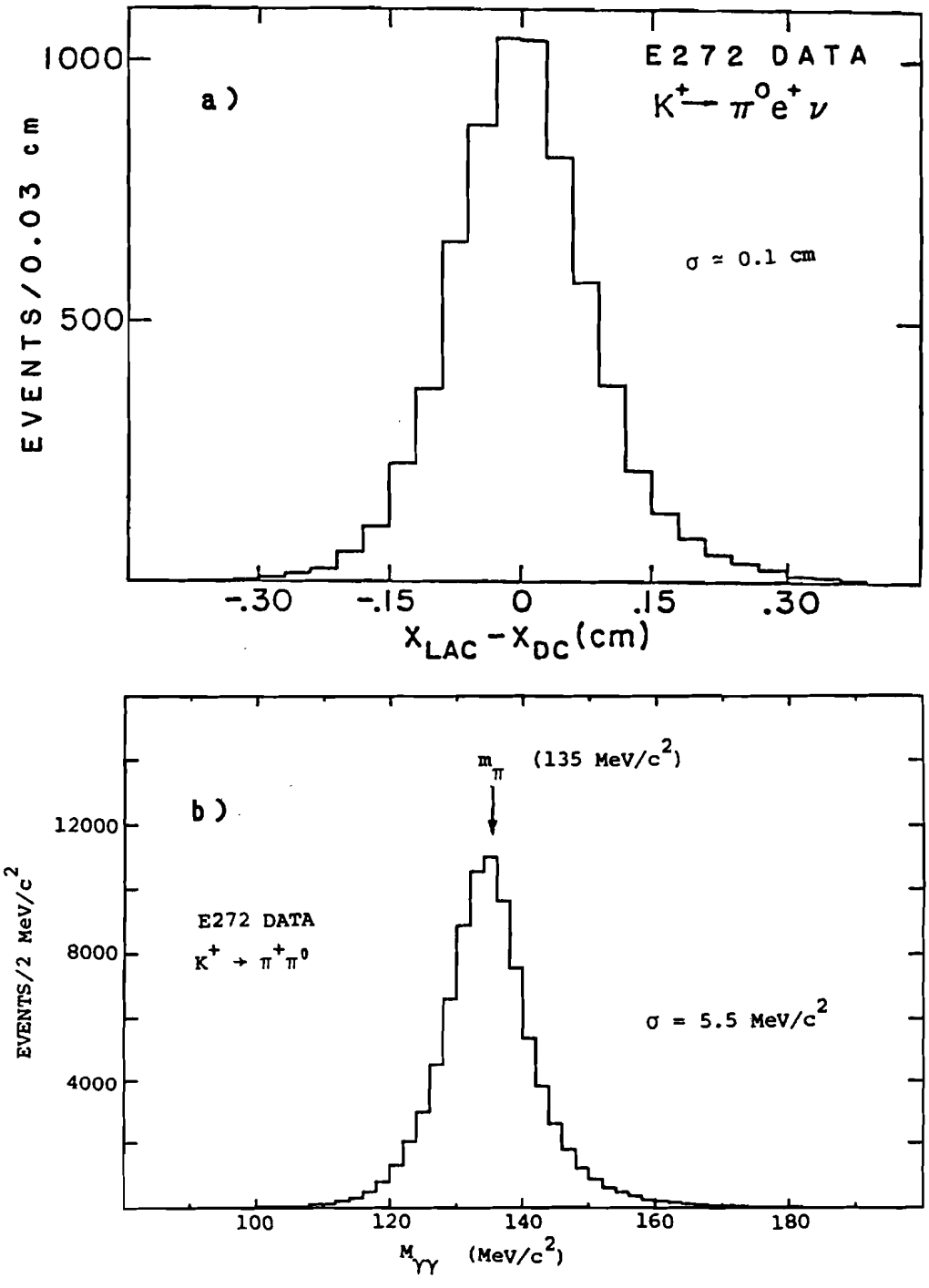
a)
E272 DATA
$K^+ \rightarrow \pi^0 e^+ \nu$
σ ≈ 0.1 cm
EVENTS/0.03 cm
1000
500
-.30
-.15
0
.15
.30
$X_{LAC} - X_{DC}$ (cm)
b)
m_π (135 MeV/c^2)
E272 DATA
$K^+ \rightarrow \pi^+ \pi^0$
σ = 5.5 MeV/c^2
EVENTS/2 MeV/c^2
12000
8000
4000
100
120
140
160
180
$M_{\gamma\gamma}$ (MeV/c^2)

Figure 3.4

detector and showers tended to be symmetric about the peak in E272.

The E629 shower shape was determined by averaging data from ~35,000 clusters. Cuts were applied to insure that each shower was synchronous with the event trigger, originated in the target, and was not of hadronic origin. Roughly 85% of the energy in an electromagnetic shower is contained within ±2 cm of the peak; non-overlapping showers were selected by requiring peaks to be separated by at least 10 cm.

Clusters were binned according to their position in the detector. The shower profile was found to be energy-independent at the 5% level; the data were therefore integrated over energy. Three ranges of X-position, corresponding to three angular ranges, were chosen for the study. The shower shape was given by

$$S_{asym}(x') = S_{sym}(x') + \theta\alpha(x'),$$

where $x' \equiv x - x_{peak}$ is the distance from the shower peak, $S_{sym}(x')$ is the shower distribution for normal incidence, and θ is the angular deviation from a normal to the LAC. The function $S_{sym}(x')$ is plotted in Figure 3.5a. The function $\alpha(x')$, which describes the shower asymmetry, is plotted in Figure 3.5b.

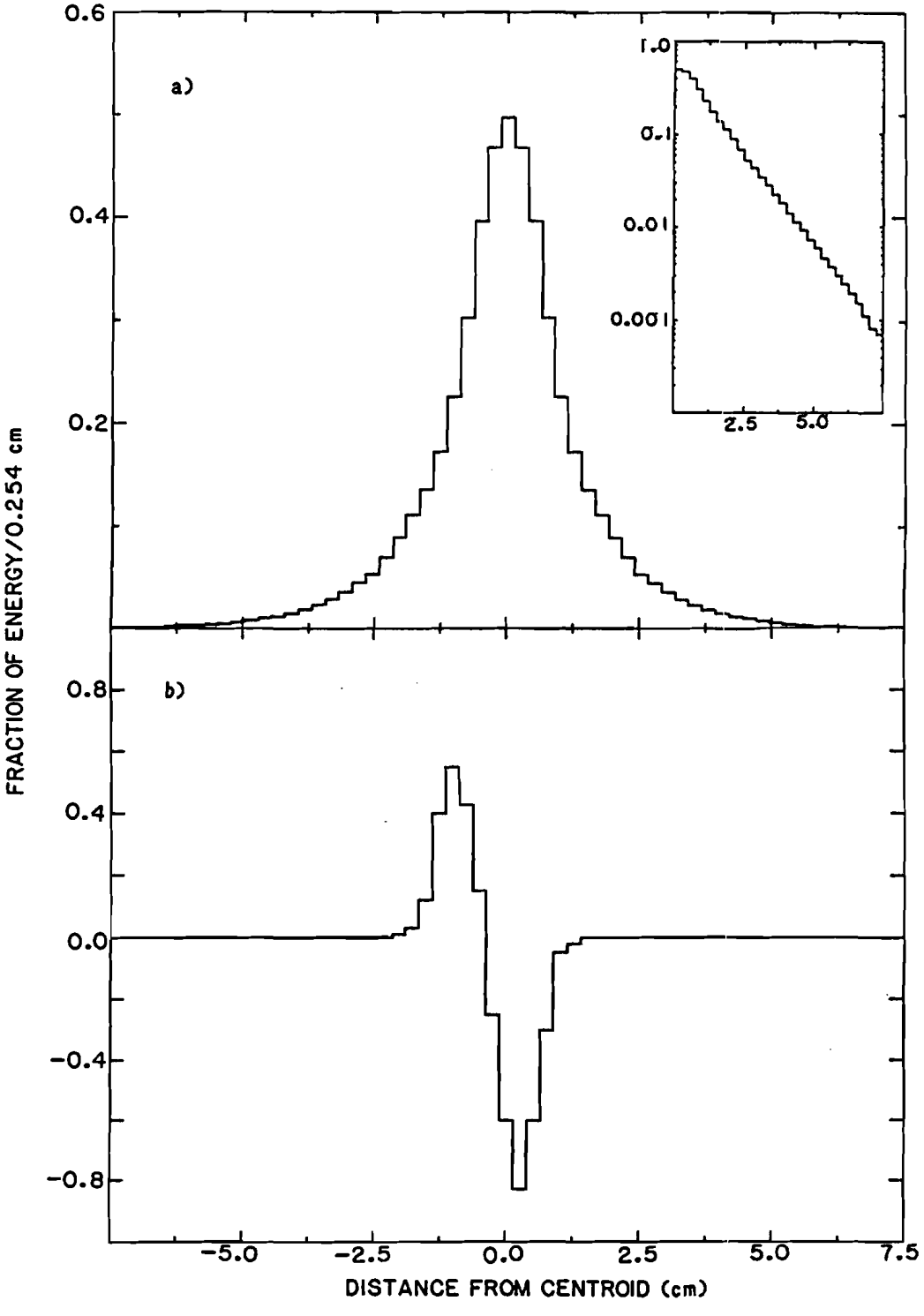
a)
b)
0.6
0.4
0.2
0.8
0.4
0.0
-0.4
-0.8
1.0
0.1
0.01
0.001
2.5
5.0
-5.0
-2.5
0.0
2.5
5.0
7.5
FRACTION OF ENERGY/0.254 cm
DISTANCE FROM CENTROID (cm)

Figure 3.5

E. Identification of Clusters in a Projection

The photon reconstruction program calculated the energies and positions of showers from the LAC strip energies. The reconstruction program was similar to the one used in E272 (i.e. see Ref. 3.7 and Ref. 3.9), with modifications to make it more effective at detecting low energy (1-2 GeV) photons. In the first stage of reconstruction, the X and Y projections of the LAC were treated independently. The program identified localized clusters of energy and calculated the energies and positions of clusters in the two views.

The reconstruction program searched the front half of the detector for groups of contiguous strips with pulse heights above a 100 MeV noise threshold. A single strip could constitute a group provided that its pulse height exceeded 175 MeV. Local maxima (peaks) and minima (valleys) were identified within each group. If more than five peaks were found within a group, or if more than eight groups were found in a particular view, the event was not processed further.

Fits of the shower shape to the data, with energies and positions of peaks as free parameters, did not converge well. In order to reduce the influence of neighboring showers, an empirical position algorithm was developed which predicted the shower centroid from the energies of the peak channel and the two immediately adjacent strips. The asymmetry in the energy of the two neighboring strips determined the shower position relative to the center of the peak strip.

Let E_p represent the energy in the peak strip of a cluster, and let E_L and E_R denote the energies of the two neighboring strips. The position, in units of strip width (1.27 cm), was determined using the following algorithm:

$$x = x_p \pm [0.40 + 0.76A \mp (0.3A^2 + 0.005)^{1/2}],$$

where $A \equiv |E_L - E_R|/E_p - 0.3$, and x_p is the center of the peak channel strip. The outer $\pm$ sign was determined from the sign of $E_L - E_R$. The inner $\mp$ sign was determined from the sign of A. The empirical constants were determined by fitting E272 electron calibration data (Ref. 3.7, Ref. 3.9) with a polynomial expression to determine the variation of x as a function of A.

Energies for isolated showers in the front half of the detector were calculated using the following algorithm:

$$E_f = \sum_i E_i + 0.4(E_L + E_R).$$

Two to seven strips were included in the summation. The exact number varied according to the characteristics of individual showers. Strips were required to satisfy the following criteria: (1) E_i had to exceed 10% of the energy recorded for the peak strip. (2) A threshold cut, $E_i > 100$ MeV, was imposed. (3) The set of strips included in the calculation did not extend past a valley. In cases where the only the peak strip satisfied these criteria, the strip with the second highest energy was included in the calculation. E_L and E_R denote the energies

of the two strips which were at the boundaries of the set that was summed over. These terms were used to apply a correction for the tails of the shower based on measurements of the lateral profile.

When showers were not isolated, but instead overlapped with other showers, a "splitting" procedure was initiated. The energy for each cluster was estimated using the algorithm described above; the energy of each strip was partitioned among overlapping peaks according to the shower shape. This procedure was iterated until the energies of all peaks in a group were stable to within 5% in successive attempts.

Energies observed in the back half of the LAC were calculated using a different algorithm. Normally, an electromagnetic shower left most of its energy in the front of the LAC and only a small amount in the back. Shower fluctuations and detector noise caused peaks in the back to be less well defined. Particles that produced showers were assumed to originate at the target. The position of the peak in the back was determined by extrapolating from the corresponding front coordinate. Three strips centered about the peak were used to calculate the back energy. Let E_p denote the energy in the peak strip of a cluster, and let E_L and E_R denote the energies of the two neighboring strips. Define

$$A \equiv (E_L - E_R)/E_p, \text{ and}$$

$$a \equiv [0.8 - 0.12A^2]^{-1}.$$

The back energies were given by: $E_B = a(E_L + E_p + E_R)$.

F. Correlation of Clusters in Different Projections

Figure 3.6 is a scatter plot of strip energies in the X and Y projections of the LAC for electrons from E272 $K^+ \to \pi^0 e^+ \nu_e$ decays (Ref. 3.7). The detector was finely segmented in the Z-direction (Figure 2.3) with alternating XY readout planes and had good energy resolution (section C). Photon energies in the two views were therefore highly correlated. Clusters in the X and Y projections were matched by comparing their energies, making allowances for the LAC energy resolution. Showers with energies less than 300 MeV were not considered. This discriminated against fake clusters produced by noise in the detector.

When correlating the two views, the program took into account the possibility that two showers overlapped and appeared as a single peak in one view, but were resolved as two distinct peaks in the other view. The program first examined isolated peaks. It then attempted to correlate the summed energy of two peaks in one view with the energy of a single peak in the other view. If a set of peaks correlated, they were immediately eliminated from further consideration to reduce the combinatorial complexity of the problem. Let E_x (E_y) denote the energy of a cluster, or set of clusters, in the X (Y) view. The quantity

$$\delta_{xy} \equiv |E_x - E_y|/\sqrt{2}\sigma_E,$$

where $\sigma_E^2 \equiv (0.15)^2(E_x + 1.0 + 0.03E_x^2)$, provided a measure of how well cluster energies in the X and Y views were correlated. The $\sqrt{2}$ factor

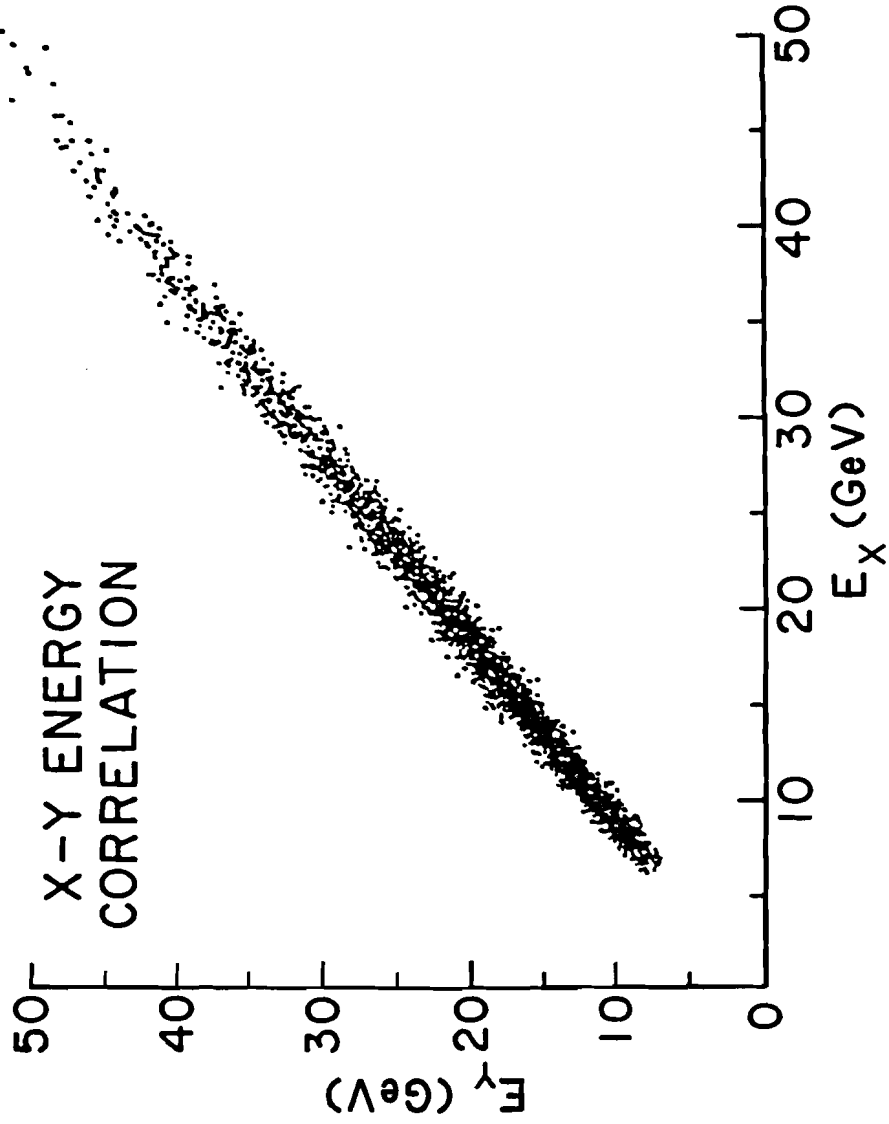

Figure 3.6

arises because $E_x \approx E_y$ and because energy fluctuations in the two views were uncorrelated. The expression $\sqrt{2}\sigma_E$ was an empirical estimate of the difference, $|E_x - E_y|$. It was essentially the energy resolution (Eq. 3.4) with a correction term (i.e. the $0.03E_x^2$ term in σ_E^2) that loosened the correlation requirement somewhat for showers with large energies. The program made a series of passes. Initially, clusters were correlated if δ_{xy} was less than a threshold value of 1.8. In subsequent passes, the threshold was progressively raised by factors of 1.25. The search continued until either all clusters were correlated, or until five iterations had been made. Back energies were also required to be in rough agreement. This latter condition suppressed accidental coincidences between photons and hadrons with similar front energies.

Shower energies were calculated by adding the energies of the component clusters in the X and Y views. The coordinates assigned to showers composed of isolated peaks were simply the front positions of the clusters in the two projections. When two clusters overlapped, their positions were determined by a fit to the peak, using energy information from the non-overlapping view, and the shower profile (Eq. 3.5). Positions in the back half, which were used in making the hadron cut described in Chapter 4.B, were determined by calculating an energy-weighted average of back strip coordinates.

Occasionally, two isolated clusters were correlated despite the possibility that a better match existed involving an overlapped cluster and two separated ones. The immediate removal of correlated

clusters from further consideration and the fixed order of searching through the possibilities (two, followed by three cluster associations) were responsible for this problem. To correct it, the program reexamined events to determine whether or not a better correlation existed.

An energy cut of 500 MeV was applied to all unmatched clusters to remove peaks that were due not to real photons, but to fluctuations in the tails of other showers. Uncorrelated clusters were paired with the other clusters in the same view. A correlation of this pair was attempted with each cluster in the other view. This new correlation was considered to be an improvement if the difference in energies between the X and Y views was smaller, even allowing for 2σ energy resolution effects (Eq. 3.4) in the original matching. All such combinations were examined. The grouping that yielded the most significant improvement was accepted, and shower positions and energies were recalculated.

Studies performed by doing visual scans of selected data events and Monte Carlo generated events indicated that this algorithm could be used to add at most one additional photon. The second unassigned cluster was not reliably handled. These studies led to the decision to limit application of the algorithm to cases in which there were no more than two unmatched peaks in either projection. This reduced the number of possible combinations the program had to deal with.

The program was set up to reconstruct a maximum of eight showers. If more hits were found, an error flag was set and analysis

of that event ceased. This was not a practical limitation in determining inclusive cross sections for single photons, π^0's, η's, etc., because there were relatively few large p_T events for large photon multiplicities. This point is discussed in more detail in Chapter 4.D.

Monte Carlo studies were performed to assess the π^0 reconstruction efficiency and the contribution to the single photon background from events that were not properly reconstructed. These studies are described in Chapter 5.E.

CHAPTER 4

Data Analysis

A. General Procedure

The positions and energies of reconstructed photons were written onto a summary tape used to carry out the analysis of the data. Also recorded were the positions and energies of uncorrelated clusters, latch data, and TDC information from the LAC. Events for which the total p_T of the photons was less than 2.0 GeV/c were eliminated.

A series of cuts were applied to events on the summary tape. Table 4.1 shows the effect that different cuts had on the data. The hadron, angle, and timing cuts (described below) were imposed primarily to suppress backgrounds to the single photon signal. These cuts were applied to all events; their effect is summarized in the

TABLE 4.1. EFFECTS OF VARIOUS CUTS

Number of Triggers	298,000
Total p_T>2 GeV/c*	211,000

Number of Events Rejected by the Cuts

Type of Cut:	All Events	Highest Energy Photon had p_T>2.1 GeV/c
Hadron	700	50
Angle	34,000	3000
Timing	19,300	2100
Angle and Timing in Coincidence	6600	1500

* In this event sample, 10% of all photons were eliminated by the fiducial area cut, and 5% by the minimum energy requirement.

column at the left in Table 4.1. However, many of the events in this category had high photon multiplicities. Most high p_T single particles (p_T>2.1 GeV/c) were found in low multiplicity events (section D). The column on the right in Table 4.1 shows the effect that the hadron, timing, and angle cuts had on the subset of events which contributed significantly to the prompt photon signal above 2.1 GeV/c.

Photons in the LAC were required to be incident within a fiducial boundary. This guarded against the possibility of shower energy escaping from the edges of the calorimeter. The centroids of reconstructed showers were required to be at least 5 cm away from the edge of the LAC. Typically, only ~1% of the energy of an electromagnetic shower is deposited more than 5 cm from the shower center.

Monte Carlo studies of the reconstruction program (Chapter 5.F) indicated that it performed reliably for photon energies as low as one GeV. A one GeV minimum energy cut was applied to all photons, to protect against reconstruction errors.

Additional cuts were applied to eliminate hadrons [4.1] produced in the target and particles originating several meters upstream of the target travelling parallel to the beam axis. The hadron cut was based on the fraction of the total energy deposited in the back portion of the LAC. Particles originating upstream of the target were cut on the basis of their time of arrival in the LAC, and their angle of incidence. Initially, these cuts were applied to all

photon candidates. Because the angle and timing information became increasingly less reliable for low energy photons, π^0 triggers were sometimes mistakenly identified as high p_T single photons. It was finally decided to apply these cuts only to the highest energy photon in the event. If this photon failed any cut, the entire event was rejected.

This procedure did not appear to bias the event sample toward single high energy photons to an appreciable degree. Above 2.1 GeV/c, the single photon p_T spectrum obtained when the hadron, timing, and angle cuts were applied to all photon candidates differed by less than 0.2% from that obtained when the cuts were imposed only on the most energetic particle in each event. This error was negligible in comparison to other systematic biases [4.2]. One reason why the effect was small is that generally, only the most energetic photon candidate in an event survived the p_T cut. The particles ranking second highest in energy contributed roughly 2% of the prompt photon signal above 2.1 GeV/c. Another reason is that in 75% of the cases in which the most energetic particle failed one of the three cuts, the second most energetic particle also failed. The particle with the most energy generally contributed the most p_T to the trigger logic. If this particle failed the timing or angle cut, the trigger was spurious, and it was likely for other particles in the event to fail as well. A more detailed description of the hadron, timing, and angle cuts is given in the next two sections.

Events which survived these cuts were examined for π^0 and η candidates. Photon pairs whose invariant mass satisfied the π^0 or η mass cuts were identified (section E). The remaining photons were included in the prompt photon sample (section F). Corrections for experimental acceptance were applied, and backgrounds to the prompt photon signal were estimated using the Monte Carlo procedures outlined in Chapter 5.

B. Hadron Rejection

Stable hadrons produced in the target were one source of background to the direct photon signal [4.3]. The design of the LAC and the distinctive properties of cascades produced by photons and hadrons helped to suppress this background. The LAC had a thickness of 25 radiation lengths, but only 1.2 pion absorption lengths. Although electromagnetic showers were effectively contained within the calorimeter, hadronic cascades were not. In general, a significant amount of an incident hadron's energy escaped detection. The hadron rejection capability of the apparatus was enhanced by the longitudinal segmentation of the LAC readout, which made it possible to independently measure the energy deposited in the front and back halves of the detector, and to impose a cut based on the longitudinal shower profile.

The response of the detector to hadrons was investigated in E272 (Ref. 3.9) using π^0's from the decay $K^+ \rightarrow \pi^+\pi^+\pi^-$. The data covered

a momentum range of ~20-180 GeV/c (Ref. 2.9). Hadrons tended to deposit little energy in the LAC. Figure 4.1a is a plot of the probability for an incident pion to deposit a fraction of its energy (E_{HAD}) in the LAC (E_{LAC}). The incident pion energy did not appear to appreciably influence the characteristics of this distribution. Approximately 20% of the pions deposited less than 5% of their total energy in the LAC, producing the spike at the left-hand side of the graph. Only a small percentage of the hadrons left a substantial portion of their energy in the detector. This fact, in conjunction with the typically rapid falloff of hadronic cross sections with p_T, helped limit the hadronic background level.

The subdivision of the readout for the front and back halves of the detector was utilized to help distinguish between electromagnetic and hadronic showers. Photons deposited ~88% of their energy in the first 12.5 radiation lengths of material. Hadrons tended to deposit a larger fraction of their energy in the back half of the LAC, as illustrated by Figure 4.1b. The cumulative distribution of the energy deposited in the back section of the calorimeter divided by the total "visible" hadronic energy (E_{LAC}) is plotted versus $(E_{BACK}/E_{LAC})_{max}$, the upper limit of integration. (The lower limit is zero.) The response of the calorimeter to electrons (solid line), which are essentially equivalent to photons in terms of shower development, and to pions (dashed and dotted lines) is shown. The curves indicate the fraction of particles that deposited less than a certain fraction of E_{LAC} in the back half of the detector. The distribution for pions did

Figure 4.1

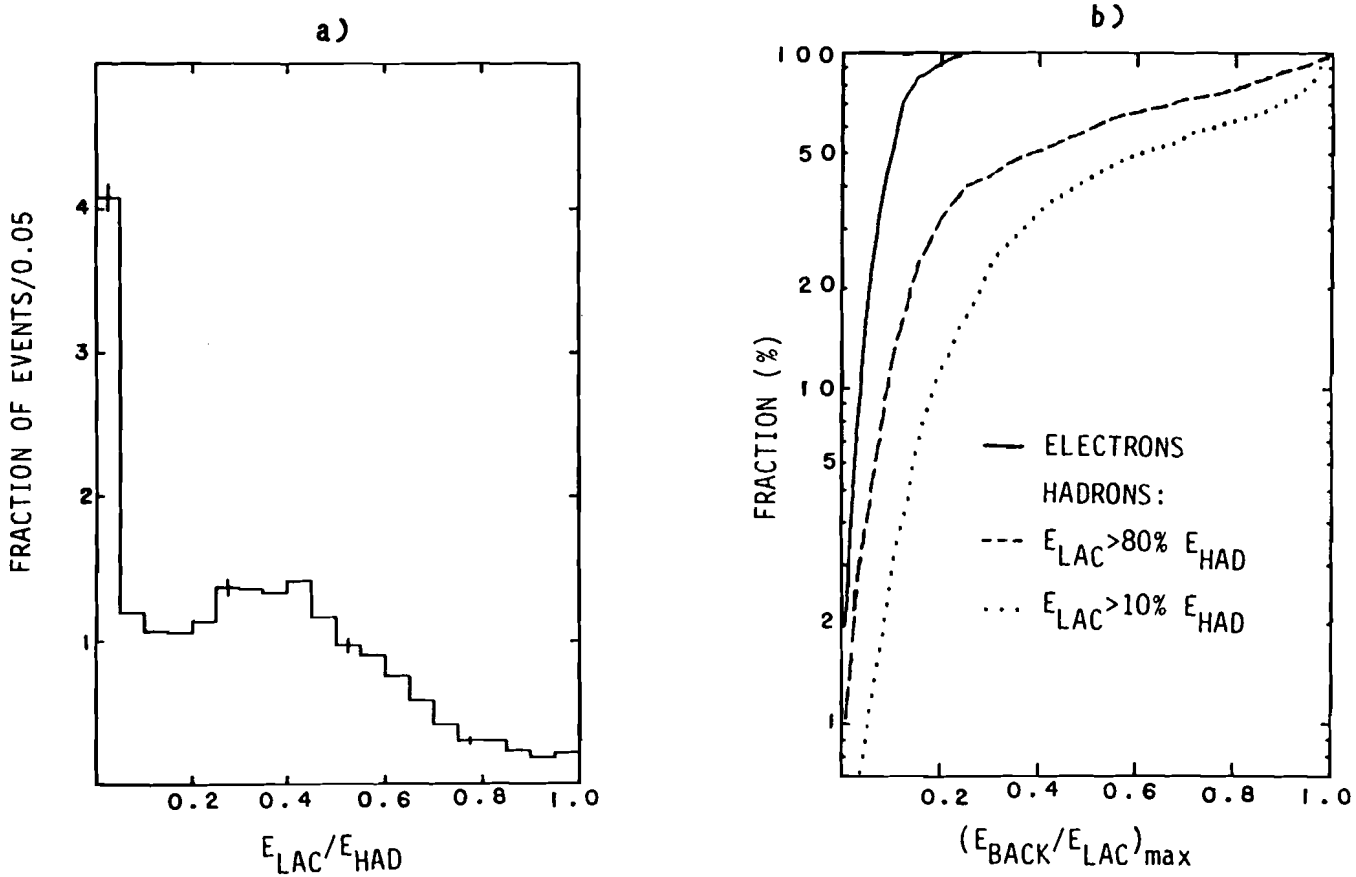
a)
FRACTION OF EVENTS/0.05
4
3
2
1
0.2
0.4
0.6
0.8
1.0
E_{LAC}/E_{HAD}
b)
FRACTION (%)
100
50
20
10
5
2
1
ELECTRONS
HADRONS:
E_{LAC}>80% E_{HAD}
E_{LAC}>10% E_{HAD}
0.2
0.4
0.6
0.8
1.0
$(E_{BACK}/E_{LAC})_{max}$

not depend strongly on the incident hadron energy, but did vary as a function of E_{LAC}/E_{HAD}. The production of secondary π^0's is one mechanism by which a hadron leaves visible energy in a calorimeter (Ref. 2.7). Generally, one would expect a cascade with $E_{LAC}/E_{HAD} \sim 1$ to have a more significant electromagnetic component. The data in Fig. 4.1b appear to support this assertion. The two curves illustrate the LAC response to "typical" hadronic cascades and to showers with a large electromagnetic component. The dotted line exhibits the behavior of the integral distribution for pions that deposited at least 10% of their energy in the calorimeter (i.e. essentially all particles which interacted in the detector). The dashed line is a similar curve for events with $E_{LAC} > 80\%\ E_{HAD}$. Although showers of this type occurred with relatively low probability (i.e. Fig. 4.1a), they constituted the bulk of the hadronic background.

To reduce hadronic contamination of the single photon signal, a cut of 0.5 was applied on E_{BACK}/E_{LAC}. The decision to apply a rather loose cut was made in order to lessen the chance of inadvertantly eliminating photons. Approximately 60% of the hadrons with $E_{LAC} > 10\%\ E_{HAD}$ had an E_{BACK}/E_{LAC} ratio greater than 0.5. For events which deposited more than 80% of their energy in the calorimeter, the corresponding fraction was ~40%. Hadrons which survived the cut did not appreciably contaminate the π^0 or η sample, because of the constraint on the two photon invariant mass. They did contribute a small background to the single photon sample, producing an apparent γ/π^0 ratio of ~0.4-1.4% over the p_T range 2-6 GeV/c (Chapter 5.E).

C. Directionality and Timing Cuts

Another source of background came from neutral or charged particles produced far upstream of the target. Most of these particles were produced at low p_T. They were moving roughly parallel to the beam axis, but offset by 1-2 meters. Because it was assumed that all particles came from the target when their p_T was calculated, their angular divergences from the beam axis were systematically overestimated. They appeared to have large p_T, and contaminated the single photon signal. Putting the veto wall and halo counters (Fig. 2.2) in the trigger (Chapter 2.F), and placing shielding in front of the LAC suppressed some of this background. Two cuts were effective in removing much of the rest: (1) the directionality cut, based on the angle of arrival of a particle at the LAC, and (2) the timing cut, based on a particle's arrival time relative to that of the trigger particle.

Figure 4.2 shows the geometry used to measure the incident angle of particles in the LAC. Due to the close proximity of the LAC to the target, the incidence angles for photons produced in the target and for particles moving parallel to the beamline differed significantly. The excellent position resolution of the LAC made possible the determination of a shower's entrance angle by comparing its position in the front and back halves of the detector.

The predicted position of a particle in the back of the detector was calculated from its front position x_F, on the assumption

Figure 4.2

$$\Delta X_B = \frac{T_{LAC}}{D_{LAC}} X_F$$

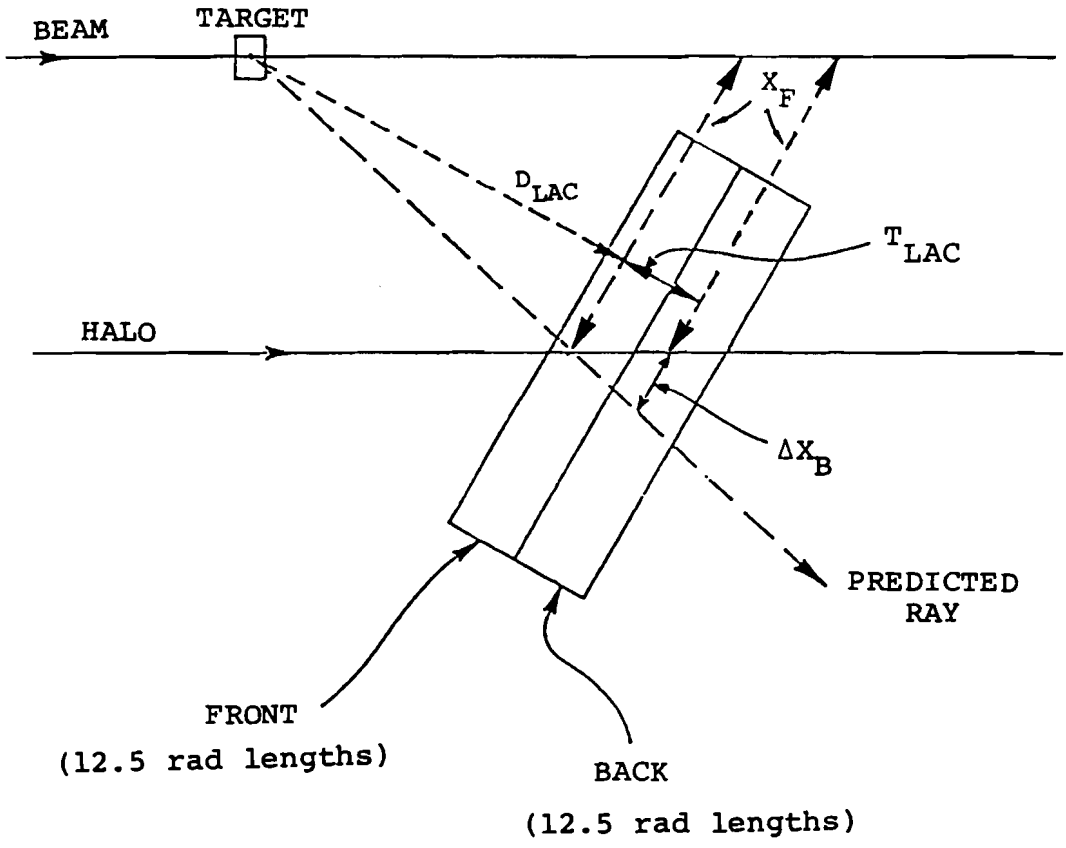

that the particle came from the target. The difference Δx_B between the predicted back position and that actually measured in the detector was evaluated. The Δx_B distribution for photons produced in the target was therefore centered around zero. Figure 4.3 is a scatter plot of Δx_B versus x_F for events in which only one shower was found in the detector. Two distinct bands are present. The one centered at $\Delta x_B=0$, independently of x_F corresponds to photons produced at the target. The tilted band is that expected for off-axis particles travelling parallel to the beam direction. The two horizontal bands at $x_F=58$ and 18 correspond to back X-strips which had broken cables inside the detector. Taking the RMS width of the central peak, and estimating the effective lever arm between the front and back halves of the LAC, the angular resolution for determining the directions of incident photons was found to be ±30 mrad (RMS).

To calculate a back position, the reconstruction algorithm required at least three strips with more than 100 MeV of energy per strip. If a photon deposited less than 300-500 MeV of energy in the back, or if a dead strip was included in the calculation, the back position was not reliably determined. The directionality cut was not applied if this was the case. Approximately 33% of the events were so affected. However, this only occurred for ~1% of the events in which the highest energy photon carried more than 2.1 GeV/c p_T.

As mentioned previously (Chapter 2.E), the amplifiers for all front X-strips were cabled to low threshold discriminators. The discriminator outputs were connected to time digitizers. This made it

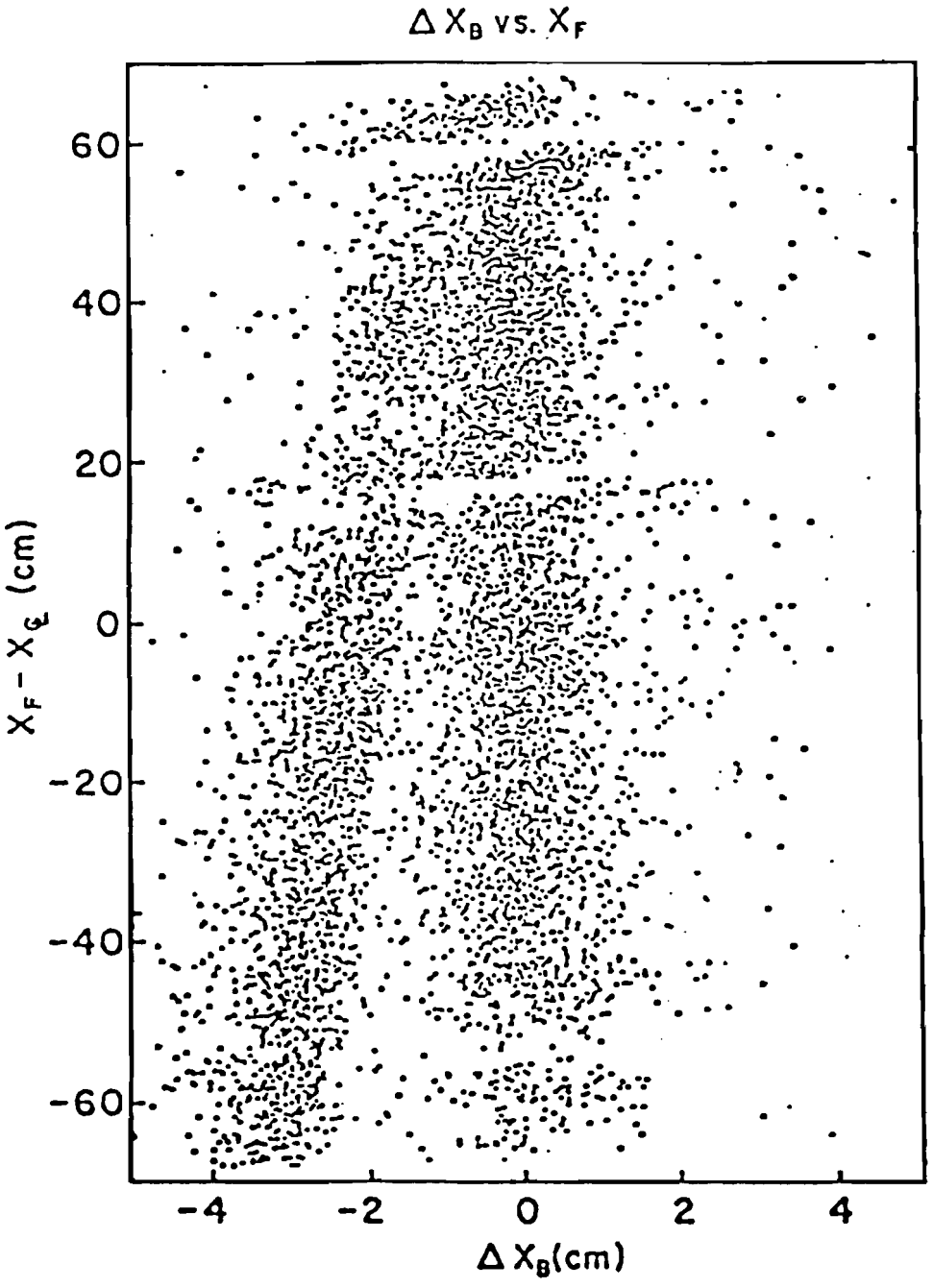

Figure 4.3

possible to measure the arrival time of energy in the detector relative to the trigger pulse. Zero baseline values for each TDC channel were determined and subtracted from the observed number of counts for that channel. An energy dependent correction term was applied to compensate for slewing of the discriminator pulses; strips with higher energies required less time to reach the threshold level. The threshold chosen for the timing discriminators corresponded to a strip energy of 500 MeV. This was the lowest threshold that could be set while remaining sufficiently far above the noise level in a particular channel. The slewing correction was reliable only for strips with more than one GeV of energy. Arrival times for photons were calculated by taking an energy-weighted average over all strips in a peak for which corrected TDC values could be determined. The timing cut was not applied to ~7% of the events, because their arrival times were not accurately calculated. However, this occurred for <0.1% of the events in which the highest energy photon carried at least 2.1 GeV/c of p_T.

Figure 4.4 shows the arrival time of energy in the detector for single photon events in three ranges of p_T. The origin is relative to the time of arrival of a photon produced in the target. The shaded distribution shows the effect of cutting on Δx_B so as to eliminate off-axis particles. In the 2-3 GeV/c p_T region, there is a clear peak at the origin with relatively little background (Fig. 4.4a). The timing resolution is inferred from the RMS width of ≈6 nsec. In the 3-4 GeV/c p_T range (Fig. 4.4b), in-time photons still dominate but

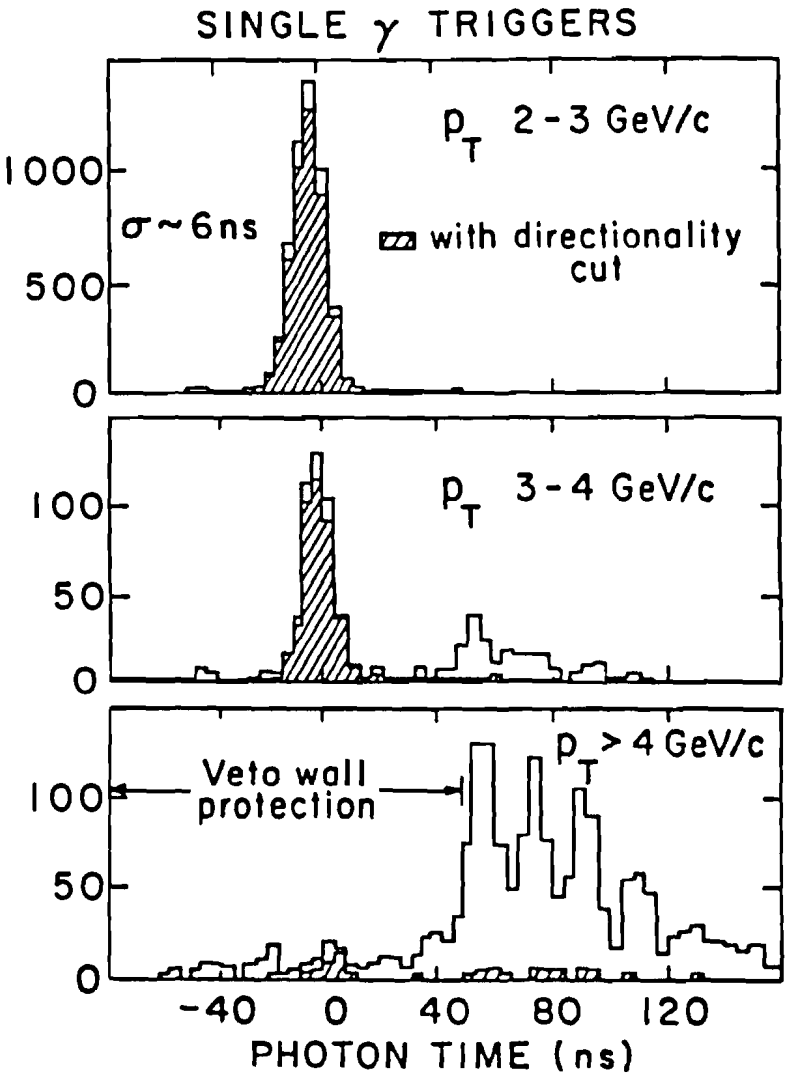
SINGLE γ TRIGGERS
p_T 2-3 GeV/c
σ~6ns
with directionality cut
1000
500
0
p_T 3-4 GeV/c
100
50
0
p_T > 4 GeV/c
Veto wall protection
100
50
0
-40
0
40
80
120
PHOTON TIME (ns)

Figure 4.4

for p_T values above 4 GeV/c the in-time peak diminishes and late arriving showers begin to dominate. The distribution in Fig. 4.4c can be understood as follows. The veto circuitry in the trigger protected against accidentals occurring within an interval 200 nsec before and 50 nsec after a beam interaction in the target. "Accidental" refers to energy deposition in the detector sufficient to satisfy the p_T threshold, but in random coincidence with a low p_T interaction in the target. The veto protection was restricted to <50 nsec past the prompt time because of the fixed delays in the LAC amplifiers. The decision to accept or reject a trigger had to occur within 250 nsec of the arrival of photons at the LAC. Because of this and because of the intrinsic delay in the formation of the veto, particles that arrived more than 50 nsec past the prompt time could not be vetoed. Before the directionality cut is applied, most of the events in Fig. 4.4c fall outside the 50 nsec protection cutoff. When off-axis photons are removed (shaded area) the resultant distribution shows a small peak of in-time photons, in addition to other small peaks corresponding to subsequent radiofrequency (RF) "bucket" times. As another indication of the timing resolution, the 19 nsec RF spill structure of the beam stands out clearly.

The timing and directionality cuts were highly correlated. Both cuts tended to reject the same events at high p_T, and were used to check one another. Some data were taken in which the target interaction requirement in the trigger was replaced by a random signal of the same frequency. It was verified that accidentals occurred at a

rate consistent with that observed for the "normal" data, and that the time and angle correlation for these accidentals was the same.

The application of directionality and timing restrictions on the showers left a clean sample of single photons originating in the target and in coincidence with a beam interaction. The effect of the hadron, angle, and timing cuts is illustrated in Figure 4.5. The upper histogram shows the p_T spectrum for events with a photon multiplicity of one and only the hadron cut applied. The lower distribution was obtained when both the angle and timing cuts were applied also. With only the hadron cut applied, the spectrum flattened out and did not fall until beyond a p_T of 10 GeV/c. With all three cuts applied, the data continued a sharp descent as expected in hadronic collisions.

D. Multiplicity Distributions

The photon multiplicity distribution in the LAC for all events which passed the cuts described in the previous sections is shown in Figure 4.6a. The average multiplicity is 3.6 photons/event. Most of these data correspond to multiphoton jets in which no individual particle carried a large p_T. This is illustrated by Figure 4.6b. The photon multiplicity distribution is plotted only for those events with a π^0 of $p_T>2.1$ GeV/c (determination of the π^0 signal is discussed in the following section). This distribution falls off rapidly with increasing multiplicity and has an average value of ~2.6.

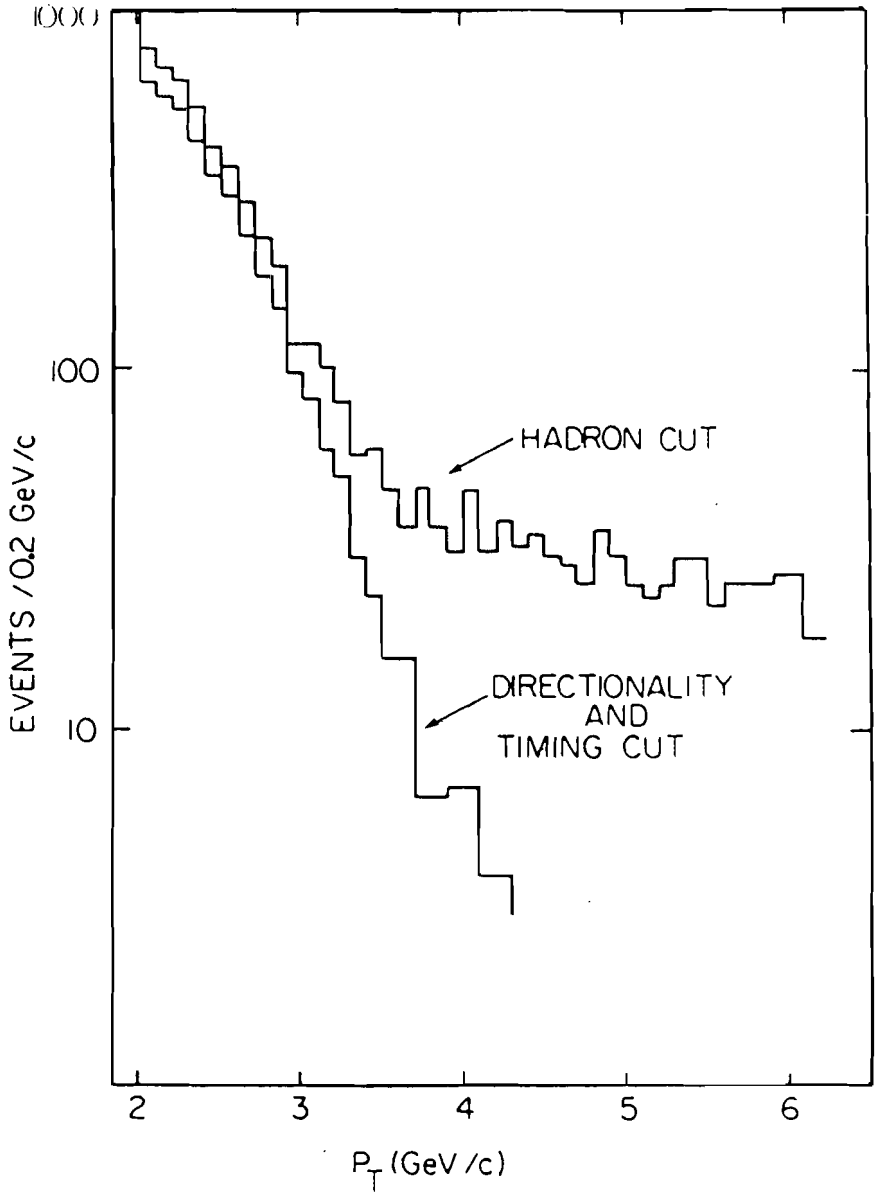
1000
100
10
EVENTS / 0.2 GeV/c
HADRON CUT
DIRECTIONALITY
AND
TIMING CUT
2
3
4
5
6
P_T (GeV/c)

Figure 4.5

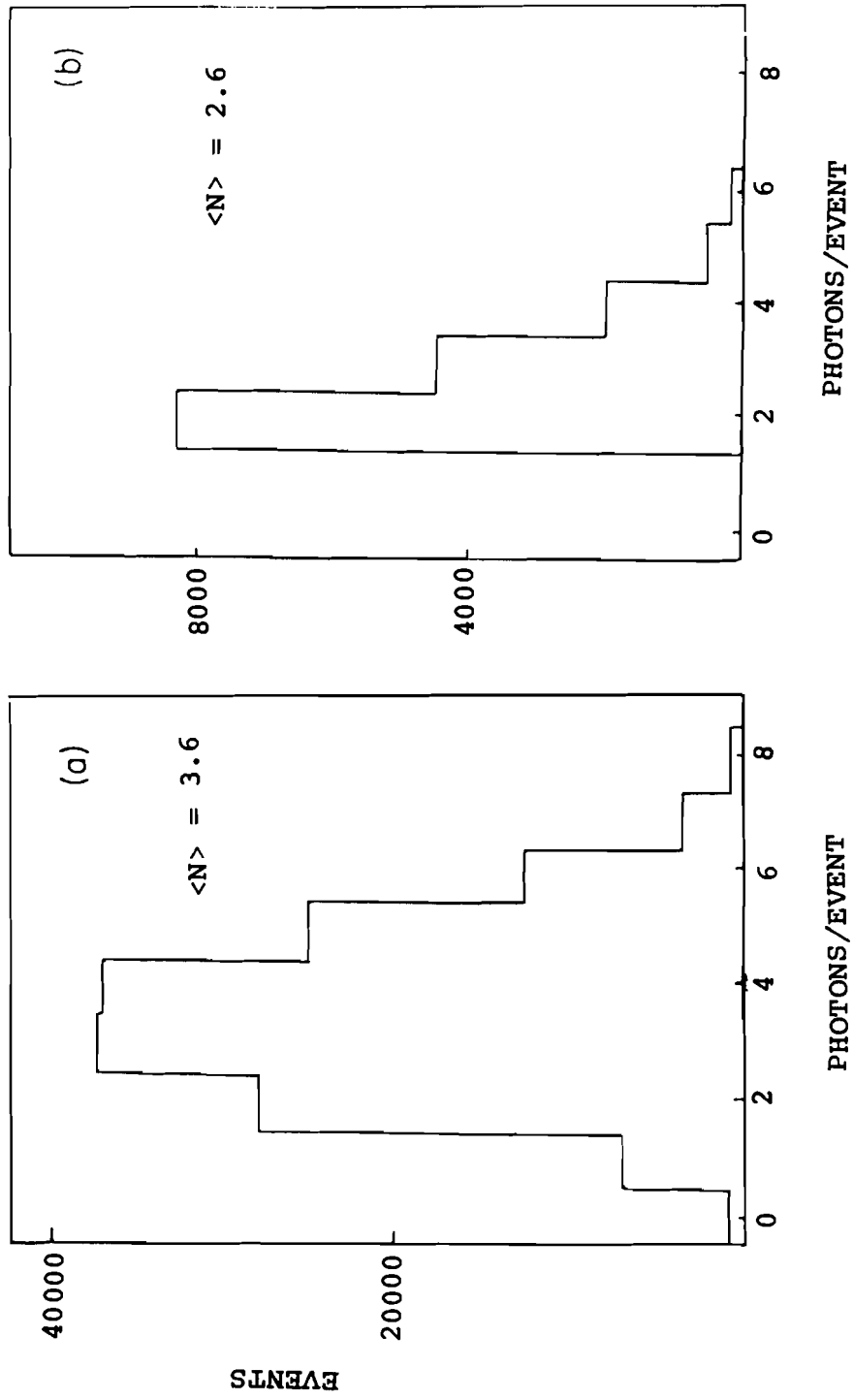
(a)
<N> = 3.6
(b)
<N> = 2.6
EVENTS
40000
20000
8000
4000
0
2
4
6
8
PHOTONS/EVENT
PHOTONS/EVENT

Figure 4.6

The experimental sample of high p_T γ's, π^0's, and η's comes predominantly from low multiplicity events. In addition, regardless of the total photon multiplicity, typically only one photon per event had a $p_T>2.1$ GeV/c, as discussed in section A. The requirement that particles carry substantial p_T significantly simplified the analysis by greatly reducing the combinatorial complexity of the high multiplicity events. Because it was relatively improbable for two accidently paired photons to simultaneously satisfy the π^0 or η mass requirement and also yield a high net p_T value, the analysis of higher multiplicity events was not plagued by unmanageably large backgrounds. The extraction of inclusive π^0 and η distributions permitted a reliable determination of the background to the inclusive high p_T direct photon distribution.

E. Neutral Mesons

In this section the procedure for defining the π^0, η, ω, and η' signals is described. The π^0, η, and η' were searched for in the $\gamma\gamma$ decay mode. Branching ratios for this mode are 98.85±0.05% for the π^0, 38.0±1.0% for the η, and 1.9±0.2% for the η'. The ω was searched for in the $\pi^0\gamma$ decay mode, which has a branching ratio of 8.8±0.5% (Ref. 2.5).

The π^0 and η signals were extracted by calculating the invariant mass of all $\gamma\gamma$ pairs. The invariant mass of $\gamma_i\gamma_j$ is given in any frame by

$$m^2 = 2E_iE_j(1 - \cos\theta_{ij}). \qquad (4.1)$$

The angle θ_{ij} is calculated using the measured separation between the photons and the distance from the LAC to the target. Because of the short lifetime for a π^0 or η ($\sim 10^{-16}$ sec), essentially all of them decay within the target.

The histograms in Figure 4.7 are invariant mass distributions for events in which $(p_T)_{ij}$ exceeded 2.1 GeV/c. Events from all multiplicity classes were included. Fig. 4.7a shows the π^0 region, and Fig. 4.7b shows the η region. As described in Chapter 3.C, the mass spectra were fit with a Gaussian, the mean of which represented the π^0 mass, plus a linear term for the background.

The π^0 mass varied linearly with its projected X-position in the LAC, as shown in Figure 4.8. The variation was symmetric about the center of the LAC. This indicates that the effect may have been caused by differences in the cable lengths connecting the strips and the amplifiers, or by differences in the effective capacitance of the LAC at the amplifier inputs. Either effect could have led to a systematic variation in amplifier gain which would not have been discerned by the calibration procedure (Chapter 3.B); when the relative gains were measured, the amplifiers were disconnected from the LAC, and the absolute normalization was determined by averaging the π^0 mass over the entire X-range. The π^0 mass in different regions of the detector was studied as a function of p_T and energy asymmetry (see Eq. 4.2) but neither possibility could clearly be established from the data. An X-dependent correction was applied to each photon

Figure 4.7

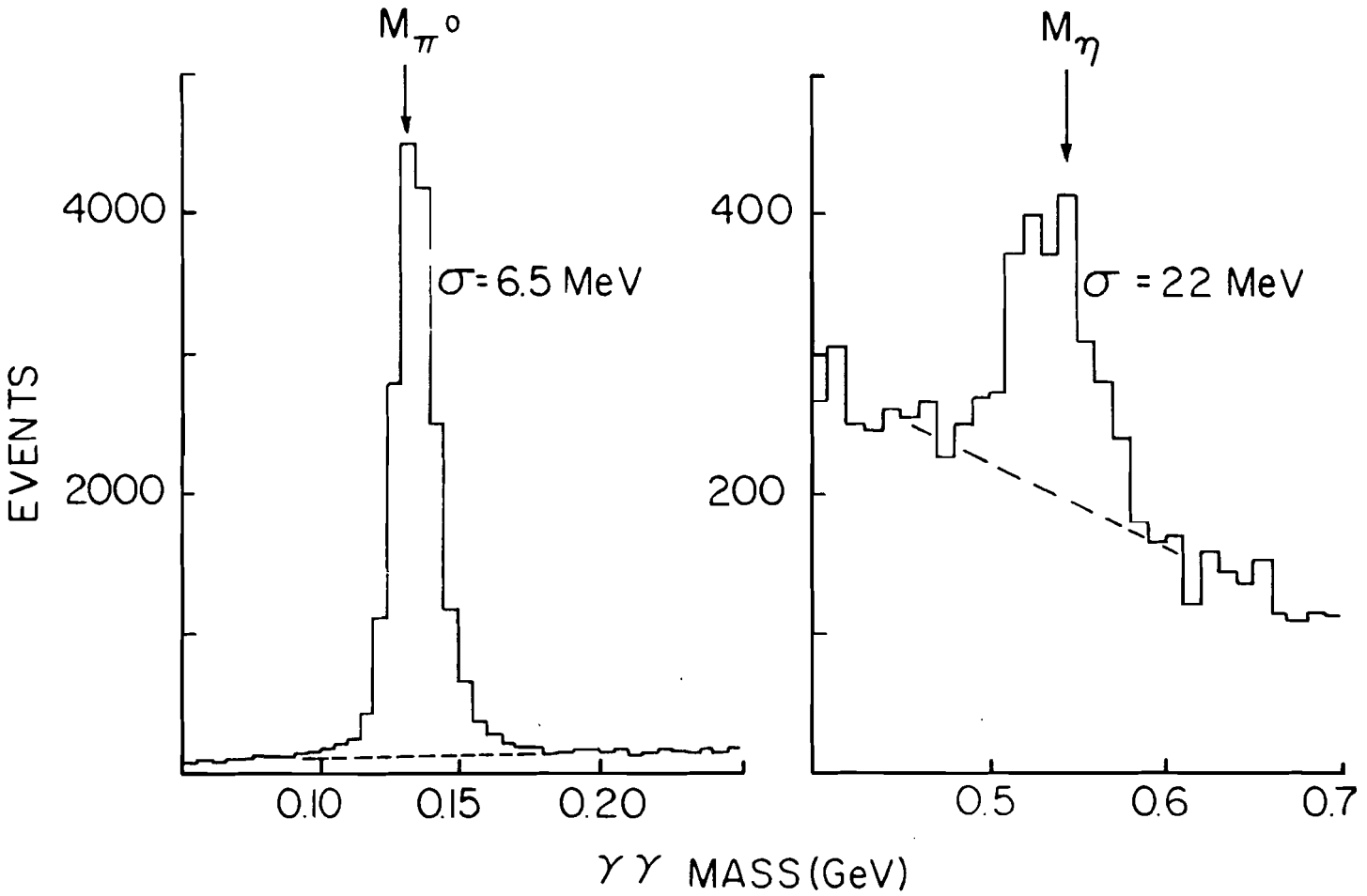
M_{π^0}
M_η
4000
2000
400
200
EVENTS
σ = 6.5 MeV
σ = 22 MeV
0.10
0.15
0.20
0.5
0.6
0.7
γγ MASS (GeV)

Figure 4.8

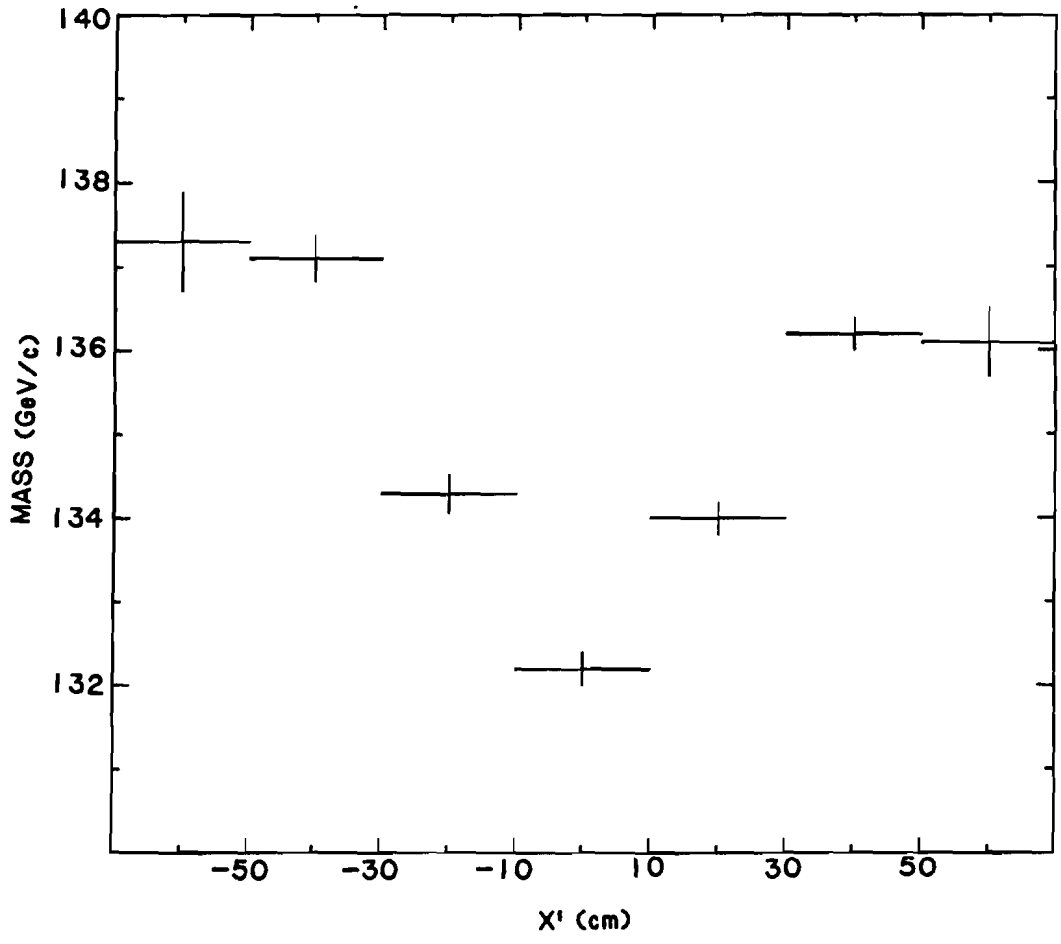

energy to compensate for the effect. Photon energies were adjusted by an overall normalization factor to bring the mean of the Gaussian to 135.0±0.1 MeV/c^2, in agreement with its accepted value of 134.9626±0.0039. The width of the peak was σ_π≈6.5 MeV/c^2. The value for the η mass was then 540.0±1.4 MeV/c^2, which differed from the accepted value of 548.8±0.6 MeV/c^2 (Ref. 2.5). The widtn of the η peak was σ_η≈22 MeV/c^2. The inability to simultaneously constrain the π^0 and η masses to better than 1% of their accepted values was taken to be indicative of a systematic uncertainty in the energy scale of ~1.5% (Chapter 6.A).

A π^0 was defined as a photon pair with a reconstructed mass that fell in the range 135±25 MeV/c^2 ($\pm 4\sigma_\pi$). A mass cut of 540±50 MeV/c^2 ($\pm 2.3\sigma_\eta$) defined η's. The e^+e^- Dalitz modes of the π^0 and η appeared identical to the γγ mode in the LAC [4.4] and were included in the respective data samples. Both signal and background were included in these mass bands. The background arose from two photons not originating from the same meson, but by coincidence having a mass within the π^0 or η mass bands.

To calculate cross sections, these backgrounds had to be subtracted. "Sidebands" were defined between 85-110 MeV/c^2 and 160-185 MeV/c^2 for the π^0, and between 250-490 MeV/c^2 and 590-750 MeV/c^2 for the η. The total width of the π^0 sidebands was equal to the width of the π^0 mass cut. To get better statistics for the η background subtraction, the total width of the η sidebands was four times greater than the width of the mass band. Events in the η

sidebands were weighted by a factor of 0.25 to compensate for the relative widths of the sideband and peak regions. The characteristics of events in the sidebands were expected to be similar to those of background events in the π^0 (η) mass intervals. Averaging the two sidebands tended to account for systematic changes in the behavior of the background over the π^0 or η mass range, at least to first order. Any quantity of interest for π^0's or η's was also evaluated for the sidebands. The sideband data were subtracted from that of the region near the corresponding peak to yield the quantity of interest for the signal alone. A small correction (4%) was applied to the number of events in the π^0 sideband to account for a tendency of the background to rise under the π^0 peak. The results were not sensitive to the widths chosen for the sidebands.

Above a p_T of 2.1 GeV/c, there were roughly 16,500 π^0 events and ~1500 events in the π^0 sidebands. There were ~1000 η's in the sample, and approximately the same number of η background events.

The degree to which the π^0, and to a lesser extent the η data is understood, determines the confidence one can place in any direct photon excess observed. For a 2γ decay, there exists a volume of phase space where one of the two photons carries off nearly the full hadron momentum, while the other has low momentum and can escape detection. Figure 4.9a depicts a $\pi^0(\eta)$ in its own rest frame decaying into two photons. In Figure 4.9b, the same decay is shown in the lab frame. A spin 0 particle decays isotropically, producing a flat distribution in $\cos\theta^*$, where θ^* is the angle a photon makes with

Figure 4.9

a) π^0 REST FRAME

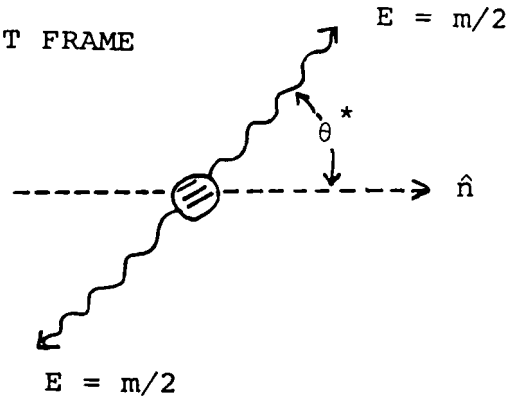

b) LABORATORY FRAME

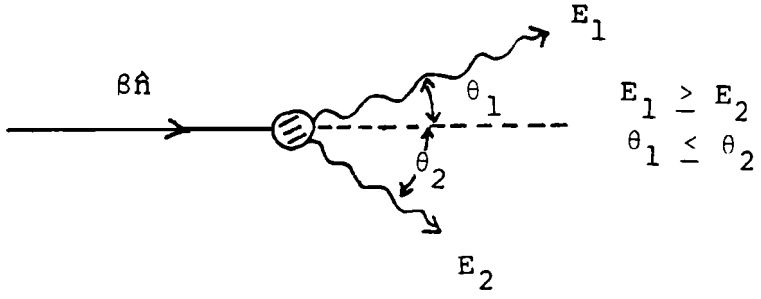

$$\text{ASYMMETRY} \equiv |\cos\theta^*| \simeq |E_1 - E_2|/(E_1 + E_2)$$

c) DECAY DISTRIBUTION

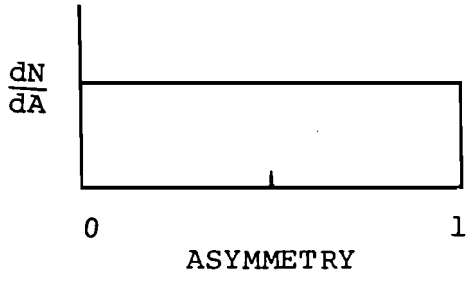

respect to the $\pi^0(\eta)$ direction. The asymmetry in the laboratory energies of the two photons is approximately equal to $|\cos\theta^*|$:

$$A \equiv \left| \frac{E_1 - E_2}{E_1 + E_2} \right| = |\beta\cos\theta^*| \approx |\cos\theta^*|. \qquad (4.2)$$

Thus, a uniform distribution of A from 0 to 1 is expected (Figure 4.9c). In practice, in events with A near unity, some of the decay photons will be lost. From Eq. 4.1 and Eq. 4.2, it follows that the minimum opening angle between two photons occurs for the case where their energies are equal, at A=0. In a highly asymmetric event, the high energy photon makes a small angle with the $\pi^0(\eta)$ direction, while the low energy photon makes a large angle. Thus at large asymmetry one photon may miss the detector completely. Another possibility is that the energy of one photon may be too low for reconstruction. This is illustrated in Figure 4.10. The reconstruction of a single photon appearing in the detector is shown in Fig. 4.10a, while Fig. 4.10b displays a highly asymmetric π^0 decay where one photon has only 5% of the total π^0 energy, and in addition, the two photons overlap in the X-view. Although the events shown were correctly reconstructed, these cases were generally difficult for the program to handle.

Figure 4.11 shows the asymmetry distribution for π^0's and η's observed in the detector. Also shown are asymmetry distributions for the two photon backgrounds near the mass peaks. In contrast to the π^0 and η distributions, the background asymmetry distributions peak at

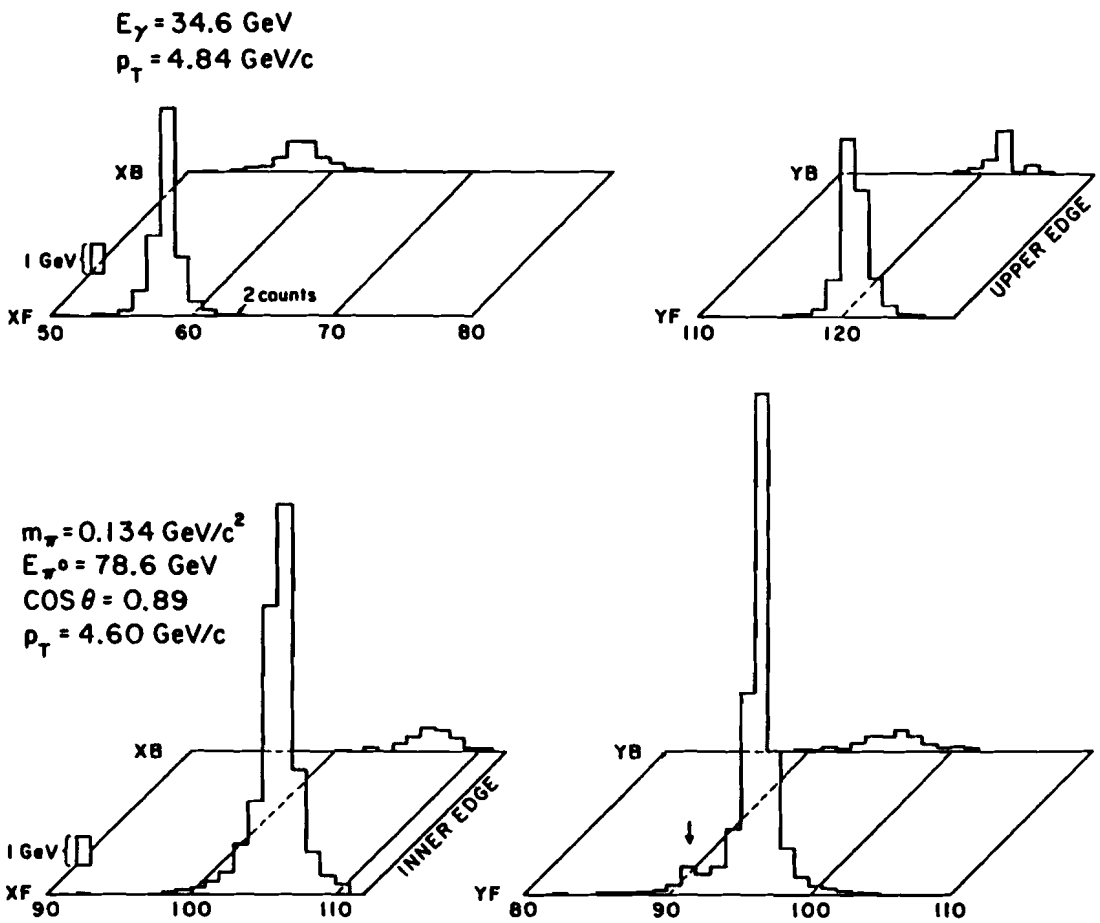
E_γ = 34.6 GeV
p_T = 4.84 GeV/c
XB
1 GeV
2 counts
XF
50
60
70
80
YB
UPPER EDGE
YF
110
120
m_{π^0} = 0.134 GeV/c^2
E_{π^0} = 78.6 GeV
COS θ = 0.89
p_T = 4.60 GeV/c
XB
1 GeV
INNER EDGE
XF
90
100
110
YB
YF
80
90
100
110

Figure 4.10

Figure 4.11

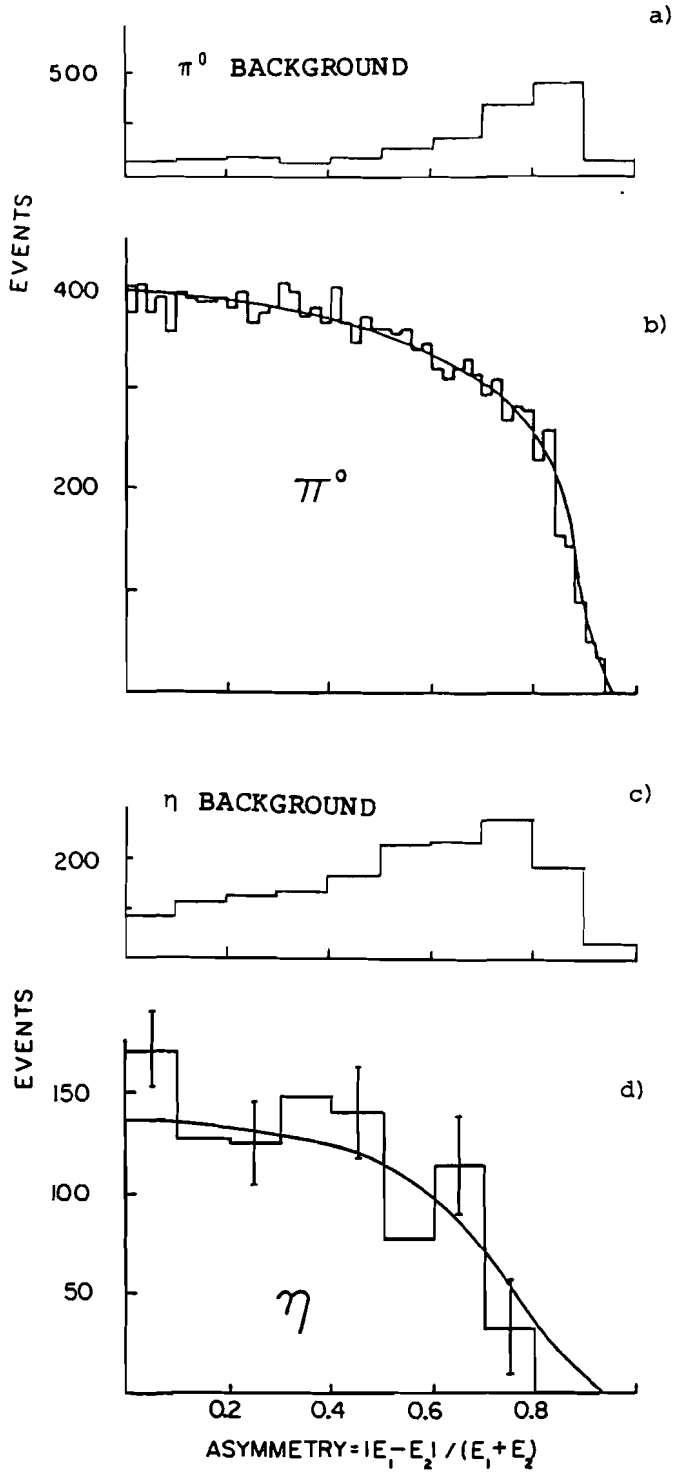
a)
500
π^0 BACKGROUND
EVENTS
400
b)
200
π^0
c)
η BACKGROUND
200
EVENTS
150
d)
100
50
η
0.2
0.4
0.6
0.8
ASYMMETRY=$|E_1-E_2|/(E_1+E_2)$

large asymmetry. The reason is that there were many low energy background photons in the LAC, some only slightly above the one GeV cut. When one of these photons, combined with a high energy photon, fell in the π^0 or η mass region, the event tended to have a large asymmetry. Applying an asymmetry cut to the data improved the signal to background ratio. Because the asymmetry distributions are flat, this cut does not introduce bias into the π^0 and η sample. An asymmetry cut of 0.8 was applied to π^0's. Because of the larger mean opening angle for the η, the asymmetry distribution falls off more rapidly. There is also a much larger background under the η peak. A somewhat tighter asymmetry cut of 0.6 was applied to the η sample. The smooth curves are Monte Carlo predictions for the background-subtracted π^0 and η signals, which clearly agree with the data. This agreement is important, because the events missing at large asymmetry are the primary background contribution to the single photon events.

The fraction of π^0 and η events lost because of the hadron, timing, and directionality cuts was estimated by applying a looser set of cuts and reanalyzing the data. The correction for these losses was ~10%. Yields were also corrected for the asymmetry cut.

Examination of the 2γ mass spectrum above the η region yielded no statistically significant sample of η' (957.57 ± 0.35 MeV/c^2) (Ref. 2.5), or of any other high mass particles decaying through this channel. The data were used to set an upper limit on the η' cross section (Chapter 6.B).

Figure 4.12 shows the three-photon invariant mass distribution for protons incident on Carbon. The peak around 780 MeV/c^2 is due to the ω meson. The accepted mass of the ω is 782.4±0.2 MeV/c^2. It decays into $\pi^0\gamma$ with a branching ratio of 8.8±0.5% (Ref. 2.5). For each event in this histogram, two of the three photons reconstructed to a π^0 mass, as defined above. The quantity $(E_\gamma - E_\pi)/(E_\gamma + E_\pi)$ was required to be greater than -0.32, and the combined p_T of the three photons had to lie in the range 2.6-3.0 GeV/c. These additional cuts reduced the background. There were roughly 30±10 ω events in this p_T range. The small number of observed events reflects both the small branching ratio and the poor acceptance of the apparatus for three-body ω decays. A Gaussian and quadratic background curve were fit to the peak. The fitted value for the ω mass was 766 MeV/c^2, and the width of the peak was ≈26 MeV/c^2.

F. Single Photons

Any photon which did not make a π^0 or η mass when paired with another photon was defined as a single photon. Those combinations that formed a π^0 or η with A>0.8 were not considered as singles. Photon pairs with an invariant mass lying in one of the background sidebands were included in the single photon sample.

There was an additional small correction to the single photon yield. When a pair of photons formed a π^0 or η mass, the algorithm did not consider them as possible single photon candidates. However,

Figure 4.12

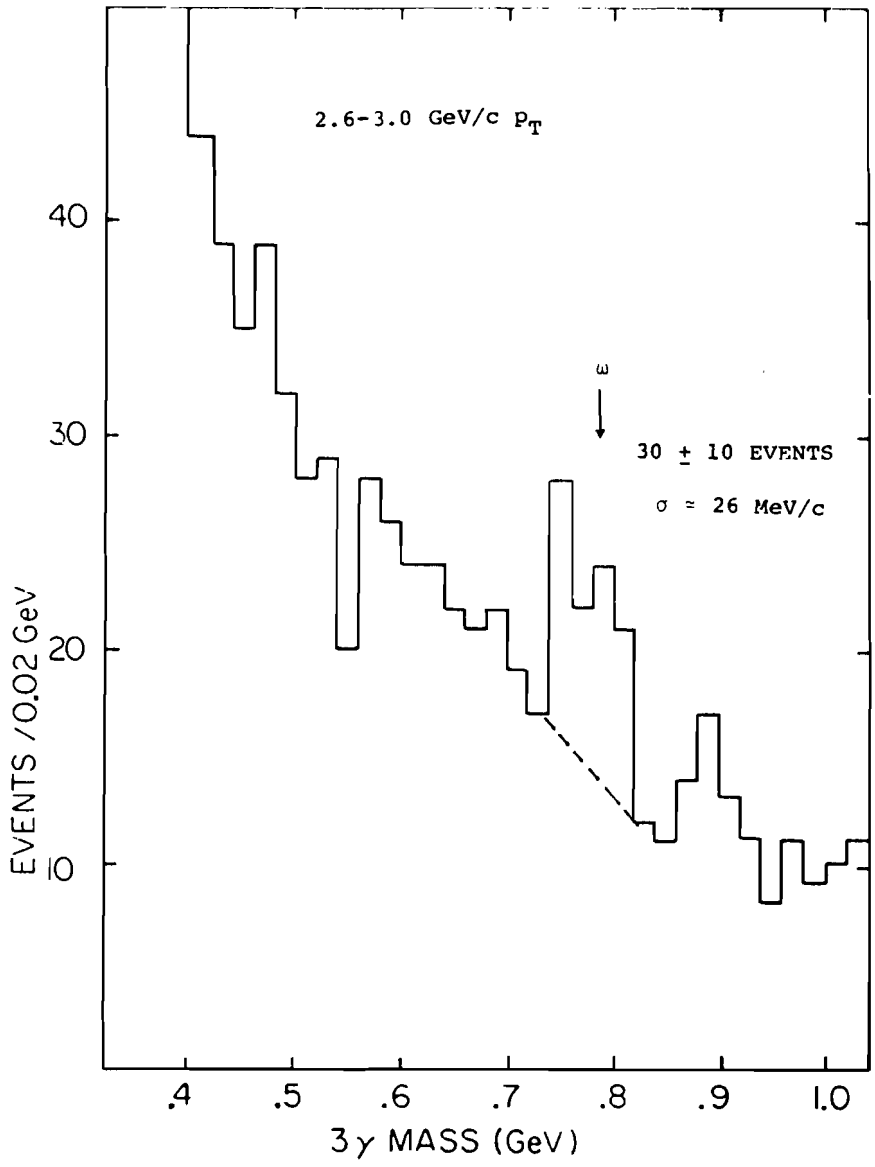
2.6-3.0 GeV/c p_T
ω
30 ± 10 EVENTS
σ ≈ 26 MeV/c
EVENTS /0.02 GeV
40
30
20
10
.4
.5
.6
.7
.8
.9
1.0
3γ MASS (GeV)

a fraction of the π^0 and η events were really due to background. Their contribution to the single photon signal was estimated to first order by doubling the single photon yield from the sidebands, after properly normalizing the sideband width to that of the signal band.

There were a total of ~5500 prompt photon candidates. Some fraction of these particles were background from $\pi^0 \to \gamma\gamma$, $\eta \to \gamma\gamma$, hadronic showers, etc. Background estimates and corrections to the π^0 and η yields for acceptance were made using the Monte Carlo procedure described in the next chapter.

G. Cross Section Normalization

The invariant cross section per nucleus can be written as

$$E\frac{d\sigma}{d^3p} = \frac{A}{\rho \ell N_o} \frac{Y_i}{F} \frac{[1 + \ell/2\lambda_{abs}]}{\Delta y \Delta\phi p_T \Delta p_T}, \qquad (4.3)$$

where A, ρ, λ_{abs}, and ℓ are the atomic weight, density, absorption length [4.5], and length of the target; N_o is Avogadro's number, Y is the acceptance-corrected yield of events, F is the incident beam flux, and $p_T \Delta p_T \Delta y \Delta\phi$ is a volume element in phase space. The factor in square brackets is a thick target correction for absorption of the incoming beam inside the target.

Signals from the trigger logic and the on-line computer (Chapter 2.F) were used to determine the incident beam flux for intervals in which the experiment was "live". The "live beam" was

defined by the following conditions: (1) The "incident beam" signal was present. (2) A "computer ready" signal indicated that electronic modules were not in the process of being digitized, read out, or cleared. (3) There was no beam-target interaction. When an interaction occurred, the system entered a "pretrigger" mode. The decision to accept or reject the event was postponed until p_T information from the LAC was available. In the interim, the beam scaler was inhibited. (4) There were no veto signals inhibiting the trigger electronics; veto protection for SCR noise and rate pile-up extended beyond the intervals defined by condition (3). The dead time introduced by the different vetos was on the order of 40%.

The various signals which defined the live beam were generated at different times relative to one another. This led to difficulties in bringing the signals into coincidence; therefore, the live beam was determined in the following manner. The "effective beam" was defined as

$$\text{EFFBEAM} = \text{BEAM} \cdot \overline{\text{PRETRIGGER}} \cdot \text{COMPUTER READY}.$$

The effective beam definition encompassed conditions 1-3. Condition 4 was then taken into account by multiplying the effective beam rate by the ratio of strobes to pretriggers. The live beam is

$$\text{LIVEBEAM} = \text{EFFBEAM} \cdot \text{STROBE/PRETRIGGER}.$$

A small correction was applied to the flux for the probability of two or more beam particles in one RF bucket being counted as one by the beam hodoscope. This yielded an increase of ~2.6% in the live beam.

Another beam related correction was made for misidentification of particles in the Cerenkov counter due to angular divergence in the beam, electronic noise in the phototubes, and shifts in the pressure of the helium used as a radiating medium. Correction factors were estimated from the pressure curve shown in Fig. 2.3 and from scaler data accumulated during the run. Prior to data-taking, the helium gas pressure was adjusted to maximize the pion detection efficiency. The flat portion of the curve was extrapolated to the pion region to estimate the background level (~2.0±0.6%) due to misidentified protons and kaons. The pressure curve indicated a pion fraction of 14±1% in the beam. Changes in the beam composition were not monitored directly -- the pressure curve measurement was only performed once during the data run. Scaler data indicated an average pion fraction of 11 ±1% over the course of the experiment. The difference between this average value and the value determined from Fig. 2.3 was attributed to the overall detection efficiency of the Cerenkov counter (~80%). The fluctuations about the average pion fraction recorded by the scalers provided an estimate for the systematic uncertainty of the detection efficiency (±10%) due to possible changes in the beam composition [4.6]. These factors were used to correct the observed number of events for contamination and counter inefficiency.

Beam studies in E272 [4.7] indicated that roughly 1% of the beam consisted of muons. The arrangement of the beamline and the beam tune were essentially the same as in E629. This value was therefore used to correct the beam flux for μ^+ contamination.

To estimate what fraction of the events were due to interactions with material in the beam other than target (air, hodoscopes, etc.), several runs were made with no target. It was found that 3-5% of the events could be attributed to such interactions. This correction was applied by rescaling the beam flux for each target by the appropriate factor after establishing that the p_T spectra for π^0's and η's were essentially the same for target-in and target-empty runs.

Table 4.2 is a summary of some relevant data for cross section normalization.

Table 4.2. Cross Section Normalization

		Be	C	Al
$\frac{A}{\rho N_o \ell}$		2.14×10^{-24}	4.74×10^{-24}	1.75×10^{-23}
Target-dependent Beam Flux Corrections†				
Empty Target		1.04	1.03	1.05
Absorption in Target:††				
Incident p_+		0.950	0.977	0.988
Incident π^+		0.966	0.983	0.991
Target-independent Beam Flux Corrections†				
Muon Background	0.99			
Two Particles/Bucket	1.026			
Losses due to Hadron, Timing, and Angle Cuts	0.91			
Pion Fraction	0.14			
$\sigma(cm^2/event)$:†††				
Incident p_+		9.43×10^{-34}	1.18×10^{-34}	2.57×10^{-33}
Incident π^+		5.69×10^{-33}	7.20×10^{-34}	1.58×10^{-32}

† Beam Flux = (Correction Factor) x (Live Beam)

†† See Ref. 4.5.

††† The cross section is obtained by multiplying this factor by the number of events (corrected for acceptance and branching ratio) and normalizing by the phase space volume that encompasses the sample.

CHAPTER 5

Monte Carlo

A. Overall Organization

Several factors affected the acceptance of the E629 apparatus. In order to extract the direct photon signal from the data and measure inclusive cross sections, it was necessary to model the geometric acceptance, the performance of the p_T trigger, the photon reconstruction efficiency, and the effects of the cuts.

The Monte Carlo procedure was a set of distinct programs. In each of these routines, the cuts that were applied to the data were also applied (whenever possible) to Monte Carlo generated events. (There were some exceptions -- for example, the hadron, timing, and angle cuts were tested in a different manner, as described in Chapter 4, Sections A-C). The geometric acceptance of the LAC and the trigger

efficiency were calculated in one program. The performance of the photon reconstruction software was evaluated separately. This division isolated the effect each factor had on the acceptance. (It was assumed that the reconstruction efficiency was only weakly correlated with the trigger and geometric efficiency.) The acceptance corrections for the π^0's, η's, and γ's (including background single photons, at this stage) were applied to the data in order to determine inclusive cross sections.

These cross sections were used as input to a third Monte Carlo routine. This program predicted the p_T distribution of background single photons from π^0 and η decays. Additional studies were performed to assess the (relatively small) single photon backgrounds produced by hadrons and by other neutral mesons (i.e. ω and η' decays). The inclusive γ/π^0 ratio and the inclusive direct photon p_T spectrum were obtained by subtracting these different backgrounds from the observed sample of acceptance-corrected single photons.

B. Geometric and Trigger Effects

The geometric acceptance for a $\pi^0(\eta)$ was a function of the position and the total p_T of the particle (i.e. via the total energy, which in turn determines the opening angle of the decay photons). The trigger acceptance depended on the X-component of the total p_T deposited in the front half of the detector, denoted by p_T^{xf}. This quantity was the sum of the p_T^{xf} deposited by the π^0 (η) and the

"associated" p_T^{xf} contributed by other particles in the event which accompanied the high p_T trigger particle. The trigger acceptance was also a function of the trigger threshold, which varied with position across the detector. The first step in the Monte Carlo involved calculating the $\pi^0(\eta)$ acceptance as a function of its X and Y coordinates (the energy-weighted average of the X and Y coordinates of the decay photons), the p_T of the particle [5.1], and the front-X component of p_T^{assoc}. For each acceptance bin, Monte Carlo $\pi^0(\eta)$ events were generated with randomly chosen decay angles. Geometric losses were evaluated by observing how often one (or two) photons missed the detector. Events having two photons contained within the fiducial geometry of the LAC were tested to see whether or not the event satisfied the p_T trigger conditions (Chapter 2.F).

Only the global p_T trigger was modeled in the Monte Carlo. The local p_T requirement did not introduce a bias for single photons, π^0's, or η's with p_T^{xf} values above the global p_T threshold. The local p_T threshold was set to ~25% of the global p_T threshold. Approximately 85% of the energy (and p_T) of a shower was deposited in three strips. Suppose that a particle had a p_T^{xf} equal to the global trigger threshold value. For a single photon, the local trigger requirement was easily satisfied. For a π^0 or η, the worst case occurred when each decay photon carried away half of the transverse momentum. In this situation, the p_T deposited in three strips corresponded to ~42% of the global p_T threshold value, still well above the local threshold level.

The global trigger condition was modeled by integrating a step function, which represented the trigger discriminator, with a Gaussian smearing term. The probability for an event to satisfy the trigger was given by

$$P(x,y,p_T^{xf}) = \int_{-\infty}^{\infty} dp_{Tx}^{smear}\ \theta[p_T^{xf} + p_{Tx}^{smear} - \tau(x,y)] \times \frac{\exp[-(p_{Tx}^{smear})^2/2\sigma^2(x,y)]}{\sqrt{2\pi}\,\sigma(x,y)}\ , \qquad (5.1)$$

The step function θ is defined as follows:

$\theta(\xi)=1$ for $\xi>0$, and

$\theta(\xi)=0$ for $\xi<0$.

The position-dependent trigger threshold [5.2] is $\tau(x,y)$, and the characteristic width of the p_{Tx}^{smear} distribution is $\sigma(x,y)$. The smearing was caused by: (1) coherent noise in the detector, (2) strip-to-strip variations in the relative gain (Fig. 3.2), and (3) variation of the threshold with position; assigning an average threshold to a finite size bin in X and Y resulted in a smearing.

The trigger threshold and the smearing term were measured using data taken with the multiple threshold triggering system described in Chapter 2.G. The trigger normally used for data acquisition had a p_T^{xf} threshold estimated to be ~2.2 GeV/c (Ref. 2.15). The low threshold trigger was set at ~1.6 GeV/c. It was assumed that the low threshold trigger was ~100% efficient for the p_T range in which the high threshold trigger turned on.

For events in which the low threshold trigger was enabled, the status of the high threshold trigger was latched. The probability for the high threshold trigger to be satisfied was given by L·H/L, where L is the number of times the low threshold trigger was satisfied, and L·H is the number of times both trigger requirements were met. A plot of this probability versus p_T^{xf} yielded the trigger efficiency $P(x,y,p_T^{xf})$, defined in Eq. 5.1.

Figure 5.1 is a plot of the trigger efficiency for π^0's and single photons. The solid line in Figure 5.1a is a fit to the π^0 data using Eq. 5.1. The same curve is superposed on the single photon data in Figure 5.1b. The threshold curve for π^0 data appears to be consistent with that obtained for triggers with only single showers.

To parameterize the position dependencies of the threshold and smearing terms, the detector was divided into nine regions. The size of each region was chosen so as to yield adequate statistics for each efficiency curve. Fits to the data in each of the nine regions determined a set of values for τ and σ. Figure 5.2a shows the nine regions and the results of the fits. The threshold τ, defined as the value of p_T^{xf} where the trigger was 50% efficient, varied from ~2.1 GeV/c in the regions farthest away from the beamline to ~2.70 GeV/c near the beamline. The values of σ ranged from ~0.3 GeV/c away from the beam to ~0.5 GeV/c near the beam.

The smearing due to averaging the effective threshold over a region is greater near the beamline, resulting in an X-dependence for σ. There were also systematic shifts in τ and σ along the Y-axis.

Figure 5.1

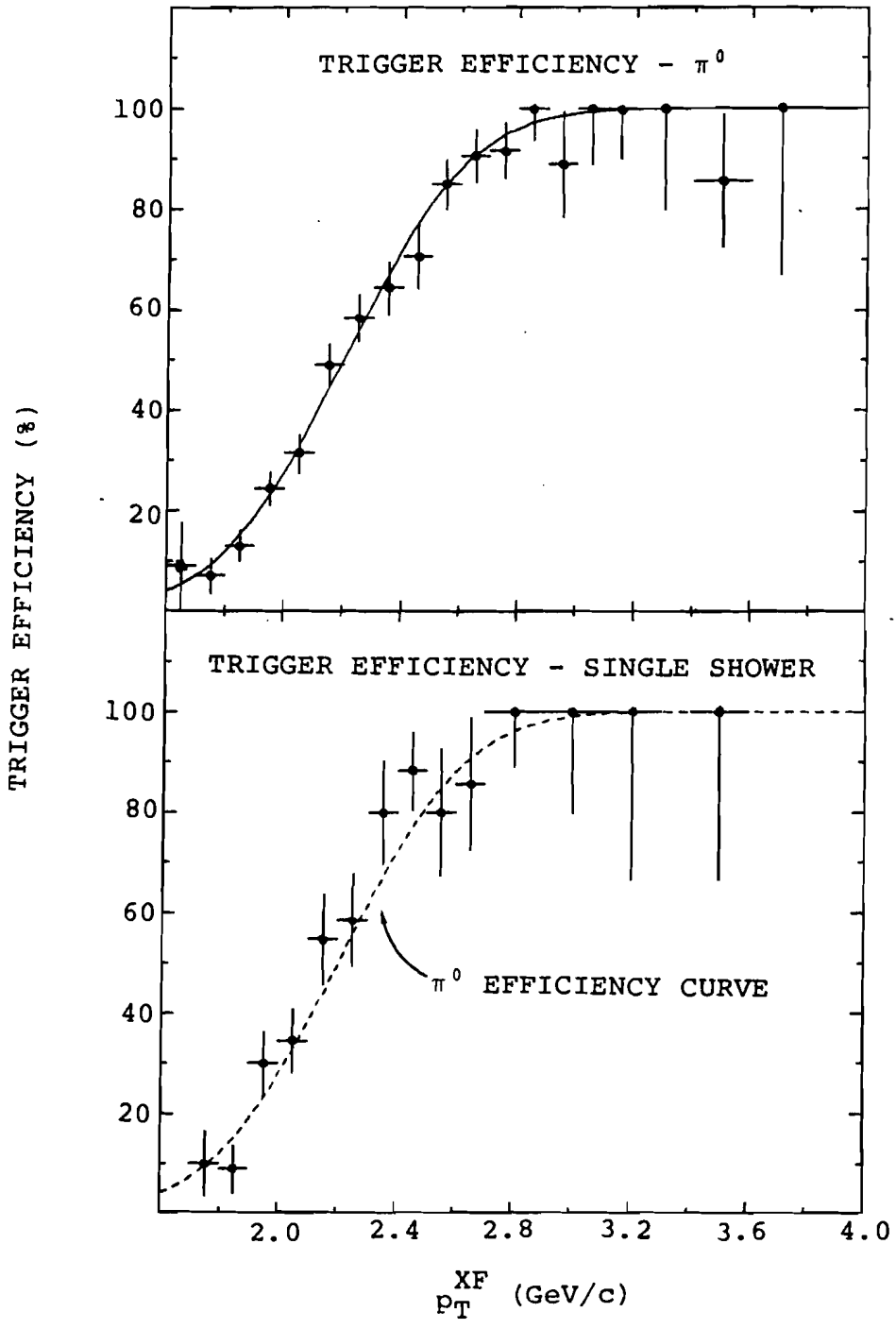
TRIGGER EFFICIENCY - π^0
TRIGGER EFFICIENCY - SINGLE SHOWER
π^0 EFFICIENCY CURVE
TRIGGER EFFICIENCY (%)
100
80
60
40
20
2.0
2.4
2.8
3.2
3.6
4.0
p_T^{XF} (GeV/c)

Figure 5.2

a)

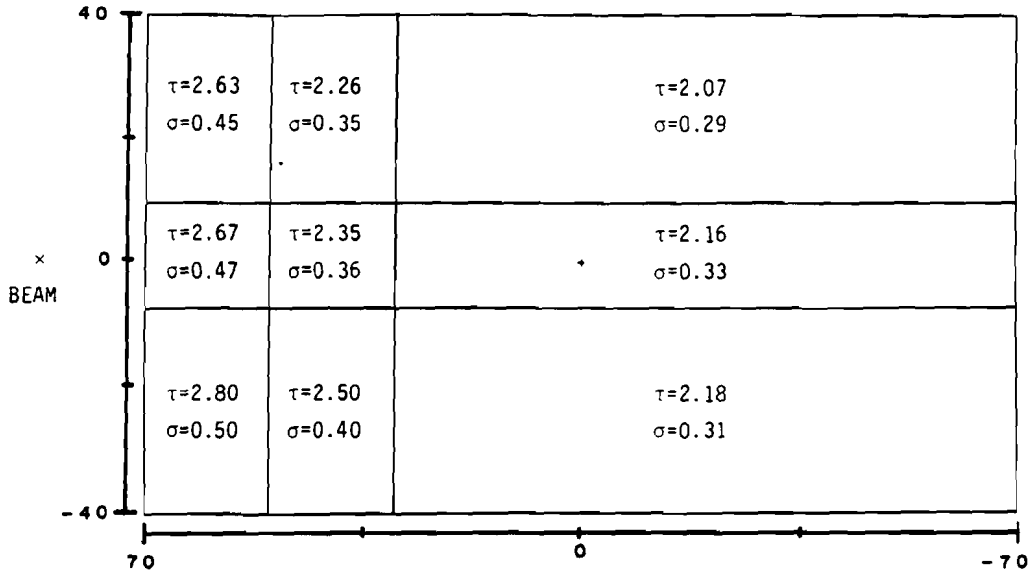
40
0
-40
BEAM
τ=2.63
σ=0.45
τ=2.26
σ=0.35
τ=2.07
σ=0.29
τ=2.67
σ=0.47
τ=2.35
σ=0.36
τ=2.16
σ=0.33
τ=2.80
σ=0.50
τ=2.50
σ=0.40
τ=2.18
σ=0.31
70
0
-70

b)

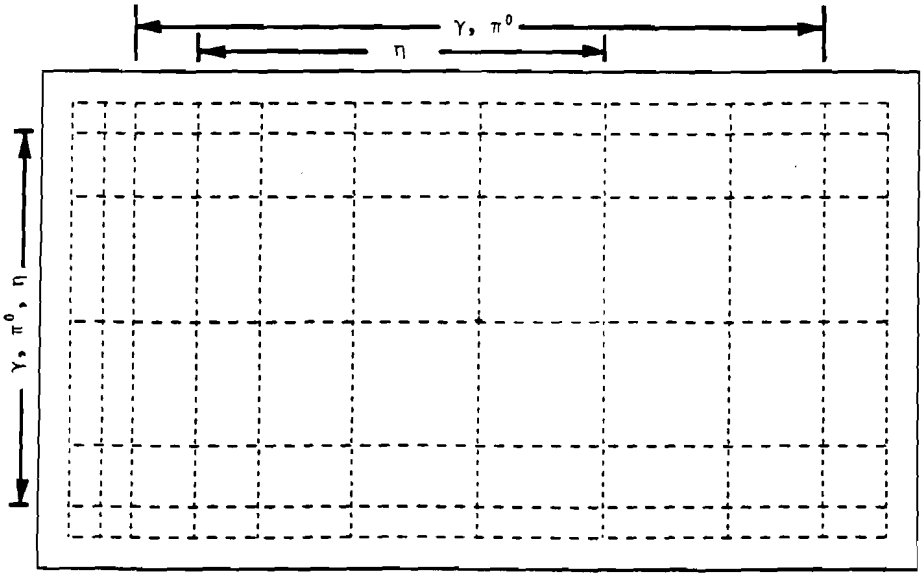
γ, π⁰
η
γ, π⁰, η

This behavior was incorporated into the trigger model. The physical cause for the variation along the Y-direction is not understood.

The p_T bins used in the acceptance calculation were 100 MeV/c wide over the range 2.0-3.0 GeV/c and 200 MeV/c wide from 3.0-4.0 GeV/c. The "associated" p_T bins were 100 MeV/c wide over the range 0.0-1.2 GeV/c. The detector was divided into 10 bins in X and 6 in Y; the bins were 5-20 cm wide in X and 10-15 cm wide in Y (Figure 5.2b). Values for X, Y, p_T, and p_T^{assoc} were randomly chosen within each bin. If both photons from a $\pi^0(\eta)$ decay were geometrically accepted, the trigger acceptance was calculated by integrating Eq. 5.1 via the Monte Carlo. Values of p_{Tx}^{smear} were chosen according to a Gaussian distribution. Values for $\tau(x,y)$ and $\sigma(x,y)$ were gotten by using the X and Y coordinates of the $\pi^0(\eta)$ [5.3] to interpolate between the fitted values for the threshold and smearing in the different regions. A linear extrapolation was used for points near the edge of the detector. If the total global p_T^{xf} exceeded the threshold, the event was accepted.

The number of events generated by the program in a particular bin was determined as follows. In bins near the edges of the detector, where the acceptance was low, 2000 events were generated. Away from the edges, an upper limit of 200 events/bin was adopted. This upper limit was not always reached; the program moved on to the next bin in the sequence after 100 events had been accepted (i.e. a sufficient number to yield a binomial error of ~7% on the weight).

The number of accepted events divided by the number of generated events yielded an acceptance for particles incident on the active area of the LAC. (An azimuth correction was applied at a later stage -- see the following paragraph.) The geometrical efficiency for π^0's hitting the active area, with decay asymmetries in the range $|\cos\theta^*|>0.8$, was typically ~90%. The worst overall efficiency (including the combined effects of the geometry and the trigger) was ~30%, near the very edges of the fiducial region.

After the $\pi^0(\eta)$ acceptances had been calculated, the data events were weighted to determine inclusive cross sections. (A correction for the fraction of azimuth spanned by the LAC was applied on an event by event basis, using the coordinates of individual particles in the data sample. A relatively small additional correction for reconstruction efficiency was also applied -- see Section E.) Fiducial and p_T cuts eliminated events with acceptance corrections that were large and varying rapidly from bin to bin. When the trigger efficiency fell below ~20%, the calculated acceptance was found to be very model dependent, particularly at low p_T. A cut on p_T was applied that varied in different rapidity intervals [5.4].

Acceptances for single photons were calculated in a similar manner; the primary difference was that the high p_T single particles were not decayed. These factors weighted every single photon data event, including the background. The π^0 and η backgrounds, as well as those contributed by hadrons, ω and η' decays, and reconstruction losses, were subtracted from this acceptance corrected signal to yield

the inclusive γ/π^0 ratio. These sources of γ background are discussed in the remainder of this chapter.

C. Single Photon Backgrounds from Particle Decays

In this section, the Monte Carlo calculation of the single photon background from π^0, η, ω, and η' decays is described. It will also be argued that other decay processes contribute negligible backgrounds.

The π^0 and η cross sections in each of the three rapidity intervals (section B) were fitted with an exponential,

$$E\frac{d\sigma}{d^3p} = A\exp(-Bp_T).$$

These parameterizations were used to distribute Monte Carlo π^0's (η's) in p_T and rapidity. Momentum four-vectors for the decay photons were generated in the meson rest frame. In this frame, the photon energies are fixed by two-body kinematics and their angular distribution is isotropic. The p_T and rapidity of a meson determined the parameters for the Lorentz transformation of the photon momentum four-vectors into the laboratory frame. If either photon failed to hit the active area of the LAC, or failed the minimum energy requirement, the other was labeled as a single photon (provided that it passed these cuts.) The ratio of the number of single photons populating a given region of phase space, $p_T\Delta p_T\Delta y\Delta\phi$, divided by the number of generated events

(multiplied by the $\gamma\gamma$ branching ratio and the η/π^0 production ratio in the case of the η), yielded the predicted background contribution to the inclusive γ/π^0 ratio from π^0 and η decay. An additional correction for the loss of π^0 photons due to reconstruction difficulties (section E) was evaluated in a separate study, and incorporated into the calculation. A correction for the loss of π^0 photons that converted into e^+e^- pairs (section F) was calculated and found to be negligible.

The ω data sample was small, and there was no statistically significant sample of η'. It was not possible to measure their cross sections as a function of p_T. It was assumed that these cross sections had the same p_T dependence as the π^0. The overall normalizations were scaled by the respective production ratios (Chapter 6.B).

For the ω, the program was modified to handle a sequential decay,

$$\begin{array}{l} \omega \rightarrow \pi^0\gamma \\ \quad\;\; \hookrightarrow \gamma\gamma. \end{array}$$

Otherwise, essentially the same procedure used for π^0's and η's was followed.

The predicted background levels from these processes are shown in Table 5.1, along with the contributions from other sources which will be explained in subsequent sections. The background ratio is shown as a function of p_T. The dependence on p_T beyond 3 GeV/c is fairly weak.

TABLE 5.1. Contributions to the γ/π^0 Background (%)

p_T (GeV/c)	π^0 decay	η decay	ω decay	η' decay	hadrons	recon-struction	total
2.15	12.7	2.2	0.2	0.3	1.3	1.5	18.2
2.25	12.3	2.2	0.2	0.3	1.3	1.4	17.7
2.35	11.1	2.0	0.2	0.3	1.4	1.3	16.3
2.45	10.3	1.9	0.2	0.2	1.0	1.2	14.8
2.55	10.5	1.9	0.1	0.2	1.0	1.1	14.8
2.70	7.8	1.4	0.1	0.2	0.9	1.0	11.4
2.90	7.8	1.2	0.1	0.2	0.9	0.9	11.1
3.25	6.7	1.3	0.07	0.13	0.6	0.8	9.6
3.75	5.6	1.1	0.05	0.1	0.6	0.6	8.1
4.50	4.5	0.3	0.04	0.06	0.5	0.5	5.9
5.50	3.4	0.3	0.03	0.02	0.4	1.0	5.2

Contributions from other particle decays, or other decay modes, were negligible, either because of small branching ratios, or for kinematic reasons [5.5]. For example, consider the decay $A \rightarrow B+\gamma$ (similar arguments can be applied to processes involving three or more secondary particles). Assume particle B is not detected, so that all of the photons contribute to the background if they are accepted by the LAC. A rough estimate of the expected background level may be obtained as follows [5.6].

In the rest frame of the primary particle A (Figure 5.3a) the photon energy (ε^*) and momentum ($\vec{q}^*$) are determined by simple two-body kinematics:

$$\varepsilon^* = \frac{(m_A^2 - m_B^2)}{2m_A} \tag{5.2a}$$

$$q_z^* = \varepsilon^* \cos\theta^* \tag{5.2b}$$

$$q_x^* = \varepsilon^* \sin\theta^* \cos\phi^* \tag{5.2c}$$

$$q_y^* = \varepsilon^* \sin\theta^* \sin\phi^*, \tag{5.2d}$$

where θ^* is the polar angle measured with respect to the Z^*-axis, ϕ^* is the azimuthal angle measured with respect to the X^*-axis, and the m's are the rest masses of particles A and B. In the laboratory frame (Figure 5.3b), particle A has energy E_A and momentum $\vec{p}_A$. The photon momentum in the laboratory frame, $\vec{q}$, may be calculated by performing the appropriate Lorentz transformation:

$$\vec{q} = \vec{q}^* + \gamma_A \vec{\beta}_A \left[\frac{\gamma_A \vec{\beta}_A \cdot \vec{q}^*}{(1 + \gamma_A)} + \varepsilon^*\right], \tag{5.3}$$

Figure 5.3

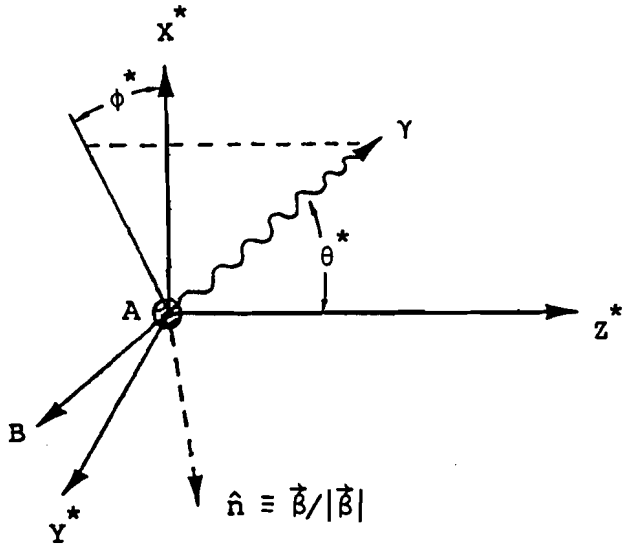

a) PARTICLE A REST FRAME

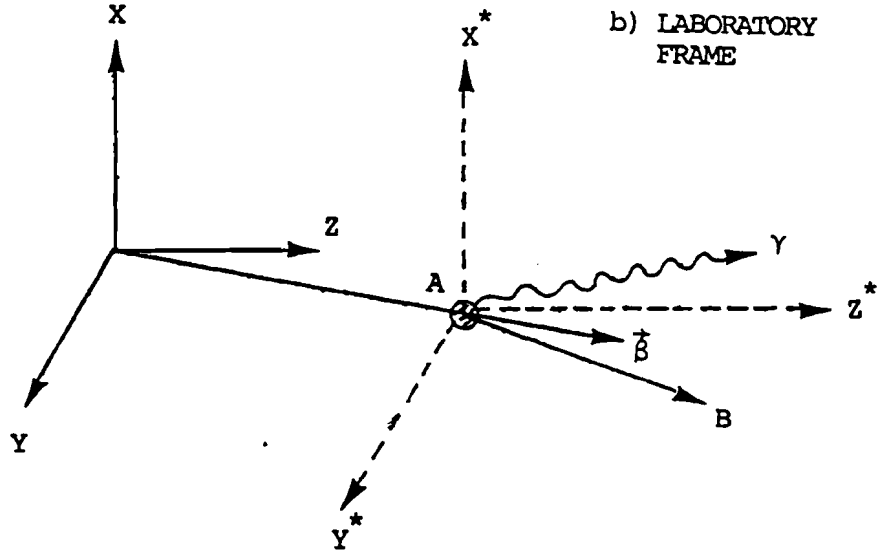

b) LABORATORY FRAME

where $\vec{\beta}_A \equiv \vec{p}_A/E_A$, and $\gamma_A \equiv E_A/m_A$. For $E_A >> m_A$, $\gamma_A >> 1$ and $|\vec{\beta}_A| \sim 1$. If the transverse momentum component of particle A (p_{TA}) is small compared to the longitudinal component, then $\beta_{Ax} << \beta_{Az}$. For large E_A: (1) either the opening angle between B and γ is small (i.e. the photon is roughly collinear with A), or (2) the photon will not be collinear, but will have low energy in the lab frame (i.e. see the discussion of π^0 decay in Chapter 4.E). Thus, the first term on the right side of Eq. 5.3 is small compared to the second. Making these approximations,

$$q_T \approx \frac{p_{TA} c^* (1 + \cos\theta^*)}{m_A}. \tag{5.4}$$

The spectrum of the decay photons, $d\sigma/dq_T$, is obtained by integrating the product of the primary particle's p_T spectrum ($d\sigma/dp_{TA}$) and the angular distribution function over all p_{TA} and θ^*, while requiring that Eq. 5.4 hold. If particle A is spin 0, or if it is produced with no polarization, the decay is isotropic in the rest frame of A. Defining $\xi \equiv \cos\theta^*$, the angular distribution is $g(\xi)d\xi = 1/2\, d\xi$. The p_T spectrum of the photon is given by

$$\frac{d\sigma(\gamma)}{dq_T} = f \int_0^\infty dp_{TA} \frac{d\sigma(A)}{dp_{TA}} \times \int_{-1}^{1} \frac{1}{2} d\xi\, \delta\left[q_T - \frac{p_{TA} c^* (1+\xi)}{m_A}\right], \tag{5.5}$$

where f is the branching ratio for the $A \to B + \gamma$ decay mode. The only

contributions to $d\sigma/dq_T$ are for values of ξ and p_{TA} such that the argument of the delta function is zero. Performing the integral over ξ, one finds that only primary particles for which

$$p_{TA} > p_T' \equiv \frac{q_T}{(1 - m_B^2/m_A^2)}$$

contribute. Eq. 5.5 reduces to

$$\frac{d\sigma(\gamma)}{dq_T} = \left[\frac{f}{(1 - m_B^2/m_A^2)}\right] \int_{p_T'}^{\infty} dp_{TA} \frac{1}{p_{TA}} \frac{d\sigma(A)}{dp_{TA}} . \qquad (5.6)$$

This expression is easy to evaluate analytically if the inclusive cross section for particle A is approximated by a power law of the form $\sigma_A p_{TA}^{-n}$, where σ_A is an appropriate normalization factor. This implies that $d\sigma_A/dp_{TA} = \sigma_A p_{TA}^{-n+1}$. The ratio R_A of the photon cross section to that of particle A, both evaluated at the same p_T, is

$$R_A = \frac{f(1 - m_B^2/m_A^2)^{n-2}}{n - 1}. \qquad (5.7)$$

Table 5.2 shows the background levels expected from various processes, assuming a p_T^{-8} dependence for the inclusive cross section. Because the γ/π^0 ratio is the quantity being measured experimentally, the values of R_A have been multiplied by the production ratios σ_A/σ_{π^0}. The various isospin states which contribute to γ/π^0 have been summed over (i.e. "ρ" represents the total contribution of the ρ^+, ρ^0, and

Table 5.2. Additional γ/π^0 Backgrounds

Process $A \to B + \gamma$	σ_A/σ_{π^0} †	f †	γ/π^0
$\eta' \to \rho + \gamma$	1.0	0.30	$\sim 10^{-4}$
$\rho \to \pi + \gamma$	1.0	0.0002	$\sim 10^{-4}$
$K^* \to K + \gamma$	0.3	0.002	$\sim 10^{-5}$
$\phi \to \eta + \gamma$	0.06	0.02	$\sim 10^{-5}$
$\Delta \to p + \gamma$	1.6	0.01	$\sim 10^{-5}$
$\sum \to \Lambda + \gamma$	0.3	1.0	$\sim 10^{-7}$

† See Ref. 5.7.

ρ^-). The largest of these contributions is of order 0.01%, roughly an order of magnitude smaller than the η' or ω background level. The sensitivity of these estimates to the approximations made in deriving Eq. 5.7 was ascertained by using the Monte Carlo program to perform a more accurate calculation for $\eta' \to \rho\gamma$, $\rho \to \pi\gamma$, and $K^* \to K\gamma$. The Monte Carlo predictions did not exceed the values listed in the table. The kinematic suppression is greater for three-body decays. Thus, the only significant backgrounds from meson decays were due to π^0, η, ω, and η'. All other processes were negligible.

D. Hadronic Backgrounds

Not all of the high p_T hadrons produced in the target were eliminated by the hadron cut described in Chapter 4.B. A fraction of them deposited a large part of their energy in the LAC, and passed the cut on the back/total energy ratio. These events were a source of background to the single photon spectrum. The magnitude of this effect was calculated by evaluating the following expression:

$$\frac{d\sigma(h\to\gamma)}{dp_T} = \sum_h \int_{p_T}^{\infty} dp_T' \frac{d\sigma(h)}{dp_T'} \quad F_h(p_T', p_T). \tag{5.8}$$

The summation is performed over the different hadron species, with cross sections $d\sigma(h)/dp_T'$. The function $F_h(p_T', p_T)$ is the probability for a hadron produced at transverse momentum p_T' to fake a

single photon at transverse momentum p_T. The integral ranges over all values of p_T'. However, since $F_h(p_T', p_T) = 0$ for $p_T' < p_T$, the lower limit was set to p_T [5.8].

Inclusive cross sections for the various hadrons were estimated by scaling the E629 π^0 cross section according to production ratios measured in other experiments [5.9]. It was assumed that these particles had the same p_T dependence as the π^0. The sum of the π^+ and π^- cross sections is roughly twice that of the π^0. The production ratios for the K^+, K^-, p, and $\bar{p}$ relative to the π^0 are ~0.5, 0.2, 0.8, and 0.06 respectively. The K_L^0 cross section was estimated by averaging the charged kaon results. The p and $\bar{p}$ ratios were used as estimates for the n and $\bar{n}$ contributions.

In order to ascertain the background contributed by a hadron of a given p_T', it was necessary to determine the amount of hadronic energy detected by the LAC, the back/total energy distribution of the "visible" energy, and the performance of the reconstruction program in dealing with hadronic events. The dependence of $F_h(p_T', p_T)$ on each of these effects is described in the subsequent paragraphs.

The probability distribution for the fraction of the total hadronic energy deposited in the LAC by an incident pion was measured in E272 (Fig. 4.1a). Distributions for other hadrons were obtained by normalizing the pion curve using weights derived on the basis of considerations regarding hadronic shower development. Because hadronic cross sections decrease rapidly with increasing transverse momentum, the particles which make the principal contribution to the

integral in Eq. 5.8 have $p_T' \approx p_T$. A hadronic shower is created by a series of inelastic hadronic interactions in which secondary particles are produced. If most of the incident energy is transferred to neutral pions in the first interaction (recall that the LAC is roughly one pion interaction length thick -- Chapter 2.A), then the shower closely resembles an electromagnetic cascade, and consequently, a substantial portion of the total energy is observable in the calorimeter. Thus, the processes of interest for the derivation of the weighting factors are those involving the inclusive production of π^0's at large x_F; interactions in which a single particle acquires most of the available energy in a collision occur predominantly in this kinematic region [5.10]. Inclusive cross sections for πp, Kp, and pp collisions at energies of 10-20 GeV and 100 GeV [5.11] (corresponding roughly to the energies of hadrons incident on the LAC) were compared in the x_F range of ~0.8-1.0. Kaons were assigned a weight of ~0.5. Protons and neutrons were weighted by ~0.1 [5.12]. The overall $\bar{p}$ and $\bar{n}$ contributions were small due to their low production ratios. Therefore, no weighting was performed for these particles.

The longitudinal development of a hadronic shower differs from that of an electromagnetic cascade. On the average, the back/total energy ratio for hadrons tended to be larger than for photons (Fig. 4.1b). The p_T trigger was sensitive only to energy deposited in the front half of the LAC, and was therefore less efficient for hadronic showers than for electromagnetic showers of the same energy. The

relative hadron/photon trigger efficiency was evaluated as a function of p_T and incorporated into the definition of $F_h(p_T', p_T)$. This efficiency factor also took into account the back/total energy cut (Chapter 4.B) applied to the data.

The parameters in the reconstruction algorithms were specifically "tuned" to locate and correlate electromagnetic clusters. They did not necessarily have optimal values for hadronic shower identification. The procedure for determining the photon reconstruction efficiency is described in the following section; the hadronic reconstruction study was conducted in a similar manner, using the hadron shower shape measured in E272 (Ref. 3.9). The hadronic shower profile is broader than the electromagnetic distribution and has a long low energy "tail" extending away from the peak. The reconstruction program frequently misinterpreted an energy fluctuation in the "tail" of a hadronic shower as a second particle [5.13]. The hadron's transverse momentum was systematically underestimated because the "peak" associated with the fluctuation was assigned, on the average, ~10% of the total hadronic energy. (These low energy peaks were subsequently eliminated by the $p_T > 2.1$ GeV/c requirement imposed on single photon candidates.) This tendency to bias hadronic energies toward lower values helped to suppress the hadronic background. An energy scale shift of ~10% resulted in a factor of 2-3 reduction in the background level (i.e. see Chapter 6.A, Eq. 6.1). This effect was included in the definition of $F_h(p_T', p_T)$.

The function $F_h(p_T', p_T)$ was entered as a look-up table of average values, with intervals in p_T/p_T' of 0.05. Eq. 5.8 was numerically integrated for a series of p_T values and divided by the π^0 cross section. This yielded the apparent inclusive γ/π^0 ratio due to hadrons, shown in Table 5.1 as a function of p_T.

E. Reconstruction Losses

The reconstruction program occasionally erred in locating clusters of energy and correlating them, resulting in a loss of π^0's. This was another source of background single photons. Failures would be expected to occur more often in high multiplicity events where many possibilities for a mismatch existed in correlating between the two projections. Reconstruction losses were studied using events with two or more reconstructed photons by the following procedure.

Events containing at least one π^0 with a p_T in the range 2-4 GeV/c were selected from the data tapes. The highest p_T π^0 in such an event was replaced by a Monte Carlo generated π^0 of the same p_T. The π^0 position within the LAC was chosen randomly. In order to extend the study beyond 4 GeV/c, the fitted π^0 cross section was extrapolated, and events were generated according to this distribution in p_T and rapidity. The angles θ^* and ϕ^* for the isotropic decay into two photons were chosen randomly. Showers were then generated for this new event using the shower distribution function to partition energy among the front strips of the LAC. Energy was divided equally

between the X′ and Y′ projections. The energy in each strip was smeared by an amount ΔE to simulate the effects of energy resolution and noise. The values of ΔE were Gaussian distributed with a mean of zero and a width σ, where σ^2 consisted of a constant term representing the mean noise per strip and a term proportional to the energy [5.14]. Single strip peaks in the raw data were used to determine the value for the constant term. These usually resulted from electronic noise in the detector although they were sometimes caused by very low energy photons or out-of-time photons. These peaks were classified as noise, since they were unlikely to be caused by real, in-time photons with ~1 GeV of energy. The standard deviation of the energy distribution of the single strip peaks was ≈30 MeV. Using this value for the noise per strip, Monte Carlo π^0′s were sprayed into the detector with different trial choices for the coefficient of the energy-dependent term. The best agreement between the width of the π^0 mass distribution in the Monte Carlo and the 2γ events in the data occurred for an energy resolution (per strip) of

$$\sigma^2(\text{GeV}) = [\ (0.15\sqrt{E\ (\text{GeV})}\ ]^2 + (0.03)^2. \qquad (5.9)$$

Upon completion of the shower generation process, the event was analyzed by the photon reconstruction program. If the low energy photon was not reconstructed, the remaining photon contributed to the single photon background. Values of $(\gamma/\pi^0)_{recon}$ for different p_T intervals are listed in Table 5.1. The entries are for total photon multiplicities 2-8 weighted according to the number of events in each

class. Below 5 GeV/c, π^0 energies were too low for shower coalescence to be appreciable. Only at higher p_T values did coalescence have an effect on the $(\gamma/\pi^0)_{recon}$ level; in the range 5-6 GeV/c, it rose by ~0.5%. This was verified qualitatively by: (1) performing a visual inspection of raw pulse height data for single photon candidates with $p_T>4$ GeV/c, and (2) by using the first and second moments of the pulse height distribution to calculate the invariant masses associated with single showers [5.15].

Figure 5.4 shows how the π^0 reconstruction efficiency varied with asymmetry for different multiplicity classes. Results are shown for 2-6 γ events. There were only 20 π^0's in the 7γ sample, and 5 in the 8γ sample with $p_T>2.0$ GeV/c. There was a deterioration of efficiency with increasing multiplicity. However, the efficiency was respectable even for high multiplicities. For the four photon events, the correlation between π^0 reconstruction efficiency and position in the LAC was examined. No significant position dependence was apparent.

The causes of the reconstruction losses were studied by examining dumps of events in which π^0's were lost. Energy fluctuations were one major reason for the loss of π^0's in reconstruction. When two or more photons in an event had nearly the same energy, small fluctuations in shower energy made it difficult to properly correlate clusters in the X' and Y' projections. A mismatch yielded the wrong positions, and therefore the wrong mass, for the photon pair. Energy fluctuations were largely responsible for the

Figure 5.4

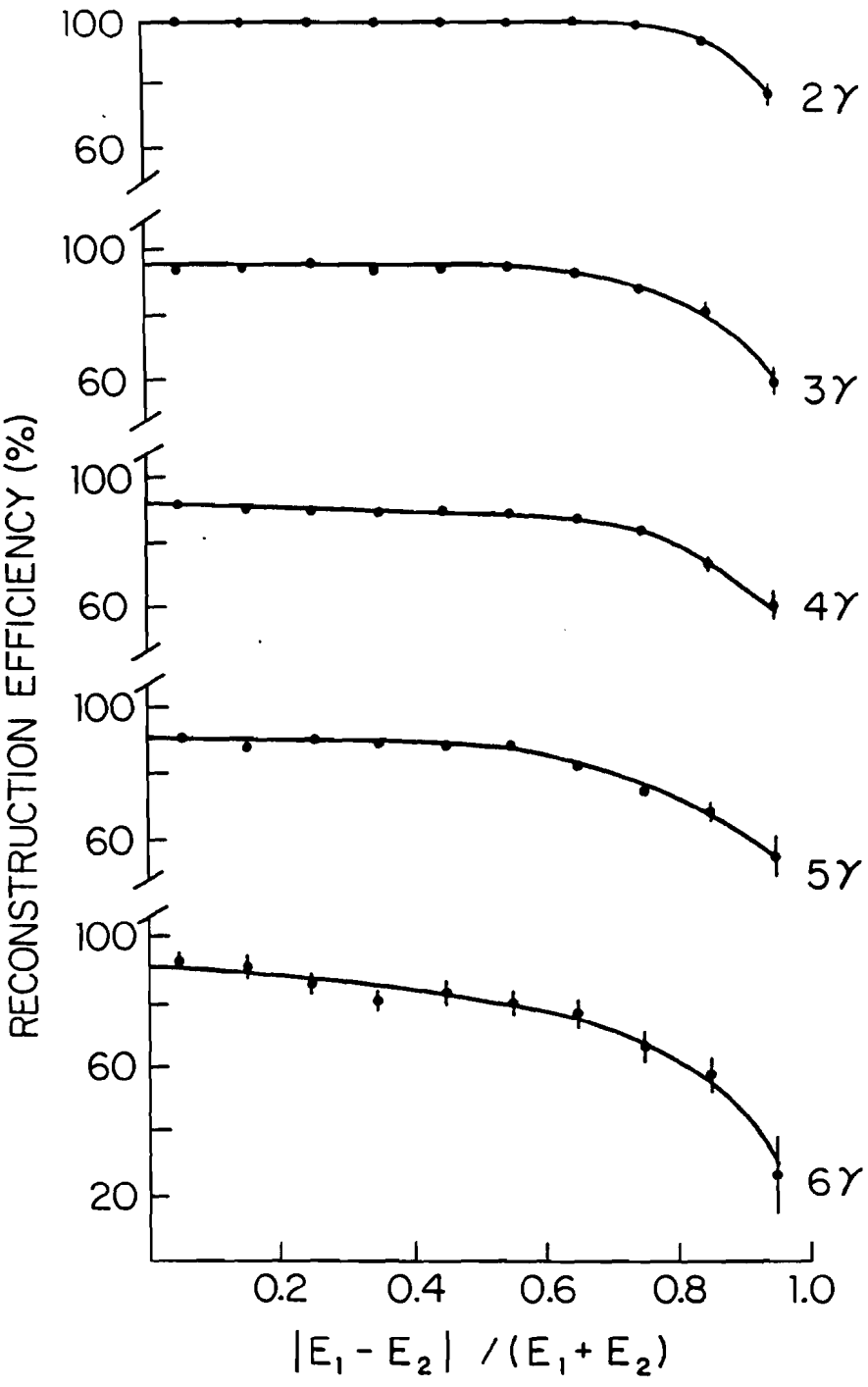
100
60
2γ
100
60
3γ
100
60
4γ
100
60
5γ
100
60
20
6γ
RECONSTRUCTION EFFICIENCY (%)
0.2
0.4
0.6
0.8
1.0
|E1 - E2| /(E1 + E2)

loss of π^0's that decayed asymmetrically, with one photon of low energy. Some losses were caused by a photon fluctuating below the one GeV cutoff. Alternately, both π^0 photons may have been reconstructed, but with a 2γ invariant mass outside the allowed range. These effects were more significant in the higher multiplicity data, because the energy spectrum of the background photons not associated with the π^0 tended to peak near one GeV. Thus, the low energy π^0 photon was often mismatched. These effects, associated with fluctuations in shower energy, accounted for ~65% of the π^0 loss in 4γ events.

Another major source of loss was the occurrence of multiple overlaps. Suppose that two photons overlapped in one view, and that a third photon overlapped with one of those photons in the other view. In this situation, there would have appeared to be only two peaks in each of the two views, even though three photons were actually present. Worse cases, such as triple overlaps (i.e. a three photon event in which all the photons overlapped in one view, thus yielding three peaks in one projection but only one peak in the other) also occurred, but less often. The reconstruction algorithm was not designed to deal with these types of events, and had difficulty in forming the correct energy correlations with information from only two views. This accounted for some of the losses at low asymmetries. In four photon events, as the π^0 asymmetry approached zero the losses remained constant at about 8% because multiple overlaps occurred in an essentially random and energy-independent manner. This effect accounted for roughly 35% of the π^0 loss in 4γ events.

F. Conversion Electrons

A photon had a probability of ~2.5% for converting into an e^+e^- pair inside the target (5% radiation length target segments, with interactions halfway through on the average). Pairs that had a sufficiently large angular divergence were reconstructed as two distinct showers in the LAC. The angular spread was energy-dependent. Single photons and π^0's of the same p_T were therefore affected differently, since the π^0 energy was divided between two photons. The magnitude of the effect that photon conversions had on the γ/π^0 ratio was calculated in the following manner.

No analyzing magnet was used in this experiment. The angular spread between e^+e^- pairs was due mainly to multiple Coulomb scattering as the particles passed through material. The RMS scattering angle for an electron is given by [5.16]

$$\theta_{RMS} \approx \frac{21 \text{ MeV}}{p\beta c} \sqrt{(L/L_R)} \qquad (5.10)$$

where L/L_R is the thickness of the material in units of radiation length, p is the electron momentum, and βc is the electron's velocity in the laboratory frame. The LAC was approximately 8 m downstream of the target. The RMS separation between an electron and positron, each carrying roughly half of the photon energy E, is

$$\delta s \text{ (cm)} \approx \frac{7.5}{E \text{ (GeV)}} \qquad (5.11)$$

at the Z′-position of the LAC.

Studies of the reconstruction program, described in the previous section, indicated that two showers were resolvable if the centroids were separated by >2.5 cm in either view. This, in conjunction with Eq. 5.11, implies that photons with E>3 GeV were reconstructed as single showers. Single photons with less than 3 GeV of energy did not contribute to the high p_T signal; a 2 GeV/c photon had to have at least 10 GeV of energy because of the geometry of the experiment.

The main problem arose in asymmetric π^0 decays, when the low energy photon converted and was "lost" in the sense that no pair of reconstructed photons satisfied the π^0 mass cut. The remaining decay photon, carrying a much larger fraction of the π^0 energy, was then free to contribute to the single photon background. The background level was estimated by selecting π^0′s in which one photon had an energy in the range 1-3 GeV [5.17]. The p_T spectrum of the remaining π^0 photons, weighted for acceptance and normalized by the conversion probability of 2.5%, indicated a γ/π^0 background level of <0.1% [5.18]. The data were not corrected for this negligibly small effect.

CHAPTER 6

Results and Conclusions

The experimental results are presented in this chapter [6.1]. Systematic errors are estimated in the first section. Cross section measurements for π^0, η, ω, and η' mesons produced on nuclear targets are presented in section B. The data on direct photon production are shown in section C. In the final section, these data are discussed and the conclusions are summarized.

A. Sources of Systematic Error

The errors quoted for the results presented in sections B and C are statistical. There are, in addition, overall systematic uncertainties in the measurements.

The principal source of systematic error in the overall normalization for the inclusive cross sections was uncertainty in the

p_T scale calibration. The steep falloff of the p_T spectrum implies that small shifts in p_T lead to large shifts in the absolute normalization. The p_T of a particle carrying energy E, and travelling at an angle θ with respect to the beam axis, is $E\sin\theta$. For the geometry of this experiment, $p_T = p_{Tx}$, where $p_{Tx} = Ex/z$ [6.2]. Thus,

$$(\frac{\Delta p_T}{p_T})^2 = (\frac{\Delta E}{E})^2 + (\frac{\Delta x}{x})^2 + (\frac{\Delta z}{z})^2. \qquad (6.1)$$

The inclusive cross sections were parameterized by an exponential, $Ae^{(-Bp_T)}$. A shift in p_T is equivalent to a change in the normalization of

$$|\frac{\Delta A}{A}| = |Bp_T\frac{\Delta p_T}{p_T}|. \qquad (6.2)$$

Fits to the π^0 data yielded B~4. The average p_T is ~2.35 GeV/c. The percentage error in the normalization constant is therefore roughly ten times the percentage error in the p_T scale.

The π^0 and η masses were simultaneously constrained to ~1% of their accepted values (Chapter 4.E). From Eq. (3.2), for $\Delta\theta = 0$ and $E_1 = E_2 \equiv E$,

$$\frac{\Delta E}{E} = \sqrt{2}\frac{\Delta m}{m}. \qquad (6.3)$$

The uncertainty in the energy scale calibration is therefore ≈1.4%. This is consistent with an estimate based on the magnitude of

variations in the trigger rate. The number of triggers, normalized to the beam flux, fluctuated by 17% over the course of the experiment (for a particular target). This variation is indicative of the uncertainty in the absolute normalization due to effects such as systematic amplifier gain drifts.

It was not known precisely where a beam-target interaction occurred. There were two target segments, separated by 25 cm and equidistant from the origin (Chapter 2.C). The point of interaction was assigned a Z-position of zero; this introduced a Δz of ± 12.5 cm. Variations in the median depth of a shower also affect Δz. To a good approximation, it depends logarithmically on the energy (Ref. 2.7). At fixed energy, the statistical nature of the cascade development is responsible for fluctuations in the median depth. The $\Delta z'$ (essentially the same as Δz -- see Ref. 6.2) introduced by these effects was calculated using analytic formulae for electromagnetic shower development (Ref. 2.7). The uncertainty in the shower depth was estimated to be ± 2.5 cm. (The radiation length of lead is much smaller than the radiation length of liquid argon or G-10. The cascade development occurs primarily in the lead sheets, which are separated by gaps. The calculation took into account the fact that a small shift in energy or a small fluctuation can shift the median of a shower across a gap.) The overall $\Delta z/z$ was estimated to be ~1%.

The X-position of the LAC relative to the beam axis was known to ± 1 cm, or 1%. The effect of shifts in the shower depth on Δx was negligible.

These sources of error lead to an uncertainty in the p_T scale of roughly 2% (Eq. 6.1). The corresponding error in the absolute normalization is therefore ≈20% (Eq. 6.2).

A number of other effects were also considered. The p_T scale is affected by the energy resolution of the LAC [6.3]. (The error associated with the energy scale calibration was discussed in a previous paragraph; this error is a consequence of choosing an incorrect overall normalization factor for the ADC count to energy conversion. The resolution effect described in this paragraph is, in a sense, a relatively small "second-order" shift. Because it affects the energy scale in a less direct and somewhat more subtle manner, it is discussed separately.) Because the p_T spectrum falls steeply, the number of low p_T (energy) events is larger than the number at high p_T. There is an imbalance between the number of events which feed into and out of a given p_T interval, which results in a shift of the p_T scale. The energy scale was calibrated by normalizing to the π^0 mass. This tends to correct for the shift, but the compensation is not complete over the entire p_T range. A Monte Carlo calculation indicated that the uncertainty introduced in the absolute normalization by the LAC energy resolution was of order 12%.

The global p_T trigger model was based on the assumption that the low threshold trigger was 100% efficient in the kinematic region to which the acceptance correction was applied. If this was not the case, cross sections were underestimated. The efficiency of the low threshold trigger was not measured directly. It was assumed that the

efficiency curve had the same shape as that of the high threshold trigger (Fig. 5.1), but was shifted along the p_T scale to a global threshold setting of 1.6 GeV/c. At a p_T of 2.1 GeV/c, the efficiency of the low threshold trigger is estimated to be ≈90%; above 2.3 GeV/c, the efficiency is 95-100%. Thus, the cross sections may be off by 5-10%, depending on the p_T.

The beam flux was measured using an XY hodoscope. The efficiency of a plane was measured and found to be >98% (Ref. 2.4). The hodoscope was designed to limit the counting rate in individual elements to a few MHz at the nominal beam intensity. There was no indication that the counting rate approached the instrumental limit -- during a particularly bad excursion in the beam intensity, 2.1×10^7 counts (twice the normal flux) were recorded during a one second spill. Beam was counted independently on two scalers, which agreed to ~0.04%. Based on the hodoscope efficiency measurement, a systematic error of 2% was assigned to the "live" beam flux. (Other counters used to define this signal were essentially 100% efficient.)

The determination of the proton and pion content of the beam was sensitive to the values used for the Cerenkov counter detection efficiency (80±10%) and the background level due to particles falsely tagged as pions (2.0±0.6%). The systematic error on the proton flux due to Cerenkov tagging was estimated to be ≈2%, and ≈15% on the pion flux [6.4].

Combining the contributions from these different effects in quadrature, the systematic error on the cross section normalization is

≈20% for incident protons, essentially all of which is associated with the p_T scale. For incident pions, the uncertainty in the pion flux is also significant. The systematic error is estimated to be ≈25%.

These effects biased the γ and π^0 cross sections in essentially the same manner, and tended to cancel out in the γ/π^0 ratio. The background predictions in Table 5.1 were sensitive to some specific features of the Monte Carlo model, the most significant being the parameterizations of the cross sections and the size of the LAC fiducial area. By adjusting these inputs, the uncertainty in the background level was estimated to be ±2%.

The pretrigger signal consisted in part of an "interacting beam" requirement. Charged particles produced by interactions in the target were detected using scintillation counters which straddled the beam region. A high p_T single particle trigger is expected to be accompanied by other hadrons produced in the fragmentation of a parton; in contrast, single photons may be produced without accompanying hadrons. Thus, it is possible that the pretrigger was biased against single photons. However, measurements at the ISR (Ref. 1.46) on the structure of events with high p_T π^0 and single γ triggers indicate that there are no significant differences in the away-side jets of these two classes of events. Since the interaction counters used in this experiment were positioned on each side of the beam (Chapter 2.F), this pretrigger bias is believed to be negligible in comparison to the systematic uncertainties in the Monte Carlo.

The γ/π^0 ratio is also sensitive to nonlinearities in the energy scale introduced by the calorimeter and by the reconstruction procedure (i.e. see Chapter 3.C). At a given p_T, a single photon typically has twice the energy of a photon produced in a $\pi^0 \rightarrow \gamma\gamma$ decay. A nonlinear energy response results in a shift of the γ p_T scale relative to that of the π^0. The absolute normalization of the γ and π^0 cross sections are rescaled by different factors, which do not cancel when the ratio is taken. An experimental limit on the overall nonlinearity was determined using the π^0 data. (This approach tested the linearity of the calorimeter response and also the energy calculation performed by the reconstruction program -- π^0 identification depended on the recorded pulse height information and on how that data was processed.) The energy of one π^0 photon was required to be within ± 1 GeV of some fixed value, chosen to get good statistics; a set of energies in the range 8-18 GeV were tried, with consistent results for each value. The π^0 mass was measured as a function of the second photon's energy, which typically ranged from 1-20 GeV. A nonlinear energy response would have resulted in a dependence of the π^0 mass on photon energy. No such dependence was observed. The data set a limit of $\pm 1.5\%$ on the γ/π^0 ratio at 4-5 GeV/c p_T. The effect is less at lower p_T values [6.5]. This limit is consistent with those discussed in Chapter 3.C.

B. Inclusive Cross Sections for Neutral Mesons

The differential cross sections per nucleus for π^0 and η production were calculated as a function of p_T. As discussed in Chapter 5.B, a cutoff on p_T was imposed that varied with the rapidity interval. Above these cutoffs, the trigger efficiency exceeded 20%. There was no discernable dependence of the π^0 or η cross sections on rapidity. Consequently, data from different regions were combined for p_T values above the respective cutoffs (see Ref. 5.4). The π^0 cross sections for the beryllium, carbon, and aluminum targets, measured with incident proton and π^+ beams are shown in Table 6.1 for different p_T bins. Table 6.2 shows the η cross sections measured on the same three targets with incident protons, and on carbon with incident π^+ beam. There were not enough data to measure the η cross sections for pions incident on beryllium or aluminum targets. The proton data are plotted in Figure 6.1. Figure 6.2 is a similar plot which displays the π^+ data.

The nuclear target dependence of the cross sections was parameterized by the commonly used form A^{α} (Chapter 1.D). No significant variation of α with p_T or rapidity was observed in the fitted values. Consequently, the data are integrated over these variables. The π^0 data lie between p_T=2.1 and 4.0 GeV/c ($\langle p_T \rangle \approx$ 2.35 GeV/c). For the η, the limits in p_T are 2.3-3.0 GeV/c ($\langle p_T \rangle \approx$ 2.5 GeV/c). The mean rapidities are $\langle y_{cm} \rangle_{\pi^0} \approx -0.3$, and $\langle y_{cm} \rangle_{\eta} \approx -0.1$. The results for α are:

TABLE 6.1

Invariant cross sections for π^0 production (cm^2/Gev^2/Nucleus) averaged over the p_T bin and the center of mass rapidity interval (-0.75 to +0.2).

p_T(GeV/c)	pBe	π^+Be	pC	π^+C	pAℓ	π^+Aℓ
2.15	$1.03\pm0.11\times10^{-29}$	$8.4\pm2.6\times10^{-30}$	$1.47\pm0.04\times10^{-29}$	$1.19\pm0.11\times10^{-29}$	$3.51\pm0.32\times10^{-29}$	$2.94\pm0.87\times10^{-29}$
2.25	$7.47\pm0.83\times10^{-30}$	$7.4\pm2.3\times10^{-30}$	$1.07\pm0.03\times10^{-29}$	$7.88\pm0.90\times10^{-30}$	$2.55\pm0.24\times10^{-29}$	$1.89\pm0.69\times10^{-29}$
2.35	$6.04\pm0.49\times10^{-30}$	$6.9\pm1.6\times10^{-30}$	$7.13\pm0.19\times10^{-30}$	$4.93\pm0.47\times10^{-30}$	$1.81\pm0.14\times10^{-29}$	$1.52\pm0.36\times10^{-29}$
2.45	$3.71\pm0.36\times10^{-30}$	$3.0\pm0.9\times10^{-30}$	$4.57\pm0.13\times10^{-30}$	$3.83\pm0.35\times10^{-30}$	$1.12\pm0.10\times10^{-29}$	$1.04\pm0.30\times10^{-29}$
2.55	$2.41\pm0.27\times10^{-30}$	$1.9\pm0.8\times10^{-30}$	$2.95\pm0.10\times10^{-30}$	$2.79\pm0.29\times10^{-30}$	$8.66\pm0.78\times10^{-30}$	$9.5\pm2.3\times10^{-30}$
2.65	$1.73\pm0.18\times10^{-30}$	$1.1\pm0.4\times10^{-30}$	$2.02\pm0.07\times10^{-30}$	$2.14\pm0.19\times10^{-30}$	$5.75\pm0.51\times10^{-30}$	$4.1\pm1.6\times10^{-30}$
2.75	$8.68\pm1.12\times10^{-31}$	$1.2\pm0.3\times10^{-30}$	$1.30\pm0.05\times10^{-30}$	$1.10\pm0.14\times10^{-30}$	$3.79\pm0.39\times10^{-30}$	$3.7\pm1.0\times10^{-30}$
2.85	$7.48\pm0.97\times10^{-31}$	$8.4\pm2.9\times10^{-31}$	$8.56\pm0.38\times10^{-31}$	$9.6\pm1.1\times10^{-31}$	$2.14\pm0.28\times10^{-30}$	$2.5\pm0.9\times10^{-30}$
2.95	$3.92\pm0.64\times10^{-31}$	$5.0\pm2.0\times10^{-31}$	$6.22\pm0.31\times10^{-31}$	$6.0\pm0.9\times10^{-31}$	$1.53\pm0.23\times10^{-30}$	$1.6\pm0.6\times10^{-30}$
3.10	$2.51\pm0.37\times10^{-31}$	$4.2\pm1.3\times10^{-31}$	$3.57\pm0.16\times10^{-31}$	$3.3\pm0.5\times10^{-31}$	$8.0\pm1.1\times10^{-31}$	$8.3\pm3.1\times10^{-31}$
3.30	$9.6\pm2.1\times10^{-32}$	$1.6\pm0.7\times10^{-31}$	$1.64\pm0.10\times10^{-31}$	$1.8\pm0.3\times10^{-31}$	$3.9\pm0.7\times10^{-31}$	$9.5\pm3.0\times10^{-31}$
3.50	$6.7\pm1.7\times10^{-32}$	$6.8\pm5.9\times10^{-32}$	$7.23\pm0.67\times10^{-32}$	$1.0\pm0.2\times10^{-31}$	$2.7\pm0.6\times10^{-31}$	$1.8\pm1.3\times10^{-31}$
3.80	$2.1\pm0.6\times10^{-32}$	$3.8\pm2.6\times10^{-32}$	$2.56\pm0.25\times10^{-32}$	$1.7\pm0.7\times10^{-32}$	$9.8\pm2.4\times10^{-32}$	$1.8\pm0.8\times10^{-31}$
4.25			$5.5\pm1.0\times10^{-33}$	$4.8\pm2.2\times10^{-33}$	$1.3\pm0.9\times10^{-32}$	
4.75			$1.0\pm0.4\times10^{-33}$			

TABLE 6.2

Invariant cross sections for η production ($cm^2/Gev^2/Nucleus$) averaged over the p_T bin and the center of mass rapidity interval (-0.5 to +0.1).

p_T(GeV/c)	pBe	pC	π^+C	pAℓ
2.40	$2.1\pm0.8\times10^{-30}$	$2.9\pm0.3\times10^{-30}$	$2.9\pm1.0\times10^{-30}$	$7.4\pm2.4\times10^{-30}$
2.60	$4.1\pm3.4\times10^{-31}$	$1.2\pm0.2\times10^{-30}$	$4.8\pm3.7\times10^{-31}$	$2.3\pm1.0\times10^{-30}$
2.85	$1.5\pm1.2\times10^{-31}$	$4.9\pm0.6\times10^{-31}$	$3.8\pm1.7\times10^{-31}$	$1.2\pm0.5\times10^{-30}$
3.20	$6.4\pm4.3\times10^{-32}$	$1.5\pm0.2\times10^{-31}$	$1.3\pm0.6\times10^{-31}$	
3.70	$3.4\pm1.8\times10^{-32}$	$2.6\pm0.7\times10^{-32}$		
4.50		$1.2\pm1.1\times10^{-33}$		

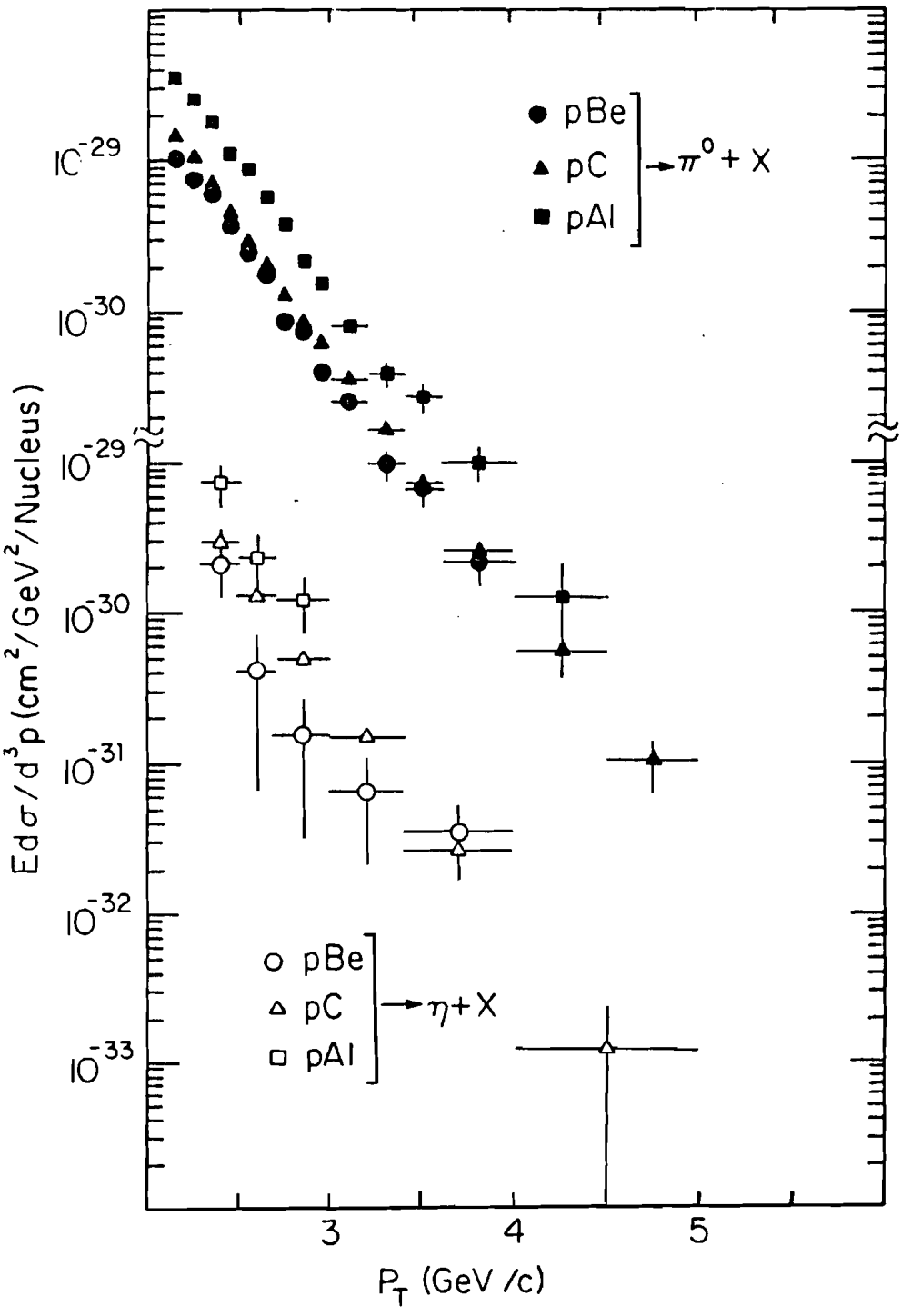
pBe
pC
pAl
→π⁰ + X
pBe
pC
pAl
→η+X
Ed σ/d³p (cm²/GeV²/Nucleus)
P_T (GeV /c)
10⁻²⁹
10⁻³⁰
10⁻²⁹
10⁻³⁰
10⁻³¹
10⁻³²
10⁻³³
3
4
5

Figure 6.1

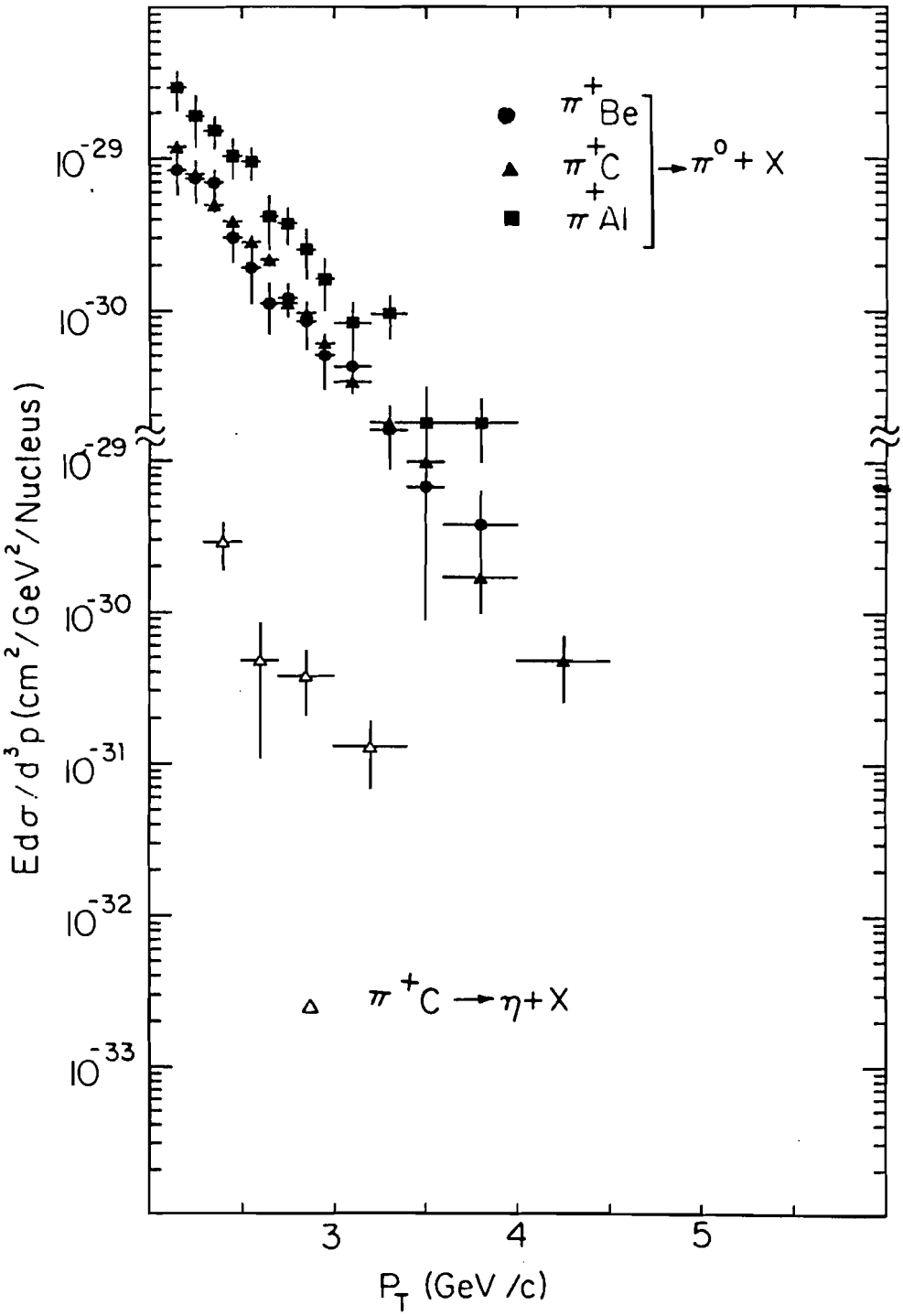
π^+ Be
π^+ C
π^+ Al
$\rightarrow \pi^0 + X$
$\pi^+ C \rightarrow \eta + X$
$E d\sigma/d^3p$ (cm^2/GeV^2/Nucleus)
10^{-29}
10^{-30}
10^{-29}
10^{-30}
10^{-31}
10^{-32}
10^{-33}
3
4
5
P_T (GeV /c)

Figure 6.2

$$\alpha_{\pi^0} = 1.11 \pm 0.05 \text{ for } pN \to \pi^0 + X,$$

$$\alpha_{\eta} = 1.14 \pm 0.30 \text{ for } pN \to \eta + X,$$

and

$$\alpha_{\pi^0} = 1.11 \pm 0.15 \text{ for } \pi^+ N \to \pi^0 + X.$$

These results are consistent with previous measurements of $\alpha_{\pi^\pm}$ in the same p_T range (Ref. 1.33). The values of α reported at a p_T of 3.08 GeV/c, for 200 GeV/c incident protons, were $\alpha_{\pi^+}=1.11\pm0.02$ and $\alpha_{\pi^-}=1.10\pm0.02$.

The π^0 cross section has been previously measured in 200 GeV pC, pBe, pp, and π^+p collisions at Fermilab, near 90° in the center of mass [6.6]. (There have been no previous measurements of π^0 or η production for π^+-nucleus interactions in a comparable kinematic region.) The E629 data are consistent with the results obtained in these experiments; they are also in agreement with the $pBe \to \pi^\pm + X$ data of Ref. 1.33, when the latter are averaged over π^+ and π^- production.

Within experimental errors, the π^0 and η cross sections have the same p_T dependence. The ratio of η to π^0 production averaged over the carbon data for incident protons was calculated by constraining the slope of the exponential and adjusting the overall normalization. The η/π^0 ratio is 0.53 ± 0.03, which is in agreement with measurements at large p_T on hydrogen [6.7] and beryllium (Ref. 1.41) targets at 200 GeV/c.

One early indication that large p_T meson production processes could be related to the hard scattering of constituents was provided by Donaldson et al. (Ref. 6.6). The π^0 yield at large p_T in π^+p

collisions was larger than that observed in the pp reaction [6.8]. Donaldson et al. (Ref. 6.6) and Corcoran et al. (Ref. 6.8) attributed this increase to the higher probability for finding a large x valence quark in the pion structure function. In Figure 6.3, the ratio $(pA \rightarrow \pi^0+X)/(\pi^+A \rightarrow \pi^0+X)$ is plotted versus p_T for the three nuclear targets used in this experiment, and compared to data on hydrogen from Donaldson et al. (Ref. 6.6). In addition to the statistical errors shown for each E629 data point, there is a systematic uncertainty of 17% associated with the beam flux determination. (As discussed in section A, there is an estimated 2% error assigned to the proton beam count and an estimated 15% error in the π^+ flux measurement. These errors are correlated. The overall uncertainty is therefore ~17%.) The similar behavior of the two data sets suggests that the mechanism responsible for enhanced meson production on nuclear targets (i.e. $\alpha>1$) does not obscure the differences observed in hard interactions of pions and protons on hydrogen.

As discussed in Chapter 1.B, invariant cross sections deviate from the p_T^{-4} dependence expected in a scaling parton scattering model. The $\sqrt{s}$ dependence of π^0 production was studied using the E629 pC data at $\sqrt{s}$=19.4 GeV, and pp data from CERN experiment R806 at $\sqrt{s}$ = 44.8, 52.7, and 62.8 GeV [6.9]. (The nuclear target dependence of π^0 production was discussed earlier in this section -- the E629 measurements were scaled by a factor $A^{1.1}$ to obtain cross sections per nucleon.) The data were fit to the form

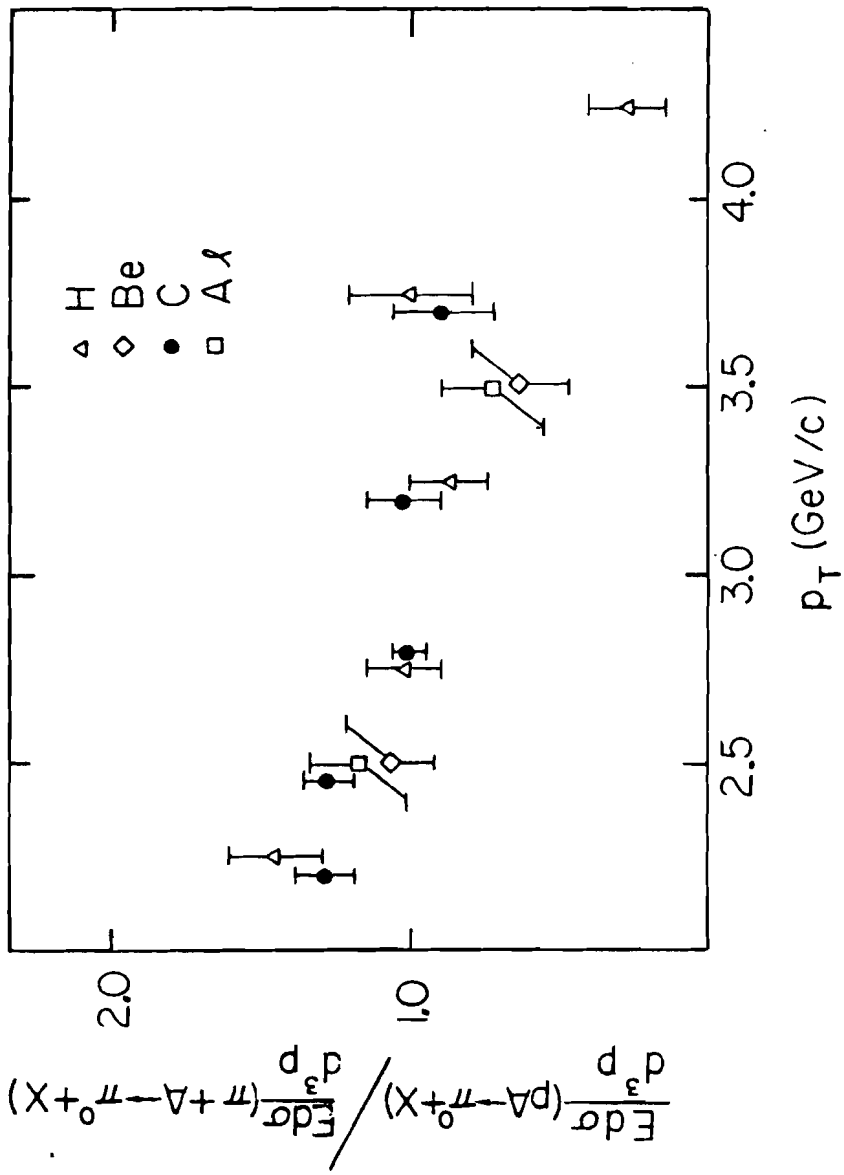
H
Be
C
Al
2.0
1.0
2.5
3.0
3.5
4.0
p_T (GeV/c)
$\frac{E\,d\sigma}{d^3p}(pA\to\pi^0+X) \Big/ \frac{E\,d\sigma}{d^3p}(\pi^+A\to\pi^0+X)$

Figure 6.3

$$E\frac{d\sigma}{d^3p} = C(1-x_T)^m p_T^{-n}. \qquad (6.4)$$

Initially, all of the R806/E629 data (including R806 π^0 cross section measurements at $\sqrt{s}$=30.6 GeV) were fit. The parameters in Eq. 6.4 were found to be rather sensitive to shifts in the relative normalization of measurements performed at different energies. (However, it was possible to obtain an acceptable fit to the R806 data at four different $\sqrt{s}$ values.) The relative cross section normalization was much less problematical when data below a p_T of 2.6 GeV/c (entirely from E629) and the 30.6 GeV R806 data were excluded from the fit; these restrictions were adopted in order to reduce the systematic uncertainties in the values of m and n (Eq. 6.4). The 2.6 GeV/c p_T cut was also imposed in the fits to the direct photon cross section described in the following section. (The cause of the problem described above is not clearly understood. It is possible that the trigger model is not reliable below 2.6 GeV/c. Alternately, the simple functional form in Eq. 6.4 may not provide an adequate description of the process over the p_T range spanned.)

The values n = 8.28±0.04, m = 9.6±0.1, and C = (9.2±0.7) x 10^{-27} were obtained from the fit, with a χ^2 per degree of freedom of 49/63. A 30% shift in relative normalization introduced a change of ~0.3 in the value of n and a change in m of ~1.3. These data and the fit are shown in Figure 6.4; the cross sections (and the function in Eq. 6.4) have been scaled by $p_T^{8.28}$ and are plotted versus x_T. In the

Figure 6.4

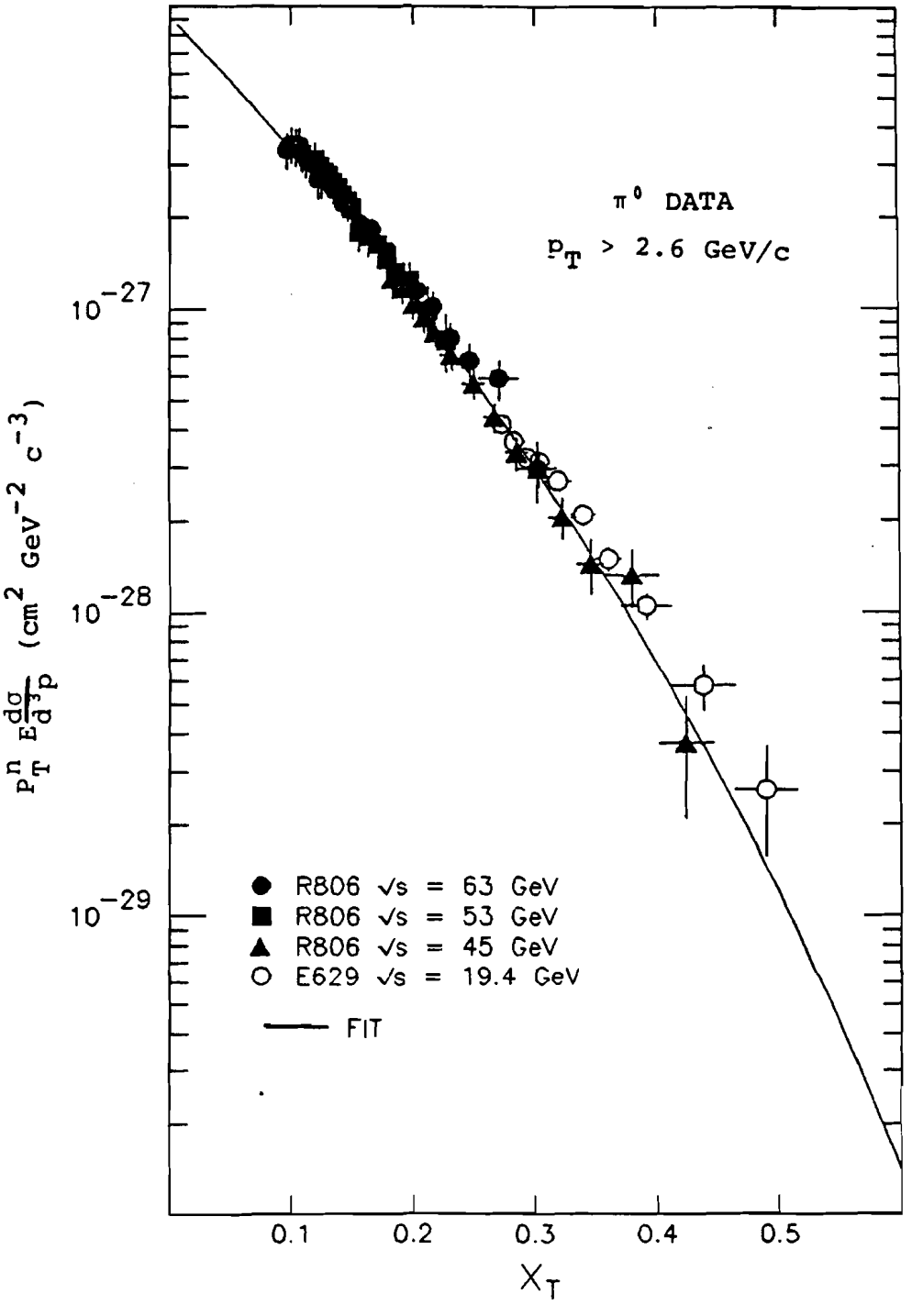
π^0 DATA
p_T > 2.6 GeV/c
10^{-27}
10^{-28}
10^{-29}
$p_T^n E\frac{d\sigma}{d^3p}$ (cm^2 GeV^{-2} c^{-3})
R806 √s = 63 GeV
R806 √s = 53 GeV
R806 √s = 45 GeV
E629 √s = 19.4 GeV
FIT
0.1
0.2
0.3
0.4
0.5
X_T

following section, this result is compared to a similar fit performed using R806 and E629 data on inclusive direct photon production.

The $\omega \rightarrow \pi^0\gamma$ event sample was too small to measure the production cross section at more than one p_T value. By inspecting the three-photon invariant mass distribution for pC data (Fig. 4.12), it was estimated that there were 30 ± 10 $\omega \rightarrow \pi^0\gamma$ events between 2.6 and 3.0 GeV/c p_T (Chapter 4.E). The Monte Carlo program was modified to calculate the ω acceptance, as discussed in Chapter 5.C. The cross section per nucleus was

$$Ed\sigma/d^3p\ (pC \rightarrow \omega + X) = (1.2\pm0.4) \times 10^{-30}\ cm^2/GeV^2/c^3$$

at $\langle y_{cm} \rangle = -0.2$ and $\langle p_T \rangle = 2.75$ GeV/c. (As mentioned above, the ω cross section was not measured as a function of p_T. The average transverse momentum was calculated by assuming an $\exp(-4p_T)$ dependence for $Ed\sigma/d^3p$, as was the case for the π^0.) The ω/π^0 production ratio at this point was 0.9 ± 0.3.

There was no discernable signal for the $\eta' \rightarrow \gamma\gamma$ decay mode. To set an upper limit on the $pC \rightarrow \eta' + X$ cross section, it was assumed that the signal had been lost because of a two standard deviation statistical fluctuation in the background level near the expected η' peak. There were ~80 events with a mass between 900 and 1000 MeV/c^2 ($\sigma \sim \sqrt{80}$). in the p_T range 2.6-3.0 GeV/c. Therefore, a two standard deviation fluctuation would have corresponded to ~18 η' particles. Corrections for the η' acceptance, branching ratio, and other normalization factors (i.e. Table 4.2) were applied. An upper limit

of 1.2×10^{-30} cm²/GeV²/c³ at $\langle p_T \rangle$ = 2.75 GeV/c and $\langle y_{cm} \rangle$ = -0.3 was established for the η' cross section per nucleus. This implies a 2σ upper limit of 0.9 for the η'/π^0 production ratio.

The high p_T production of ω and η' mesons has been previously measured in 200 GeV/c pBe collisions at Fermilab [6.10] and in $\sqrt{s}$ = 31-62 GeV pp collisions at the ISR [6.11]. Donaldson et al. (Ref. 6.10) quoted a value for ω/π^0 of 0.44±0.08 and an upper limit (95% confidence level) for η'/η of 1.4 (corresponding to an η'/π^0 upper limit of <0.7). These measurements were made for the kinematic range $x_L \equiv (p_L/p_{max})_{cm}$ = 0.0-0.4 and p_T>2.2 GeV/c. Diakonou et al. (Ref. 6.11) obtained the values ω/π^0 = 0.87±0.17 and η'/π^0 = 0.9±0.25. These measurements were made at 90° in the center of mass, for p_T = 3.5-7 GeV/c. The E629 data are consistent with both of the previous experiments. The ω/π^0 ratio appears to be in somewhat better agreement with the ISR result.

C. Direct Photon Data

The ratio of direct photon candidates, corrected for geometric acceptance and trigger efficiency, to the inclusive π^0 yield is plotted in Figures 6.5a ($pC \rightarrow \gamma/\pi^0+X$) and 6.5b ($\pi^+C \rightarrow \gamma/\pi^0+X$). The predicted background contributions to these ratios, listed in Table 5.1, are indicated by the shaded bands. The widths of the bands represent the ±2% systematic uncertainties in the Monte Carlo background calculation. The additional systematic uncertainty due to

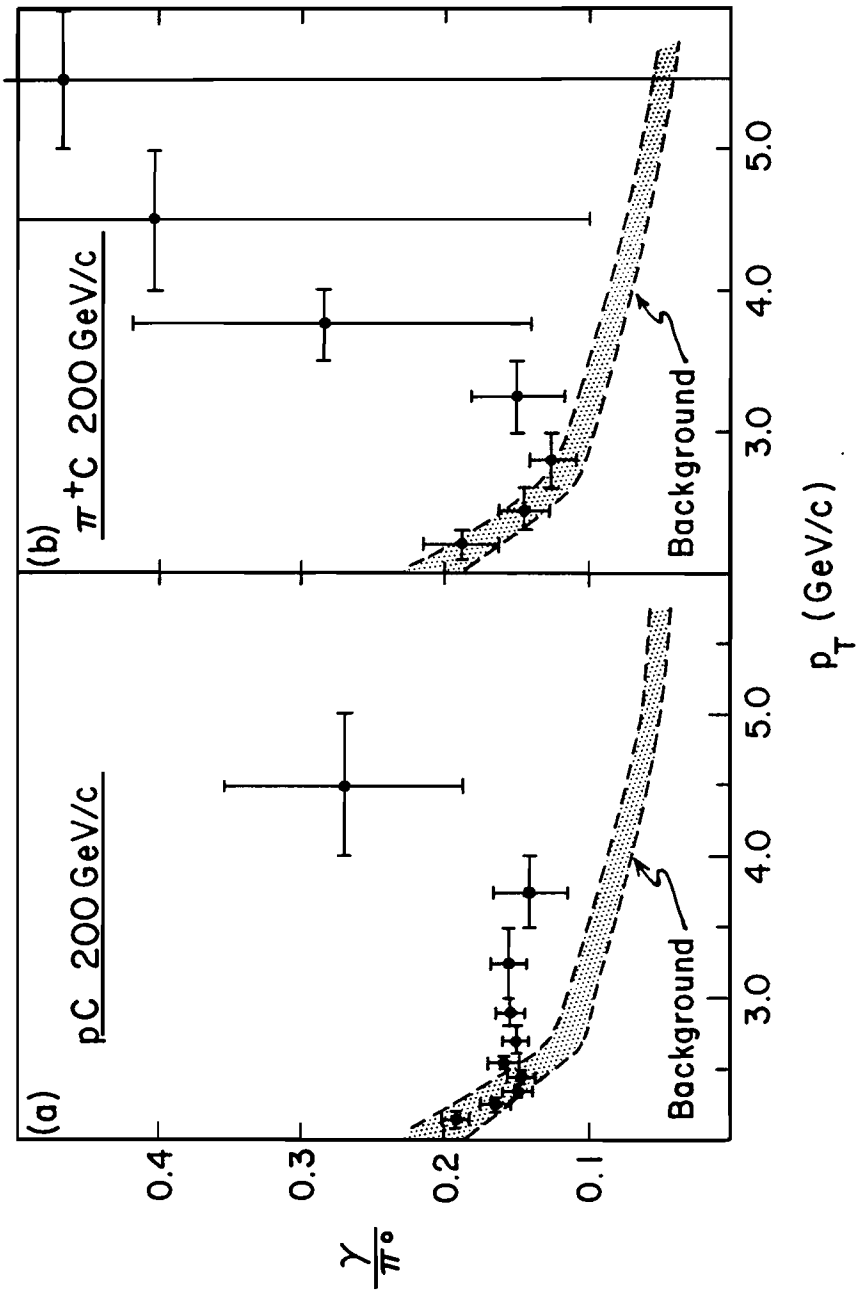
(a)
pC 200GeV/c
(b)
π^+C 200GeV/c
Background
Background
$\frac{\gamma}{\pi^0}$
0.4
0.3
0.2
0.1
3.0
4.0
5.0
p_T (GeV/c)

Figure 6.5

detector nonlinearity is not included. This is negligible at low p_T, but may be comparable in magnitude to the systematic error associated with the Monte Carlo near 5 GeV/c.

Below p_T~2.5 GeV/c, the signal is consistent with the level expected from background, to within the statistical and systematic uncertainties. Although the background level decreases as the transverse momentum increases, the signal for p_T≈3-4 GeV/c is roughly flat at a level of ~15% in pC collisions. The average background-subtracted γ/π^0 ratio for the pC data in the 3-5 GeV/c region is 6.5±1.6%; for π^+C interactions in this p_T range, the average background-subtracted ratio is 6.8±3.6%.

The inclusive cross sections for direct photon production were obtained by multiplying the background-subtracted γ/π^0 ratios by the π^0 cross sections. These ratios and the corresponding cross sections on carbon are presented in Table 6.3 as a function of p_T.

The background-subtracted results for direct photon production in pBe, pAl, π^+Be, and π^+Al interactions are shown in Table 6.4; the data for pBe and pAl reactions are compared with the pC data in Figure 6.6. There is essentially no single photon excess below p_T=3 GeV/c, but some evidence for an effect at higher p_T.

When comparing the E629 data to that of other experiments, it should be kept in mind that the γ/π^0 ratios in pA and pp collisions are not necessarily the same. The A dependence of direct photon production remains an open question. If direct photon production varies as $A^{1.0}$ (as might be expected from a naive analog to Drell-Yan

TABLE 6.3

Background-subtracted γ/π^0 ratios and the invariant cross sections for direct photon production at 90° in the center of mass for 200 GeV/c collisions on carbon. The calculations of the cross section per nucleon assume a linear dependence of A for direct photon production.

Reaction	p_T(GeV/c)	γ/π^0(%)	$Ed\sigma/d^3p$(cm^2/GeV^2/Nucleon)
$pC\rightarrow\gamma+X$	2.25	<2.2	$<1.9\times10^{-32}$
	2.45	<2.0	$<7.6\times10^{-33}$
	2.55	1.1±2.1	$(2.6\pm5.2)\times10^{-33}$
	2.70	3.5±1.7	$(4.7\pm2.4)\times10^{-33}$
	2.90	4.4±1.8	$(2.8\pm1.1)\times10^{-33}$
	3.25	6.0±1.9	$(1.2\pm0.3)\times10^{-33}$
	3.75	6.0±3.1	$(1.7\pm0.9)\times10^{-34}$
	4.50	21.3±8.7	$(5.9\pm2.6)\times10^{-35}$
$\pi^+C\rightarrow\gamma+X$	2.20	<3.3	$<2.5\times10^{-32}$
	2.45	<2.4	$<6.4\times10^{-33}$
	2.80	1.3±2.4	$(1.3\pm2.4)\times10^{-33}$
	3.25	5.4±3.8	$(1.1\pm0.8)\times10^{-33}$
	3.75	20.±14.	$(4.3\pm2.9)\times10^{-34}$
	4.50	34.±30.	$(7.8\pm6.7)\times10^{-35}$
	5.50	42.±47.	$(3.3\pm3.7)\times10^{-35}$

TABLE 6.4

Background-Subtracted γ/π^0 Ratio (%) for Beryllium and Aluminum Targets

p_T(GeV/c)	pBe	pAl	π^+Be	π^+Al
2.20	0.4±1.6	<3.4	<10.4	<12.0
2.45	<2.6	<2.4	<6.6	<8.4
2.80	1.4±1.5	2.3±1.5	<6.6	3.2±4.7
3.25	2.7±3.6	4.0±3.2	<2.6	18.±11.
3.75	1.9±6.6	14.±8.		16.±15.

Figure 6.6

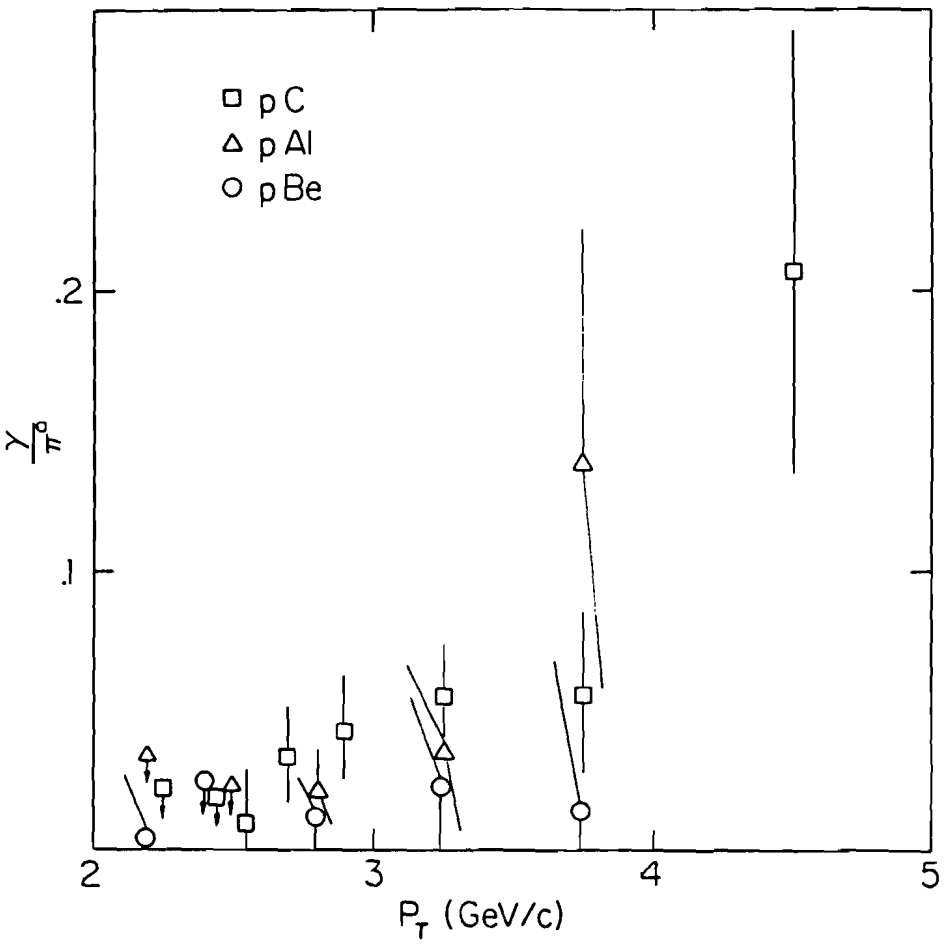

production [6.12]), and if π^0 production in the kinematic region covered by this experiment scales as $A^{1.1}$ (as discussed in the previous section), then the γ/π^0 ratio on nuclear targets should be smaller than that measured in pp collisions. The statistics of the E629 data are too poor to make any definitive statement about the A dependence, other than to say it is consistent with $A^{1.0}$.

The E629 results are in reasonable agreement with a previous measurement of the γ/π^0 ratio at Fermilab of $\gamma/\pi^0 = 8.0\pm2.5\%$ in 200 GeV/c pBe collisions, for $p_T>3$ GeV/c and center of mass rapidities in the range 0.0 to -1.7 (Ref. 1.41). At smaller values of transverse momentum ($p_T<2.5$ GeV/c) an upper limit for γ/π^0 of 2% was obtained in E629; this is significantly lower than the value measured in the previous experiment ($\gamma/\pi^0 = 6\pm2\%$). The difference might be attributable to the different rapidity ranges covered in the two experiments.

The E629 data are more consistent with results obtained at the CERN ISR. In the energy range $\sqrt{s}$ = 31-63 GeV ($y_{cm}\approx0$), measurements of direct photon production [6.13] and low mass virtual photons (e^+e^- pairs) (Ref. 1.38) indicate upper limits of a few percent for γ/π^0 in the p_T range 2-3 GeV/c, and a subsequent rapid rise of that ratio with increasing p_T. In the p_T range 3-5 GeV/c, the measurements of Anassontzis et al. (Ref. 1.45) at $\sqrt{s}$=31 GeV and the E629 value of $\gamma/\pi^0 = 7\pm2\%$ at $\sqrt{}$=19.4 GeV are consistent to within errors.

The E629 measurement of direct photon production is the only truly inclusive one to date. Other direct photon experiments have

applied isolation ("cleanliness" or "loneliness") cuts to the data before accepting events as direct photon candidates. This could lead to an underestimation of the direct photon cross section and of the γ/π^0 ratio; although similar cuts were applied to both γ and π^0 events, the effect of these cuts may be quite different for the two signals.

Using information on charged particles from the Axial Field Spectrometer drift chambers, Anassontzis et al. (Ref. 1.45) were able to estimate the effect of the isolation cuts and apply a correction for this bias to the data at $\sqrt{s}$=63 GeV [6.14]. These data and the E629 data at $\sqrt{s}$=19.4 GeV were used to investigate the scaling behavior of direct photon production with p_T and x_T. (A linear A dependence was assumed in order to obtain cross sections per nucleon from the E629 measurements. Discrepancies of ~10-20% in the relative normalization of the R806 and E629 data could result because of this assumption.) A fit to Eq. 6.4 (using data above p_T=2.6 GeV/c) yielded the results:

$$n=6.9\pm0.2,$$

$$m=7.9\pm0.8, \text{ and}$$

$$C=(7.3\pm2.7) \times 10^{-29} \text{ cm}^2/\text{GeV}^2/c^3.$$

The cross sections for the two experiments, multiplied by $p_T^{6.9}$, and the result of the fit (similarly scaled) are plotted versus x_T in Figure 6.7; the χ^2 per degree of freedom is 7/16. The systematic errors in the parameters are comparable to those obtained for the π^0

Figure 6.7

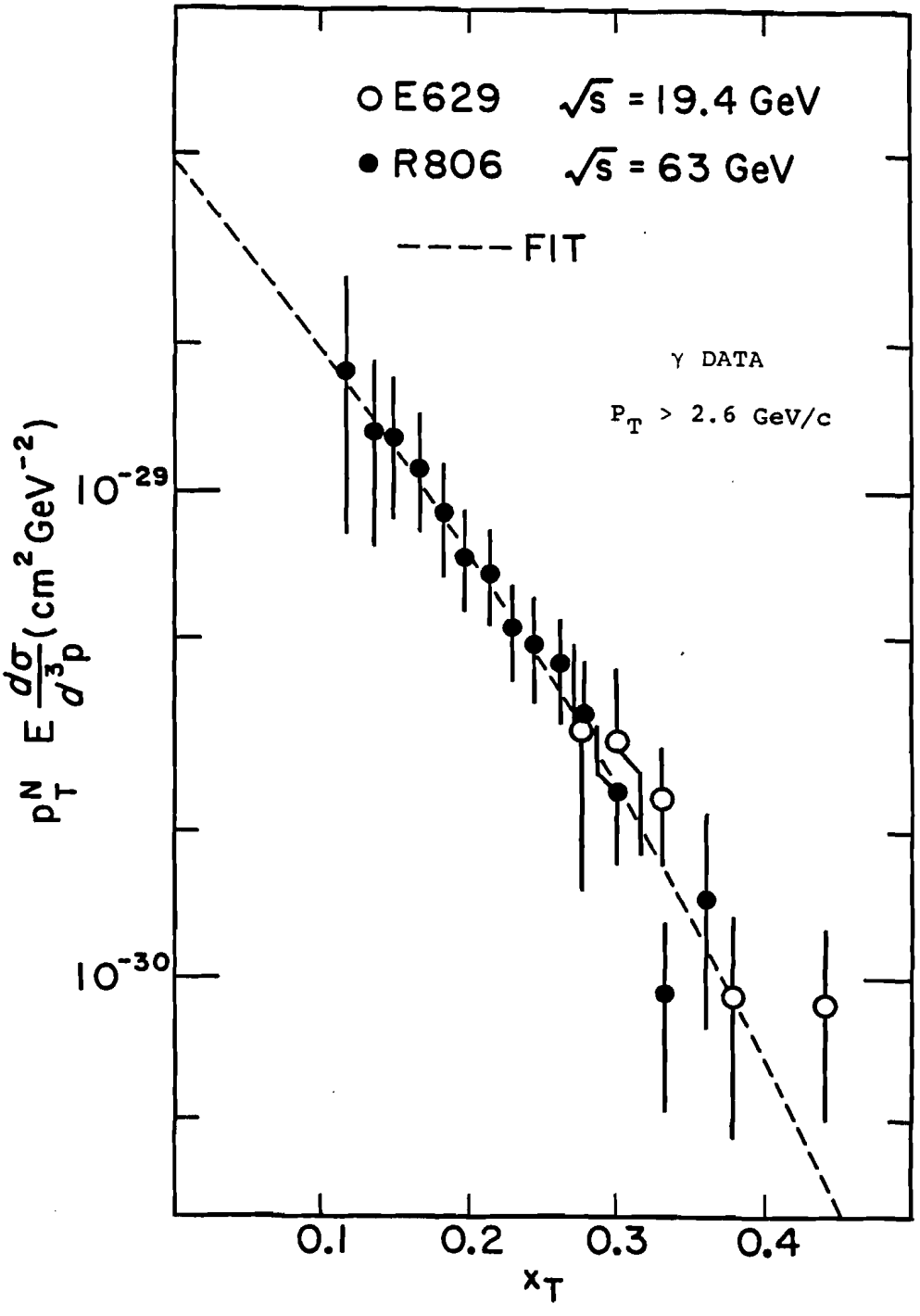
○ E629 $\sqrt{s}$ = 19.4 GeV
● R806 $\sqrt{s}$ = 63 GeV
---- FIT
γ DATA
P_T > 2.6 GeV/c
$p_T^N E \frac{d\sigma}{d^3p}$ (cm^{2}GeV^{-2})
10^{-29}
10^{-30}
0.1
0.2
0.3
0.4
x_T

fit described in section B. The uncertainty in the relative normalization of the two experiments (~30%) introduces a systematic error of ~0.3 in the value of n, and an error of ~1.1 in the value of m.

The naive parton model with pointlike coupling predicts a value of 8 for m and 4 for n [6.15]. As discussed in Chapter 1.B, Fermilab and ISR data indicate that cross sections for meson production at 90° in the center of mass and p_T<8 GeV/c roughly follow a p_T^{-8} dependence (i.e. Ref. 1.10). The scaling fit to the R806/E629 data (section B) exhibited similar behavior. The increase of the exponent n from 4 to ~8 is a consequence of the running of the strong coupling constant, scaling violations in the structure and fragmentation functions, and higher order contributions. The production of a π^0 involves the fragmentation of a constituent parton. One would expect the characteristics of the direct photon cross section to more closely resemble those observed in jet production if photons emerge as free particles in collisions among hadronic constituents; the similarity between the p_T dependence obtained in the fit to the γ data and that observed for jet production by experiment R807 at the ISR [6.16] suggests that this is the indeed the case.

D. Discussion of Results and Conclusions

The E629 measurements of the π^0 and η inclusive cross sections appear to be in agreement with previous measurements made under

similar conditions. The Monte Carlo prediction of the single photon background agrees with the data between p_T = 2.1-2.6 GeV/c, as expected if direct photons are not being produced in this region. The drop in the Monte Carlo prediction for this p_T interval is also seen in the data. Furthermore, predictions for the π^0 and η decay asymmetries (Fig. 4.11) match the observed distributions well. These facts indicate that the Monte Carlo accurately models the single photon background. Consequently, the observed systematic rise in the background-subtracted γ/π^0 ratio with increasing p_T is attributed to the production of single photons.

The hadronic production of direct photons may be calculated within the framework of quantum chromodynamics. The direct photon cross section measurements for pC and π^+C interactions (Table 6.3) are plotted in Figures 6.8a and 6.8b along with theoretical predictions for $\sqrt{s}$=19.4 GeV [6.17]. As discussed in Chapter 1, there are many uncertainties in the calculation of direct photon production. The effect of uncertainties in the proton's gluon distribution function is illustrated by the two sets of predictions in each figure; these estimates correspond to:

$$xG_{g/p}(x,Q_o^2=4\ \text{GeV}^2) \sim (1+9x)(1-x)^4, \text{ or alternately}$$
$$xG_{g/p}(x,Q_o^2=4\ \text{GeV}^2) \sim (1-x)^5, \text{ and}$$
$$xG_{g/\pi}(x,Q_o^2=4\ \text{GeV}^2) \sim (1-x)^3.$$

In the pN case, the choice of gluon distribution affects the absolute cross section by roughly a factor of two. In the π^+N case, the effect

Figure 6.8

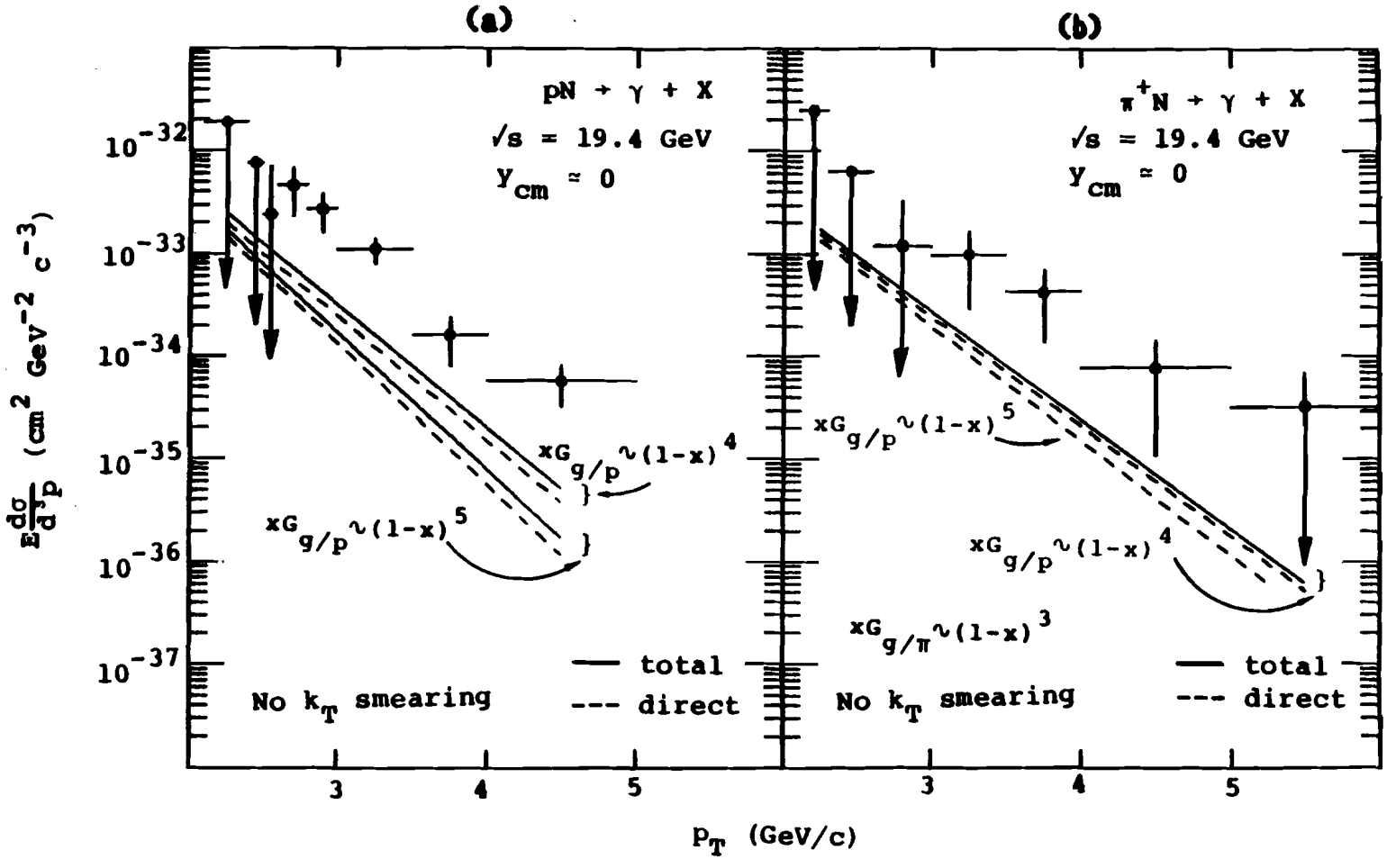
(a)
(b)
pN → γ + X
√s = 19.4 GeV
y_cm ≈ 0
π⁺N → γ + X
√s = 19.4 GeV
y_cm ≈ 0
E dσ/d³p (cm² GeV⁻² c³)
10⁻³²
10⁻³³
10⁻³⁴
10⁻³⁵
10⁻³⁶
10⁻³⁷
xG_g/p ∿ (1-x)⁴
xG_g/p ∿ (1-x)⁵
xG_g/p ∿ (1-x)⁵
xG_g/p ∿ (1-x)⁴
xG_g/π ∿ (1-x)³
total
direct
No k_T smearing
No k_T smearing
3
4
5
p_T (GeV/c)

is less because of the $q\bar{q}$ contribution, and because the π^+ gluon distribution was not varied. It is also possible that the momentum distribution of gluons in a nucleus is quite different from the distribution in an isolated proton [6.18]. The predictions labeled "total" were calculated by summing the contributions of the "direct" ($qg \rightarrow \gamma q$ and $q\bar{q} \rightarrow \gamma g$) and bremsstrahlung diagrams. The correction arising from the bremsstrahlung terms is not large in comparison to the variation associated with different choices for the gluon distribution.

Contogouris et al. calculated some of the "π^2" corrections to $qg \rightarrow \gamma q$ and $q\bar{q} \rightarrow \gamma g$ in the so-called soft-gluon limit [6.19]. These terms form part of the next-to-leading order corrections and may or may not comprise the bulk of the contribution from higher order terms. They yield multiplicative corrections in the range 1.4-1.8 for different Λ and Q^2 values.

The predictions shown in Fig. 6.8a and Fig. 6.8b do not include the effects of the k_T smearing of partons, which may lead to large enhancements in single particle cross sections. The magnitude of the enhancement depends on whether one uses "on-shell smearing", or if one puts partons with $k_T \neq 0$ off the mass shell, as would be required by kinematics. The on-shell approach raises the cross section by roughly a factor of three for $\langle k_T^2 \rangle = 1$ GeV^2. Off-shell smearing yields a smaller correction. However, $\langle k_T^2 \rangle = 1$ GeV^2 is probably unrealistically large. The large smearing phenomenologically incorporates contributions from higher order terms into the calculation.

Theoretical predictions [6.20] for γ/π^0 are a factor of two (or more) below the E629 results. It appears that theoretical difficulties remain in explaining the absolute yield of direct photons.

The γ/π^0 ratios are similar in both the proton and π^+ data. In this range of p_T, the u-quark Compton process is predicted to dominate direct photon production. Thus, only small differences in the ratio would have been expected.

In conclusion, the character of the increased production of π^0 and η mesons in the interaction of π^+ and protons on nuclear targets is similar to meson production on hydrogen. This suggests a common primary and secondary scattering mechanism for $\pi^{\pm}$, π^0, and η production. Direct photon production in pC and π^+C collisions has been observed for $p_T>2.5$ GeV/c. The ratio γ/π^0 is <2% for $p_T<2.5$ GeV/c. It rises with increasing p_T, attaining an average value of 7±2% above 3 GeV/c in pC interactions, and an average value of 7±4% for π^+C reactions in the same p_T range. No strong energy-dependence for γ/π^0 is observed at fixed p_T between $\sqrt{s}$=19.4 GeV and $\sqrt{s}$=63 GeV.

In Chapter 1, the phenomenological uncertainties inherent in QCD predictions were discussed. Because of these ambiguities, and because there is at present no complete calculation of the higher-order contributions to direct photon production, it is not altogether surprising that predictions for prompt photon absolute cross sections disagree with the data (i.e. Fig. 6.8). Although the statistical errors are too large to permit a definitive statement to

be made, the choice of a "hard" $(1+9x)(1-x)^4$ proton gluon distribution and the introduction of k_T smearing seem to improve the agreement between the calculated and measured direct γ cross sections.

REFERENCES AND FOOTNOTES

[1.1] Several review articles on QCD and its associated phenomenology may be found in Perturbative Quantum Chromodynamics, Physics Reports Reprint Book Series -- Vol. 5, ed. M. Jacob, North Holland (1982).

[1.2] R. P. Feynman, Photon-Hadron Interactions, (W. A. Benjamin Inc., Reading, Mass., 1972); J. Bjorken, lectures given at the International Summer Institute in Theoretical Physics, DESY, Sept. 1975.

[1.3] The definition of Q^2 is not unique in hadron-hadron collisions. This ambiguity is discussed later in this section.

[1.4] C. Quigg, Gauge Theories of the Strong, Weak, and Electromagnetic Interactions, Benjamin-Cummings Pub. (1983); I. J. R. Aitchison and A. J. G. Hey, Gauge Theories in Particle Physics, Adam Hilger Ltd. (1982). This expression results from summing the lowest order corrections to the gluon propagator (the "one-loop" corrections).

[1.5] The parameter Λ and α_s at some fixed value Q_o^2 are not specified and must be experimentally determined. QCD then describes the evolution of α_s with Q^2. The latest favored value for Λ is ~200 MeV/c. See B. Adeva et al., Phys. Rev. Lett. 50, 2051 (1983).

[1.6] D. Gross and F. Wilcek, Phys. Rev. Lett. 30, 1323 (1973), and Phys. Rev. D8, 3633 (1973); H. D. Politzer, Phys. Rev. Lett. 30, 1346 (1973).

[1.7] For example, see Ref. 1.1. Eq. 1.2 applies to partons moving collinearly. Effects due to the transverse Fermi motion of partons confined within hadrons are not included. The influence of "intrinsic k_T" is discussed later in this section.

[1.8] The number distribution functions G are related to the structure functions F by: $F(x,Q^2) = xG(x,Q^2)$.

[1.9] G. R. Farrar, Phys. Lett. 67B, 337 (1977); S. M. Berman, J. D. Bjorken, and J. Kogut, Phys. Rev. D4, 3388 (1971).

[1.10] For example, see the review article: S. D. Ellis and R. Stroynowski, Rev. Mod. Phys. 49, 753 (1977).

[1.11] H. Georgi and H. D. Politzer, Phys. Rev. D9, 416 (1974); D. J. Gross and F. Wilczek, Phys. Rev. D9, 980 (1974); A. DeRujula, H. Georgi, and H. D. Politzer, Ann. Phys. 103, 315 (1977); G. Altarelli and G. Parisi, Nucl. Phys. B126, 298 (1977).

[1.12] K. Wilson, Phys. Rev. 179, 1499 (1969). See also Ref. 1.1.

[1.13] R. Ellis, M. Furman, H. Haber, and I. Hinchliffe, Nucl. Phys. B173, 397 (1980).

[1.14] A. Buras, Lepton-Photon Conference, Bonn, Germany, Aug. 24-29, 1981.

[1.15] R. D. Field, Lectures given at the Boulder Summer School on Quantum Flavordynamics, Quantum Chromodynamics, and Unified Theories, University of Colorado, July 9-27, 1979.

[1.16] R. Blankenbechler, S. Brodsky, and J. Gunion, Phys. Rev. D18, 900 (1978).

[1.17] D. H. Perkins, Techniques and Concepts of High-Energy Physics, ed. T. Ferbel, Plenum Press (1981).

[1.18] H. Wahlen, presented at the 18th Rencontre de Moriond, La Plagne, France, Jan. 23-29, 1983; D. W. Duke and J. F. Owens, Phys. Rev. D23, 1671 (1981).

[1.19] The physics of direct photons is reviewed by T. Ferbel and W. Molzon, Rev. Mod. Phys. 56, 181 (1984).

[1.20] P. Aurenche and J. Lindfors, Nucl. Phys. B168, 296 (1980); M. Nowak and M. Praszalowicz, Zeit. Phys. C17, 249 (1983).

[1.21] A. Buras and K. Gaemers, Nucl. Phys. B132, 249 (1978); R. P. Feynman, R. D. Field, and G. Fox, Phys. Rev. D18, 3320 (1978); J. F. Owens and E. Reya, Phys. Rev. D17, 3003 (1978).

[1.22] Distributions for the proton are from Feynman, Field, and Fox (previous ref.). For the pion distributions, see R. D. Field, Phys. Rev. D27, 546 (1983).

[1.23] L. Cormell and J. Owens, Phys. Rev. D22, 1609 (1980); F. Halzen, M. Dechantsreiter, and D. M. Scott, Phys. Rev. D22, 1617 (1980).

[1.24] C. Bromberg et al., Phys. Rev. Lett. 38, 1447 (1977); Nucl. Phys. B134, 189 (1978).

[1.25] A. P. Contogouris, S. Papadopoulos, and J. Ralston, Phys. Rev. D25, 1280 (1982); O. Benary, E. Gotsman, and D. Lissauer, Zeit. Phys. C9, 81 (1981) and Zeit. Phys. C16, 211 (1983); K. Kato and H. Yamamoto, Prog. of Theor. Phys.

64, 230 (1980); R. R. Horgan and P. N. Scharbach, Nucl. Phys. B181, 421 (1981).

[1.26] The curves in Fig. 1.5 are the calculations of: a) R. Ruckl, S. Brodsky, and J. Gunion, Phys. Rev. D18, 2469 (1978); b) F. Halzen and D. M. Scott, Phys. Rev. D18, 3378 (1978); c) F. Halzen and D. M. Scott, Phys. Rev. D21, 1320 (1980); and d) A. P. Contogouris, S. Papadopoulos, and M. Hongoh, Phys. Rev. D19, 2607 (1979).

[1.27] K. Heller et al., Phys. Rev. D16, 2737 (1977).

[1.28] R. J. Glauber, Lectures in Theoretical Physics, Vol. 1, ed. W. E. Brittin and L. E. Dunham (1958) (Inter-Science, NY, 1959).

[1.29] W. Busza et al., Phys. Rev. Lett. 34, 836 (1975).

[1.30] J. R. Florian et al., Phys. Rev. D13, 558 (1976).

[1.31] J. Cronin et al., Phys. Rev. D11, 3105 (1975).

[1.32] K. Gottfried, Phys. Rev. Lett. 32, 957 (1974); G. Farrar, Phys. Lett. 56B, 185 (1975); J. Pumplin and E. Yen, Phys. Rev. D11, 1812 (1975); J. Kuhn, Phys. Rev. D13, 2948 (1976); A. Krzywicki, J. Engels, B. Petersson, and U. Sukhatme, Phys. Lett. 85B, 407 (1979); A. Capella and J. Tran Thanh Van, Phys. Lett. 93B, 146 (1980).

[1.33] D. Antreasyan et al., Phys. Rev. D19, 764 (1979).

[1.34] H. Frisch et al., Phys. Rev. D27, 1001 (1983).

[1.35] S. Drell and T. Yan, Phys. Rev. Lett. 25, 316 (1970).

[1.36] M. Binkley et al., Phys. Rev. Lett. 37, 571 (1976); D. Antreasyan et al., Phys. Rev. Lett. 39, 906 (1977); D. M. Kaplan et al., Phys. Rev. Lett. 40, 435 (1978); K. J. Anderson et al., Phys. Rev. Lett. 42, 944 (1979).

[1.37] W. Willis, talk at the 4th International Colloquium on Photon-Photon Interactions, Paris, 1981, CERN preprint CERN-EP/82-26.

[1.38] J. Cobb et al., Phys. Lett. 78B, 519 (1978).

[1.39] A. Chilingarov et al., Nucl. Phys. B151, 29 (1979).

[1.40] P. Darriulat et al., Nucl. Phys. B110, 365 (1976).

[1.41] R. Baltrusaitis et al., Phys. Lett. 88B, 372 (1979).

[1.42] E. Amaldi et al., Phys. Lett. 84B, 360 (1979).

[1.43] A. Angelis et al., Phys. Lett. 94B, 106 (1980).

[1.44] A. Angelis et al., Phys. Lett. 98B, 115 (1981).

[1.45] E. Anassontzis et al., Zeit. Phys. C13, 277 (1982); M. Diakonou et al., Phys. Lett. 87B, 292 (1979); M. Diakonou et al., Phys. Lett. 91B, 296 (1980).

[1.46] T. Akesson et al., Phys. Lett. 118B, 178 (1982).

[1.47] T. Akesson et al., Phys. Lett. 123B, 367 (1983).

[2.1] Further information on the M-1 beamline is provided in the M-1 User's Guide, S. Ecklund, Fermilab Report TM-743.2833, May 1977.

[2.2] TRANSPORT User's Manual, K. L. Brown et al., Fermilab Report NAL-91, March 1974.

[2.3] The counter was designed by T. F. Kycia. For a description of its operation, see the Appendix of Ref. 2.1.

[2.4] Details on the construction of the hodoscope may be found in C. Bromberg, S. R. W. Cooper, and R. A. Lewis, Nucl. Inst. and Meth., 200, 245 (1982).

[2.5] " Review of Particle Properties", Particle Data Group, Phys. Lett. 111B, April 1982.

[2.6] Radiation lengths scale roughly as A/Z^2, while interaction lengths tend to increase as $A^{1/4}$ (for example, see Ref. 2.7). The A versus Z curve for stable elements has the form $A/Z \approx 2 + 0.015A^{2/3}$ (i.e. see the discussion in E. Feenberg, Rev. Mod. Phys. 19, 239 (1947)). Thus, the ratio of radiation to interaction length is more favorable for low Z targets.

[2.7] The phenomenology of electromagnetic and hadronic showers and the principles of calorimetry are discussed in a TRISTAN workshop review by S. Iwata, "Calorimeters (Total Absorption Detectors) for High-Energy Experiments at Accelerators", Nagoya University Report DPNU-3-79, (February, 1979).

[2.8] W. J. Willis and V. Radeka, Nucl. Inst. and Meth. 120 , 221 (1974).

[2.9] For a more detailed description of the E272/E629 LAC, see C. Nelson et al., Nucl. Inst. and Meth. 216, 381 (1983).

[2.10] J. Engler et al., Nucl. Inst. and Meth. 120 , 157 (1974); W. Hofmann et al., Nucl. Inst. and Meth. 135 , 151 (1976).

[2.11] G. Knies and D. Neuffer, Nucl. Inst. and Meth. 120 , 1 (1974).

[2.12] C. Brassard, Nucl. Inst. and Meth. 162 , 29 (1979).

[2.13] S. E. Derenzo et al., Phys. Rev. A9, 2582 (1974).

[2.14] T. F. Droege, F. Lobkowicz, and Y. Fukushima, Fermilab Report TM-746 2500.000 (Oct. 1977).

[2.15] Because the global and local p_T triggers were sensitive only to energy deposited in the front-X strips, the actual transverse momentum of an event (or individual particle) was greater than that sensed by the trigger. Here, and throughout the text, quoted p_T threshold values should be interpreted as conditions on the front-X component of the "true" p_T which must be met in order to satisfy the trigger. The nominal 2.2 GeV/c global threshold is roughly equivalent to a total p_T of ~2.4-2.5 GeV/c for an event, and the 600 MeV/c local p_T threshold corresponds roughly to a p_T of ~800 MeV/c deposited in a three strip region of the LAC.

[2.16] The summed analog global p_T signal was cabled to a discriminator module which produced an output signal when the input signal exceeded a fixed voltage threshold. The "trigger threshold" for a particular region of the detector was the p_T value at there was the p_T value for which there was a 50% probability for an event to trigger the experiment (noise in the input signal is the motivation for defining this threshold in terms of probability). The trigger threshold depended not

only on the discriminator threshold, but also on the attenuation applied to individual strips in forming the analog sum. By varying these weighting factors, it was possible to effectively set the p_T trigger threshold at different levels in different regions of the LAC.

[2.17] The time interval for veto protection was asymmetric about the trigger time because of constraints imposed by the fixed values of the delay elements in the LAC amplifiers (Fig. 2.10a) and the transit times for signals from counters used in defining this veto. Protection could only be extended to ~50 nsec past the trigger time. See also Chapter 4.C.

[2.18] The on-line software was based on the MULTI package, tailored for use in this experiment. MULTI is supported by the Fermilab Computing Department. Further details may be found in the Fermilab MULTI User's Guide (PN-97.5).

[3.1] Mean pedestal values for individual runs drifted by ~2.7 ADC counts over the course of the experiment.

[3.2] The uncertainty in the gain measurement did not greatly affect the energy resolution of the LAC. Fluctuations in energy deposition and discrete sampling of the shower were more significant factors.

[3.3] In a later stage of the analysis, a linear variation of the π^0 mass with X-position in the LAC was discovered (Chapter 4.E). An additional correction to the photon energies compensated for this effect.

[3.4] The amplifiers for strips 85-88 were situated on a spare module used as a replacement for one that failed prior to the run. The gains for these four channels were somewhat lower than those of other strips because the input capacitors for these amplifiers had different values. This did not affect the determination of strip energies. Variations in gain contributed to the smearing of the global p_T threshold (Chapter 5.B). This smearing was incorporated into the Monte Carlo for the trigger acceptance.

[3.5] For example, see Ref. 2.7.

[3.6] G. A. Akopdjanov et al., Nucl. Inst. and Meth. 140, 441 (1977).

[3.7] J. Huston, Ph. D. Thesis, Univ. of Rochester (1983).

[3.8] J. Cobb et al., Nucl. Inst. and Meth. 158, 93 (1979).

[3.9] S. Cihangir, Ph. D. Thesis, Univ. of Rochester (1981).

[4.1] The "hadrons" referred to in this context include (for example) charged pions, but not particles which decay electromagnetically, such as the π^0 or η.

[4.2] The 0.2% bias associated with the hadron, angle, and timing cuts scales the photon cross section by a multiplicative factor. The absolute error introduced in the γ/π^0 ratio (~20% at 2 GeV/c) is roughly 0.04%. This is considerably smaller than the ±2% systematic error on γ/π^0 attributed to other sources (Chapter 6.A).

[4.3] The proportional wire chamber data were not used to identify hadrons. In the off-line analysis, the chambers were found to be too inefficient and noisy to permit reliable track reconstruction.

[4.4] See the discussions in Chapter 2.C and Chapter 5.F regarding conversion electrons; essentially the same arguments apply to Dalitz pairs.

[4.5] Absorption lengths were calculated using the absorption cross section measurements of S. P. Denisov et al., Nucl. Phys. B61, 62 (1973). Data were obtained for π^+ and p incident on various nuclear targets (including beryllium, carbon, and aluminum) over the energy range 20-60 GeV.

[4.6] The systematic error in the determination of the proton and pion beam flux is discussed in Chapter 6.A.

[4.7] Ref. 3.7, Chapter V.A. See also J. Huston, "Muon Contamination in E272", University of Rochester Internal Report.

[5.1] For the trigger model, p_T^{xf} was required. The X-component of the total p_T was calculated using the X and Y coordinates. Energy was partitioned between the front and back portions of the calorimeter according to the probability distribution for an electron's back/total energy ratio (Fig. 4.1b). The calculated acceptance was averaged over this back/total energy split.

[5.2] Strictly speaking, the X-Y coordinates used to calculate τ and σ should have been determined by taking a weighted average over all the strip energies in the detector. However, because most of the p_T in an event was carried by a single particle, it was assumed that the "associated" p_T did not appreciably perturb the energy-weighted mean position away from the X-Y coordinates of the π^0 (η).

[5.3] As discussed in Chapter 2.F, signals from the LAC strips were weighted and summed. If the summed voltage exceeded a fixed discriminator threshold, the global p_T trigger requirement was met. The values chosen for the weighting factors resulted in an effective variation of the trigger threshold across the detector.

[5.4] In the range p_T = 2.1-2.3 GeV/c, $-0.75 < y_{cm} < -0.3$ for the π^0, and $-0.5 < y_{cm} < -0.3$ for the η; $\langle y_{cm}\rangle_{\pi^0} = -0.52$ and $\langle y_{cm}\rangle_{\eta} = -0.4$. Between p_T = 2.3 and 2.6 GeV/c, $-0.3 < y_{cm} < 0.0$ for both particles; $\langle y_{cm}\rangle_{\pi^0} = \langle y_{cm}\rangle_{\eta} = -0.15$. Above p_T = 2.6 GeV/c, $0.0 < y_{cm} < 0.2$ for the π^0 ($\langle y_{cm}\rangle_{\pi^0} = 0.1$), and $0.0 < y_{cm} < 0.1$ for the η ($\langle y_{cm}\rangle_{\eta} = 0.05$).

[5.5] Processes such as $\eta \to 3\pi^0$ contribute to the single photon background at roughly the same level as the ω and η', but are included as part of the inclusive π^0 cross section.

[5.6] For a more general derivation, see N. S. Craigie, Phys. Rept. 47, 1 (1978).

[5.7] The η/π^0 ratio was measured in this experiment (Chapter 6.B). The production ratio for the η' measured in E629 was averaged with the data of Ref. 6.10 and Ref. 6.11. Production ratios for the ρ, K^*, and ϕ are tabulated in R. Feynman and R. Field, Nucl. Phys. B136, 1, (1978); the authors reference the ρ and ϕ measurements. The Δ^+, Σ^0, and $\bar{\Sigma}^0$ production ratios were estimated by multiplying the measured p/π ratio by theoretical predictions for Δ/p and Σ/p from V. V. Anisovich and V. M. Shekhter, Nucl. Phys. B55, 455 (1973). The values quoted for these theoretically derived factors reflect the relative magnitudes of directly produced particles only; the effects of decaying baryon/meson resonances on the production ratios are assumed to be small at large p_T. Branching ratios are from Ref. 2.5.

[5.8] Because of the LAC energy resolution, there is a small probability for $F_h(p_T', p_T)$ to be nonzero for $p_T' < p_T$. This was neglected in the background calculation.

[5.9] These factors were derived from the 200 GeV pBe data of Ref. 1.33 at $p_T = 3.08$ GeV/c. The K^+, K^-, p, and $\bar{p}$ cross sections were divided by the average of the π^+ and π^- cross sections measured using the same apparatus to obtain the production ratios. The E629 π^0 inclusive cross section (Chapter 6.B) agrees with the averaged π^+ and π^- data to within the systematic errors of the two experiments.

[5.10] There may also be contributions from processes in which (for example) a resonance produced at large x_F decays into two or more low x_F π^0's. The estimates for the weighting factors did not take these processes into consideration; it was assumed that either the cross section for producing such a resonance at large x_F would be small, or that the branching ratio for decay into a final state consisting exclusively of π^0's would tend to suppress the contribution of these particles. Other mechanisms which lead to the production of multiple low x_F π^0's (including particles in the forward and backward center of mass hemispheres) were neglected because a significant fraction of the energy in these reactions should generally be shared with other hadrons (i.e. charged particles or neutral hadrons that do not produce electromagnetic showers -- see Ref. 2.7).

[5.11] V. V. Anisovich et al., Nucl. Phys. B55, 474 (1973) give predictions for π^0 production at large x_F in πp, Kp, and pp collisions. These predictions were based on data for charged pion production at energies of 10-20 GeV. Data for 100 GeV/c πp, Kp, pp, and $\bar{p}p$ interactions are tabulated in BNL- 23844 (BNL-CIT-LBL).

[5.12] A charged pion may interact with a nucleus via charge exchange and produce a π^0 which carries off nearly all of the available energy. The probability of obtaining a leading π^0 in a process involving an incident proton or kaon is much smaller (i.e. because quantum numbers must be conserved). The response of a

liquid argon/iron calorimeter to 10 GeV/c protons and pions is discussed by C. W. Fabjan et al., Nucl. Inst. and Meth. 141, 61 (1977). The distribution of charge deposited in the detector differed for the two beams. The distribution observed when π^- were incident had a "break" attributed to charge exchange. This feature was much less prominent in proton interactions. The relative magnitudes of the large x_F π° cross sections for pp and Kp collisions may be explained in part by differences in the proton and kaon valence quark momentum distributions; a quark in a kaon would be expected to have a larger average fraction of the incident momentum. Thus, the production of a forward π° in a Kp collision should be favored with respect to production in a pp interaction. See G. Donaldson et al., Phys. Rev. Lett. 40, 917 (1978).

[5.13] The application of a cut on shower width is a technique which improves the hadron rejection capabilities of a photon detector (i.e. Ref. 2.7). This was attempted at an early stage in the analysis, but abandoned without success. The reason for the failure was understood after studies of the reconstruction program were performed. The algorithm used to calculate the width of the peak tended to truncate shower tails upon encountering these strip energy fluctuations, interpreting the residual energy as a second "photon".

[5.14] For example, see Equation 3.3.

[5.15] The algorithm was derived by R. L. Walker. It is described in R. A. Johnson, Ph. D. thesis (1975), LBL-4610.

[5.16] B. Rossi, K. Greisen, Rev. Mod. Phys. 13, 240, (1941).

[5.17] The one GeV minimum energy cut on the data fixes the lower limit.

[5.18] It was even less likely for an electron pair produced downstream of the target to be misconstrued as two individual photons because the spacing, Δs, between shower centroids was proportionally smaller for conversions that occurred nearer to the LAC.

[6.1] Some of these results have appeared in previous publications of the E629 collaboration: J. Povlis et al., Phys. Rev. Lett. 51, 967 (1983); M. McLaughlin et al., Phys. Rev. Lett. 51, 971 (1983).

[6.2] See Chapter 2.A, Fig. 2.2 for the definition of the coordinate system; see also Chapter 2.F.

[6.3] This effect was studied by J. Huston (private communication).

[6.4] The beam is predominantly composed of protons (~85%). A 15% error in the measurement of the π^+ fraction (~15% of the beam) leads to an error of (.15)(.15)~2% in the proton flux determination.

[6.5] The nonlinearity of the energy response contributes to the overall energy scale uncertainty (determined from the π^0 and η masses) discussed at the beginning of this section. It accounts for, at most, 30% of this effect.

[6.6] D.C. Carey et al., Phys. Rev. Lett. 33, 327 (1974) and Phys. Rev. D14, 1196 (1976); J.A. Appel et al., Phys. Rev. Lett. 33, 719 (1974); G. Donaldson et al., Phys. Rev. Lett. 36, 1110 (1976); R.M. Baltrusaitis et al., Phys. Rev. Lett. 44, 122 (1980).

[6.7] G. Donaldson et al., Phys. Rev. Lett. 40, 684 (1978).

[6.8] This effect was also observed by M. D. Corcoran et al., Phys. Rev. Lett. 41, 9 (1978).

[6.9] C. Kourkemelis et al., Zeit. Phys. C5, 95 (1980).

[6.10] G. Donaldson et al., Phys. Rev. D21, 828 (1980).

[6.11] M. Diakonou et al., Phys. Lett. 89B, 432 (1980).

[6.12] See the discussion in Chapter 1.D.

[6.13] E. Amaldi et al., Nucl. Phys. B150, 326 (1979); A. Angelis et al., Ref. 1.43 and Ref.1.44; M. Diakonou et al., Ref. 1.45.

[6.14] These data are essentially the results of experiment R806 (M. Diakonou et al., Ref. 1.45) corrected by a factor of ~1.4 to obtain inclusive yields. See also: V. Burkert, Proceedings of the Recontre de Moriond (1983), J. Tran Thanh Van, ed., for an approximate determination of the scaling properties of direct photon production using R806 data alone; J. Huston, Proceedings of the 14th International Symposium on Multiparticle Dynamics (Lake Tahoe, 1983), J. Gunion, ed. (to be published).

[6.15] For example, see R. Ruckl, S.J. Brodsky, and J.F. Gunion, Ref. 1.26.

[6.16] W.R. Molzon, Proceedings of the Recontre de Moriond (1983), J. Tran Thanh Van, ed.

[6.17] These are unpublished calculations provided by J. Owens, Florida State University (1983) in a private communication to C. Bromberg (E629).

[6.18] J.J. Aubert et al., Phys. Lett. 123B, 275 (1983); A. Bodek et al., UR 858 COO-3065-365 (Invited Talk given at the 6th High Energy Heavy Ion Study, Berkeley, CA, June 28 - July 1, 1983).

[6.19] See Chapter 1.E, Fig. 1.6 and Ref. 1.25.

[6.20] S. Petrarca and F. Rapuno, Phys. Lett. 88B, 167 (1979); F. Halzen, M. Dechantsreiter, and D. M. Scott, University of Wisconsin Report No. MAD/PH121, 1981 (to be published), and Ref. 1.23; A. Contogouris, A. Papadopoulos, and J. Ralston, Phys. Lett. 104B, 70 (1981), and Ref. 1.25; R. Baier, J. Engels, and B. Petersson, Zeit. Phys. C6, 309 (1980); L. Cormell and J. F. Owens, Ref. 1.23; R. Ruckl, S. J. Brodsky, and J. F. Gunion, Ref. 1.26.